Combined magnetic, electric, ferroelectric and magnetoelectric characterization of novel multiferroic perovskites obtained by high pressure/temperature synthesis

Davide Delmonte

Ph.D Thesis in Physics

Parma, January 2015

Università degli studi di Parma
Physics and Earth Science Department

Coordinator: Chiar.mo Prof. Cristiano Viappiani

Supervisor: Chiar.mo Prof. Massimo Solzi

External Supervisor: Dr. Edmondo Gilioli

Author's address:

Davide Delmonte

davide.delmonte@fis.unipr.it

davide.delmonte@imem.cnr.it

Physics and Earth Science Department

Università degli Studi di Parma

Parco Area delle Scienze 7/A
I-43124 Parma
Italy

Institute of Materials for Electronics and Magnetism (IMEM)

Research National Council (CNR)

Parco Area delle Scienze 37/A
I-43124 Parma
Italy

A mio Padre e mia Madre

Table of Contents

Colonel:
"Surely, you will not turn down the opportunity of commanding a brigade?
The Emperor is our hope and strength.
We belong to him!"

General D'Hubert:
"Colonel, I have entertained the notion that I may belong to myself.

From "The Duellists", a film by Ridley Scott (1977) based on a novel of J. Conrad

The reasons of a choice

In the long way of human progress, the role of Science followed the social and economical changes, often along contradictory paths. Since its dawn, the political establishment managed Science as an instrument of power. Thereby Science (and so scientists) was born deprived by its basic commandment: the freedom of seeking answers to independent questions. What exactly happened was that the questions to be answered were directly established by the Power so that the scientists were coerced to blindly accept an ill-concealed subordination in the name of the possibility to practice their '*art*', consequently renouncing to the cultural role they would have been entitled to. Such strong social authority limitation is dramatic as far as the natural aspiration of representing a free-standing entity is concerned. How might Science be effectively useful for the entire population, confined within these boundaries? Aristotle, one of the fathers of the Western Science, foresaw this problem with words of incomparable wisdom[†]: *"At first he who invented any art that went beyond the common perceptions of man was naturally admired by men, not only because there was something useful in the inventions, but because he was thought wise and superior*

[†]Aristotle: Metaphysics, Books I-IX, Loeb Classical Library No. 271 (1933)

[†] The set-up for measuring electrical resistivity in the SQuID has been completely developed before my arrival

to the rest. But as more arts were invented, and some were directed to the necessities of life, others to its recreation, the inventors of the latter were always regarded as wiser than the inventors of the former, because their branches of knowledge did not aim at utility."

In the XXI century the panorama is utterly worsened. The funds offloaded in the scientific research derive almost entirely from private sources, often multinational corporations, and the public/social investments are negligible or even missing. This is a natural outcome of the final power transfer from the national governments to the world of finance, the latest terrifying event of uncontrolled capitalistic era. Nevertheless a little number of isolated realities have survived sustained by public investment; herein Science still preserves a tiny independence. That is why I chose to become a researcher, for the survival of such realities and moved by the hope to give an effective contribution as a public employed. In my Ph.D activity at University of Parma, I have worked in order to enforce my knowledge and to develop the capability of planning and realizing scientific "products" of "*social utility*", quoting the words of Aristotle.

I consider myself fortunate, because no one, neither my supervisors nor my graduated colleagues, imposed me strategies or courses of action, so I was free to organize my daily work and chase my ideas. This is not a usual condition and, for this reason, I attach importance to open this Thesis thanking them all for putting unconditioned trust in me, as researcher but mainly as man. I will look forward to become the scientist that I have pictured in this prelude: namely devoted to the society, to my country and not to this or that private interest.

I. Introduction

The mass technological revolution, exploded around the later Seventies, has invaded the global market and completely changed the way of making scientific research. Every day we are witnessing the exponential increasing of new performing devices which permeate our daily life. Simultaneously, behind the scenes, further requests of new developments continue to feed this unstoppable machine. The addressee of such requests is, of course Science, which is obliged to keep in step with this. In particular, the efforts of Materials Science, Physics and Engineering (listed in this order as primary-secondary and tertiary stages of development) are nowadays prevalently devoted to seek innovative solutions in the new generation devices' scalability within different technological macro-areas (i.e. electronics, energy, transports etc.). In particular, the current main issue is the need of multi-functionality or rather the possibility of joining different and independent "functions" in the same physical component. To this wide category belong electro-optic materials, that currently lead the field of data transfer and manipulation; ferromagnetic semiconductors, providing high efficiency in LED structures and offering interesting perspectives in spintronics development; magnetoresistive compounds, bound to become dominant in the market of random access memories in virtue of low power consumption and high operating frequencies; multiferroic materials, finally, which deserve attention aside, as principal actors of my studies. Specifically referring to the data storage technology, multiferroics application may theoretically allow doubling both the density of storable information and the velocity of writing/reading processes, if compared to the devices currently commercialized. These are fundamental characteristics as far as the current rush towards high-speed electronic devices' miniaturization is considered. Furthermore, multiferroics can be achieved as key element in the production of electric and magnetic field multi-sensors and can be utilized as constitutive parts of electronic trasducers.

All these potentialities are however obstructed by the lacking availability of natural multiferroics compounds. Here comes the scientific Research. Indeed the role of Material Scientist is mandatory, to product novel materials individuating the more effective synthesis

strategies. Later, once a new multiferroic is synthesized, its functionalities have to be correctly quantified. This is another inevitable step that requires a Physical approach for building-up specific characterization techniques and thus for interpreting the experimental data. In conclusion, the multiferroic-based device must be designed and realized in agreement with the displayed properties. This is a further critical point that usually needs Engineering competence to be carried out.

The present Thesis concerns the first two stages of this chain. Herein I present the basic scientific developments and technical improvements carried out to prepare, together with my colleagues, a specific laboratory for the production and study of multiferroic materials. In the discussion, some of the most significant samples are reported in order to help the reader to understand what we are effectively able to do and how we operate. Some results start to pay us back of the intense work despite some failures met along the way. As it often happens, the solution is hidden behind the comprehension of our mistakes and it appears just when the difficulties are faced.

II. On Multiferroic Magnetoelectrics and their characterization

A. The Magnetoelectric Effect and the born of the term Multiferroism

The four equations governing the classical electrodynamics, proposed by James Clark Maxwell in 1865 [1], represented the final unification of the electric field and magnetic field in an unique entity: the "electromagnetic field". This theory shows that magnetic interactions and motion of electric charges, which were initially thought to be two independent phenomena, are otherwise intrinsically coupled to each other. This correlation justifies in principle the existence of components of the susceptibility which couples the electric (magnetic) field with the magnetic (electric) polarization response.

Truthfully the first observations of this coupling are dated back to Faraday, whom, ten years before, found a slight magnetic dependence on the electrical field without understanding the reason. After the Maxwell's turning point, experimental scientists tried to directly measure the mutual effect in the matter. First among everyone in 1888, the German physicist Röntgen [2] (whom contributes on the later X-ray discovery) observed that a couple of dielectric oxides, put in oscillation into an external electric field, tended to magnetize. Only seventeen years later, the opposite phenomenon, namely the polarization of a dielectric material during its oscillation in a static magnetic field, was also recorded. However the first theoretical prediction about the possible mechanism at the basis of magnetoelectric effect is due to Pierre Curie; in 1894 with a famous work named *"Sur la symétrie dans les Phénomènes Physiques"* [3], starting from considerations about the symmetry of the crystalline systems. He stated the possibility to observe intrinsic magnetic and electric character in the matter even in absence of any applied magnetic or electric field. The terms "magnetoelectric" was coined more than thirty years later by Paul Debye [4], by discussing the affirmation for which a dielectric system is able to develop magnetic polarization only through a time inversion symmetry breaking. Nevertheless, the complete description of the link between symmetry and magnetoelectricity was carried out by Landau in 1937 (and then formally in 1962 together with Lifschitz) in a comprehensive dissertation based on the

Group Theory [5,6]. As a consequence, it became clear that the time inversion symmetry breaking could be obtained at least in two cases: by the application of an external magnetic field, or by the occurrence of a spontaneous long range magnetic order.

It is just in the middle of the Cold War that two Russian physicists, Dzyaloshinskii [7] and Astrov [8] succeeded to unveil the symmetry breaking in the antiferromagnetic system Cr_2O_3. Indeed, by means of an innovative instrument, Astrov was able to measure the magnetization generated by an electric field and vice versa, the polarization induced by an external magnetic field; thus allowed to properly calculate the magnetoelectric coefficient of the compound. Pushed by these first experimental confirmations, the scientific attention on the study of possible magnetoelectric compounds increased, activating a prolific debate that anyhow remained confined to a little elite of scientists. The reasons of such lack of interest essentially depended on the very low intensity magnetoelectric coefficients spotted by the natural or artificial compounds studied.

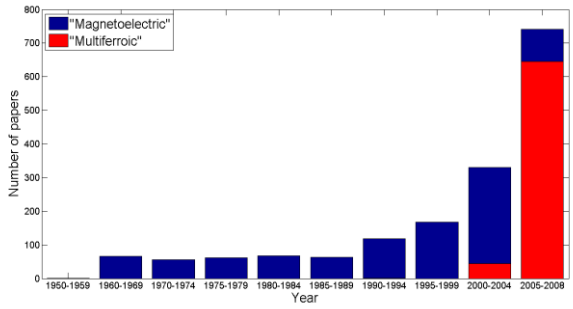

Figure II.1. Statistics reporting, as a function of the elapsed years, the number of scientific papers containing the keywords "magnetoelectric" (blue histogram) and "multiferroics" (red histogram). *[Image taken from en.wikipedia.org/wiki/Multiferroics].*

These unsatisfactory results are related to the intrinsic difficulty in obtaining magnetoelectric phases through standard synthesis techniques. As a consequence, the situation did not change until the achievement of new technological developments and instrumental innovations in the field of Material Science. For instance the born of epitaxial film deposition techniques (Molecular Beam Epitaxy (MBE), Pulsed Laser Deposition (PLD), Spray depositions etc. etc.) gave a new extraordinary pulse to the research. In 2001,

Nicola A. Spaldin organized the first special session on multiferroics at the American Physical Society's March meeting. The turning point occurred just two years later, by the appearance on the scene of both the so-called spontaneous magnetoelectrics and the strongly coupled magnetoelectrics. In 2003, the observation of the high spontaneous electrical polarization of the antiferromagnetic bismuth ferrite $BiFeO_3$ (BFO) [9], together with the detection of a very high magnetoelectric coefficient in terbium manganites $TbMnO_3$ [10] and Tb_2MnO_5 [11], opened the "golden season". Specifically BFO brought back to actuality a phenomenological definition [12] pointed out by Hans Schmid in 1994: the concept of multiferroism. Using his words, multiferroism is the *"... coexistence of two or more primary ferroic orders in the matter, namely (Anti)Ferromagnetism, Ferroelectricity and Ferroelasticity"* (and/or Ferrotoroidicity, trivial order). Hence it is worth to note that a system displaying coexistence of spontaneous electrical polaritazion (Ferroelectricity) and magnetic ordering in a wide or narrow (it does not matter) thermal regime is properly definable as multiferroic. This is precisely the case of BFO, which represents the first material in the history to have shown this property. As pictured in Fig. II.1, since 2003 the number of publications with "multiferroic" as keyword abruptly increased from zero up to few hundreds. Consequently a reshaping of the lexicon became mandatory to uniform the scientific communication and avoid incomprehension among researchers. **This process leaded to the born of the term multiferroic magnetoelectrics (Fig. II.2), referring to those compounds showing magnetoelectric effect and spontaneous electric and magnetic orders.** Between 2004 and 2010 many important scientists published wide and complete reviews trying to put order into such a variegate set of novel scientific results, also indicating the main ways for further discoveries [13,14,15,16,17,18].

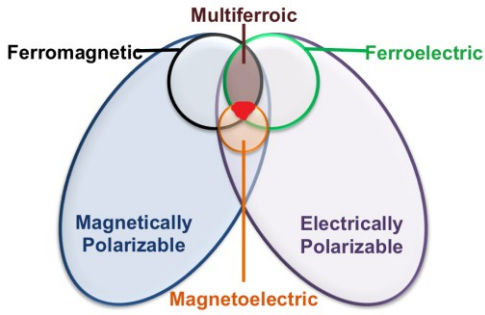

Figure II.2. The sketch shows, within the two heterogeneous families of magnetically and electrically polarizable materials, the little intersection set (filled in red) which identifies the narrow subcategory of multiferroic magnetoelectrics. *[Image taken from L. D. Martin Dalton Trans **39**, 10813-10826 (2010)].*

At present, magnetoelectric coefficients large enough to allow technological applications are reached only at very low temperatures or in composite materials or hetero-structures, where typically magnetostrictive and piezoelectric compounds are coupled. In these systems a specific study of the interplay between the ferroic degrees of freedom is needed, since linear elasticity models cannot be used to describe the responses on the atomic scale. Experimentally, the use of self-organized nanocomposites could offer a particularly efficient coupling between the phases [19]. Today the challenge is still represented by the perspective of achieving high magnetoelectric performances and intrinsic multiferroic character in a single phase near room temperature and without artificial heterostructures. Anyhow, besides the technological interest, it should not be forgotten the unique chance offered by multiferroics to the study of Solid State Physics, for what concerns both the understanding of the ferroic orders and their complex interactions.

B. Multiferroic Magnetoelectrics: the key role of Symmetry

The amount of natural multiferroic magnetoelectric compounds is very small: an empirical rule states that ferroelectric materials are usually non-magnetic, while spin-ordered systems seem not to allow ferroelectric distortions. The understanding of this behavior needs a description of the conditions allowing both ferroelectricity and magnetism to be present in a material. In an ionic crystal two kinds of interaction are present: short-range repulsions between the electronic clouds which favor a non-ferroelectric symmetric structure, and bonding interactions, which may stabilize the ferroelectric phase. At high temperatures, the former is dominant, inducing high symmetry (paraelectricity) phases also in ferroelectric systems first. The lowering of temperature causes a distortion that, in transition metal (TM) oxides, is usually due to the hybridization of TM *d* orbitals with the oxygen *2p* orbitals, inducing the off-centering shift of the cation. Noteworthy, the most favorable condition providing *d* orbital close in energy to the O *2p* -thus the insurgence of ferroelectricity- involves d^0 TM ions, proofed by the fact that most of the ferroelectric perovskites show such an electronic configuration (examples are perovskite containing d^0 ions like Ti^{4+}, Zr^{4+} and Nb^{5+}). On the other hand, it is clear that *d* orbital occupancy is a fundamental requirement for the occurrence of magnetic ordering. Such strong constraint limits the incidence of magnetoelectricity, but it is not the only one. The occurrence of both ferroelectricity and ferromagnetism requires very strict symmetry conditions. These arise directly from the Landau-Lifschitz theory, as anticipated in the Introduction. They rewrote the classification of the crystalline structure unifying the spatial symmetry and the magnetic (temporal) symmetry. By means of this operation the number of independent and non-trivial crystallographic magnetic structures increases to 1191, which correspond to 122 Shubnikov point groups [20].

Among these 122 degrees of freedom of the crystal nature, only 58 groups are invariant for transformations of spatial and temporal reversal but simultaneously allow the existence of non-null terms of the magnetoelectric coefficient (which is a second order tensor). In these groups the space and time inversion symmetry breaking occurs in general when an external

electric and magnetic fields are applied. This class of magnetoelectrics are called, *latent magnetoelectrics*.

Moreover, a little number of symmetry groups can be further distinguished, corresponding to those crystals in which spontaneous electric or magnetic polarization is present. Under such constraint, stricter than that of the former situation, the internal field induces the spatial or time inversion in the same crystallographic sites, leading to formation of missing spontaneous polarization. Herein the magnetoelectric coefficient is quite high, so that the coupling is particularly intense. These magnetoelectrics are called *semi-spontaneous magnetoelectrics.*

Finally, only 13 point groups (1, 2, 2', *m*, *m*', 3, 3*m'*, 4, 4*m*'*m*', *m*'*m*2', *m*'*m*'2', 6, and 6*m*'*m*') are intrinsically non-symmetric for time and space inversion operations. In this narrow class, the two orders are present and often characterized by a different origin. For this class the magnetoelectric coefficient, if present, is very low. The crystals of this class are called *spontaneous magnetoelectrics.*

Both spontaneous and semi-spontaneous magnetoelectrics may be correctly called *multiferroic magnetoelectrics* too; in literature they are also known with the appellative of *type-I* and *type-II multiferroics* respectively. Another diffuse labeling emphasizes instead the mechanism responsible for the occurrence of electrical polarization so that one can speak of *proper* and *improper ferroelectrics* referring to the corresponding categories. For the sake of clarity, and to dribble misunderstanding, I report below, in Table II.1, all the accepted nomenclatures corresponding to spontaneous and semi-spontaneous magnetoelectrics.

Table II.1. All the accepted scientific nomenclatures used to define the two categories of multiferroic magnetoelectrics.

MULTIFERROIC MAGNETOELECTRICS	
Spontaneous Magnetoelectrics	**Semi-spontaneous Magnetoelectrics**
Type-I Multiferroics	Type-II Multiferroics
Proper ferroelectric Multiferroics	Improper ferroelectric Multiferroics

C. If Ferromagnet fights, Antiferromagnet assists Magnetoelectricity

In addition to what has been said, electrical considerations must be taken into account for understanding the strong limitations affecting the multiferroic family. Many ferromagnetic oxides with perovskite structure are characterized by metallic properties. These materials have partially filled d^0 shells which in absence of particular orbital hybridization lead to high density of states at the Fermi level and thus to the conductive behavior. However, in a ferroelectric material, there is a voltage drop due to the electrical dipole. If the material is metallic, this voltage creates a charge flow that will set the drop to zero. Hence, ferroelectrics need an insulating medium. Otherwise, antiferromagnetic oxides are usually good insulators, and for this reasons they result to be natural candidates for proper or improper ferroelectricity. For this reason it is easier to find magnetoelectric compounds whose weak ferromagnetic properties are generated by a frustrated antiferromagnetic behavior or by spin canting of the antiparallel moments arrangement via antisymmetric effects as for example Dzyaloshinskii-Moriya (DM) interactions or Single Ion Anisotropy (SIA). Finally, structural considerations are also involved in the lack of multiferroic compounds. As previously anticipated, ferroelectricity often takes place as a low temperature distortion determined by an ion displacement from the center the polyhedra of coordination. However, the presence of unpaired electrons in the outer shell of several d^n transition metals induces a Jahn-Teller distortion which behaves as a competitive process with respect to the off-centering mechanism, for reasons not entirely clear. In conclusion, it seems that no other accessible ways different from choosing antiferromagnetic materials as basilar components in the realization of multiferroic and magnetoelectric compounds are effectively possible.

D. Conditions for the existence of Ferroelectricity in magnetic materials

The extensive list of restraining conditions reported in the preceding subchapters may seem discouraging to the researcher in the field of magnetoelectric materials, anyhow an increasing number of multiferroics has been synthesized in recent years, and this was made possible by the notion that additional structural or electronic driving forces can help magnetoelectricity to take place. The applied strategies follow two different paths: the first one leads to magnetoelectricity through the presence of two subsystems carrying electrical and magnetic properties separately (it is the case of proper ferroelectrics or type-I multiferroics); the second way involves ferroelectricity to be driven by a magnetic ordering process, as sometimes it happens in spiral or cycloidal magnetic systems (it is the case of the improper ferroelectrics or type-II multiferroics). In order to describe the general classes of magnetoelectric materials may be useful to consider the common ways to induce ferroelectric (FE) properties in a crystal:

- the presence of a transition metal (TM) with d^0 configuration, through the process previously described (Fig. II.3). In this case, it is difficult to introduce magnetism since unpaired electrons on the *d*-shell are required.

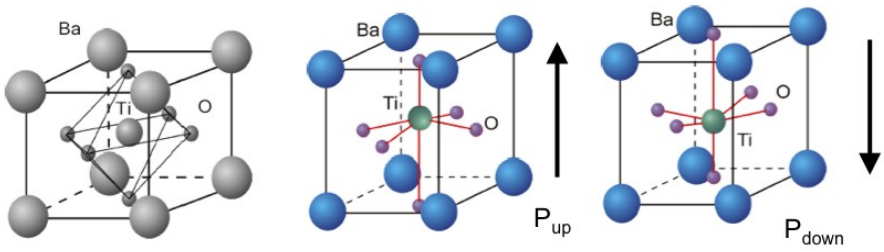

Figure II.3. Ti^{4+} off-centering in the $BaTiO_3$ ferroelectric perovskite.

- the introduction within the structure of Bi^{3+} or Pb^{2+} ions, that can induce FE through the stereochemical activity of their "lone pair" electrons. The $6s^2$ electronic shell tends to hybridize with the *2p* orbitals of oxygen anions, giving rise to highly directional bonds and electronic cloud polarization (Fig. II.4).

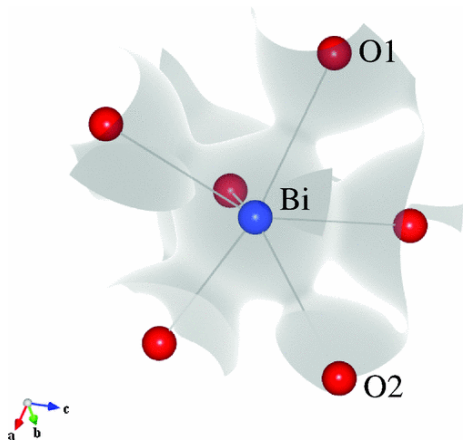

Figure II.4. Sketch of bismuth ion stereochemical effect on oxygen electronic clouds hybridization.

- the presence of *"geometric"* ferroelectricity, as it happens in $YMnO_3$[21], where FE is caused by a rigid rotation of the Mn-O coordination polyhedral induced by the small ionic radius of Y^{3+} (Fig. II.5).

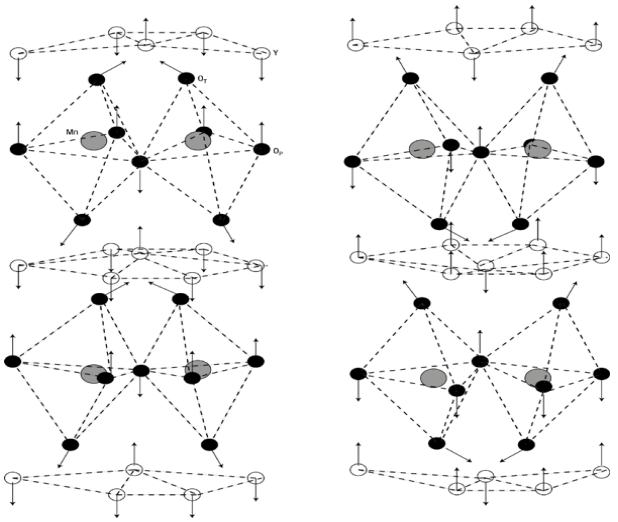

Figure II.5. Origin of the two enantiomorphous polarized states in $YMnO_3$ perovskite.

- in some cases FE can be induced by charge ordering, when inequivalent bonds are created between sites displaying different charges, just like in presence of a Peierls transition or magnetostriction. The resulting arrangement is polar, and an electrical dipole moment sets in (Fig. II.6).

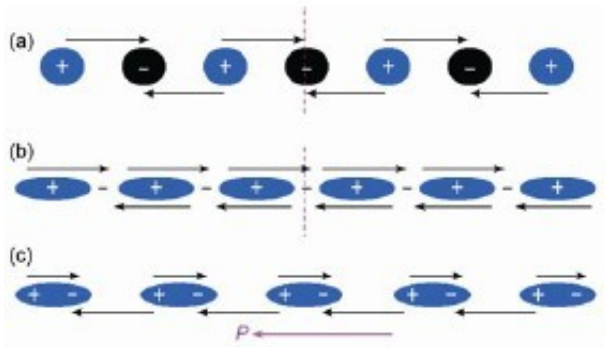

Figure II.6. Charge Ordering mechanisms in linear chain. (a) Site centered charge ordering (non-polar); (b) bond centered charge ordering (non-polar); (c) combination of site and bond centered charge ordering (polar).

Let us now consider some different classes of magnetic materials, arranged on the basis of the phenomenon which is likely at the origin of the ferroelectricity; these classes are reasonably good candidate to magnetoelectricity (ME).

D.1 Geometrical frustration

When ferroelectricity is induced by lattice distortions through the off-centering of ions, often magnetoelectricity may be achieved via a geometric frustration (e.g. in Kagomè lattices) of the spin structure, arranged in non-collinear ways. To this class of multiferroics belong the hexagonal manganites $RMnO_3$ (R = Rear Earth or Y), where the low size of the R ion yields a large deviation from the classical perovskite structure being likely at the origin of ferroelectric distortion. In this case, although the ordering temperatures of

ferroelectric and magnetic degrees of freedom do not coincide, a large coupling may be expected, since the ion at the origin of both the ferroic phenomena is Mn^{3+}. Also the class of compounds $K_xFe_5F_{15}$, so-called tetragonal tungsten bronzes fluorites class [22], belong to this category of ferroelectrics.

D.2 Lone pair

As it has been said, the introduction in a non-polar oxide of a $6s^2$ ion may induce ferroelectricity through the stereochemical activity produced by its electronic lone pair. The concomitant presence in the crystallographic framework of magnetically active atoms could produce magnetoelectric coupling. Examples include $BiFeO_3$ [23], $BiMnO_3$ [24,25], $PbVO_3$ [26], $BiMn_7O_{12}$ [27] and some Pb and Bi-based double perovskites of mine, new magnetoelectric compounds whose synthesis and characterization are discussed in detail in chapter *III.C*, *III.D* and *III.E* respectively.

D.3 Charge ordering

If magnetic ions are present in a dimerized charge-ordered system, the coexistence of magnetism can be established and may be coupled to ferroelectricity. In the case of $LuFe_2O_4$ [28], ferroelectricity is due to the lack of geometrical compensation in a triangular arrangement of mixed valence Fe^{2+} and Fe^{3+} ions. Ferrimagnetic behavior arises from the frustration of the antiferromagnetic interactions within the triangular Fe-O-Fe framework. For $(Pr,Ca)MnO_3$ [29], the possibility of charge-ordered based magnetoelectric behavior has been hypothesized under the name of a "Zener polaron state" [30]. In this model one electron is shared by the pair of neighboring Mn ions (which are in formal valence state 3+ and 4+), inducing a partial dimerization. Moving back and forth between them, the e_g electron orients in a parallel way the localized spins on the t_{2g} orbitals by the double exchange mechanism, making possible magneto-dielectric coupling. However, this hypothesis has not been verified by direct experimental observations due to high conductivity of the material at low temperatures. In addition, charge-ordered ferroelectricity

is suggested also in the well known ferrimagnetic compound Fe_3O_4 [31], occurring together with other physical changes at the Verwey transition temperature [32].

D.4 Magnetically driven magnetoelectricity

In magnetically driven magnetoelectrics, namely improper ferroelectrics and/or type-II multiferroic, FE is induced by magnetic ordering, so that in this class of materials the largest couplings are expected. The possible origins of this behavior are two distinguishable by matters of exchange interaction symmetry.

The first case is the FE driven by a-symmetrical Exchange interaction where formally:

$$P \approx e_{ij} \cdot S_i \times S_j. \qquad \text{(II.1)}$$

This occurs in the so called *bc-cycloids* and *ab-cycloids* systems; herein a inverse Dzyaloshinskii-Moriya effect,[33] operates whenever a non-collinear distribution of the spins is present, usually spiral magnetic structures (i.e. in which the spins rotate around an axis perpendicular to the propagation vector of the spiral),[34] requiring the direct action of the spin-orbit interaction. The induced electric polarization is orthogonal to the propagation vector and lies in the spiral plane. This mechanism is responsible of ME effect in systems like $TbMnO_3$ [10], $Ni_3V_2O_8$ [35], $MnWO_4$ [36], $BaNiF_4$ [37] and $DyMnO_3$ [38] in which the zigzag arrangement of magnetic moments is responsible for the occurrence of a net electric dipole moment in the structure (see Fig. II.7).

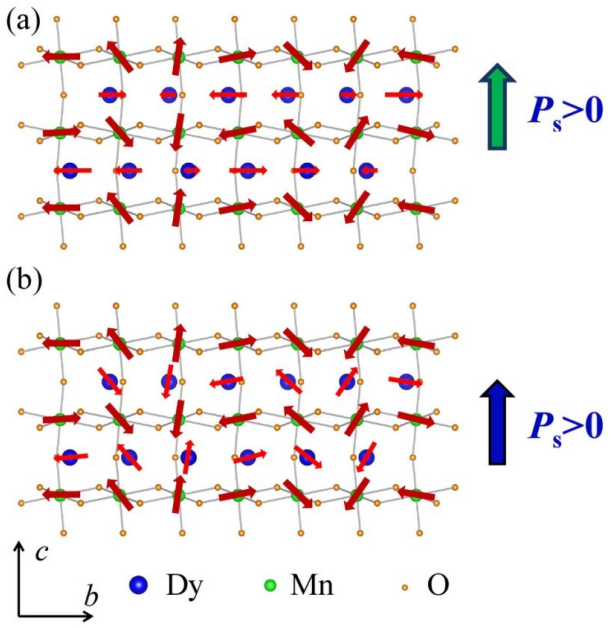

Figure II.7. Sketch of the possible magnetic configurations for Dy and Mn spin in $DyMnO_3$. Both these configurations are non-collinear. This induces a spatial inversion symmetry breaking and so the ferroelectricity.

For the second case, FE arises from a symmetrical exchange interaction:

$$P_a \approx S_i \cdot S_j \qquad \text{(II.2)}$$

and lies in the same plane of the magnetic interaction. Basically, it is a *magnetostrictive effect* and can take place in collinear magnetic structures; in such a case FE does not require the presence of spin-orbit coupling. These systems are usually characterized by a E-type AFM structure, normally stable at very low temperature.

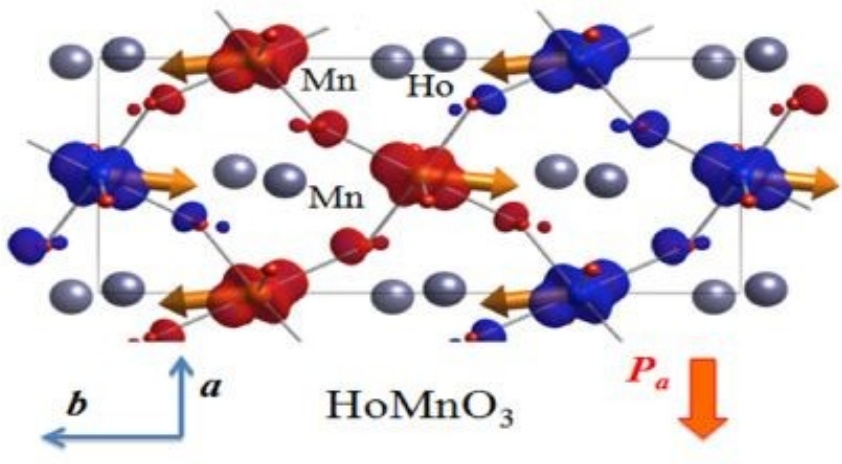

Figure II.8. Schematic representation of the direction of polarization of Mn in orthorhombic E-type AFM $HoMnO_3$ perovskite.

For instance, in $HoMnO_3$ [39], magnetostriction generates a multiferroic behavior by means of a periodic collinear spin arrangement of the up-up-down-down type that can induce electric polarization (see Fig II.8). Even if characterized by a high magnetoelectric coupling coefficient, magnetically driven magnetoelectrics unfortunately display both low electrical saturation polarizations ($1 \div 6\ \mu C/cm^2$) and very low Curie-Weiss transition temperatures.

E. The Perovskite lattice: the best fitting cloth for Multiferroic Magnetoelectrics

Most of the mechanisms presented in the previous chapter are characterized by a significant lowering of the space and time symmetry making possible the existence of magnetoelectricity. However such phase transformations, in order to be stabilized, has to be tolerated by the crystallographic structure of the compound. It is not a coincidence that almost all the samples reported as notable examples in the previous subchapter, are based on the perovskite structure.

The term "perovskite" namely indicates the mineral of calcium titanate ($CaTiO_3$) and it was attached by the German mineralogist Gustav Rose in 1840 in honor of the Russian Imperial Court Minister and collector Lev Von Perovskiy, the first who classified such kind of crystals gathered on Ural Mountains. Nowadays many minerals, constituents earth crust's deeper stratum, crystallize on the basis of the perovskite structure. Hence, the terms perovskite has been promptly extended to a large class of natural compounds to which many other artificially synthesized by men have been added. The scientific interest arose from the observation of many interesting and intriguing properties from both the theoretical and the application point of view. Colossal magnetoresistance, ferroelectricity, superconductivity, charge ordering, spin dependent transport, high thermo-power and the interplay of structural, magnetic and transport properties are commonly observed features in this family. Surprisingly perovskite seems to be the perfect cell for most of the exotic properties of the matter as well as specifically for multiferroic magnetoelectricity.

The reasons of this success are purely structural. Pictured in Fig. II.9, the perovskite structure is an ideal cubic cell indentified by the basic unit formula ABO_3. A and B indicate two different cation in which the A ionic radius is larger than the B one; O indicates the oxygen anions. The ratio between A-O and B-O bond distances is exactly equal to $\sqrt{2}$ in cubic symmetry.

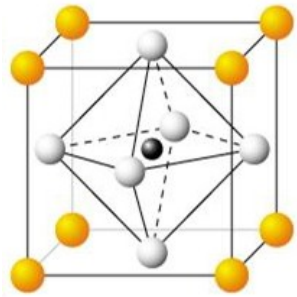

Figure II.9. The ideal perovskite cubic cell. The black, white and golden spheres represent the B, O and A ions respectively.

The main characteristics are the high coordination numbers: respectively 12 for A-cation and 6 for B-cation, which yields extraordinary density to the structure. Moreover, from a geometrical point of view, this spatial distribution guarantees high tolerance to chemical substitutions allowing to insert cations of different valence states and ionic radii. Nevertheless, the set of possible substitutions is limited by two following empirical rules (Eqs. II.3 and II.4) pointed out by Goldschmidt, in the later 1920 [40]:

$$0.75 \leq \frac{r_A + r_O}{\sqrt{2}(r_B + r_O)} < 1.05 \qquad \textit{(Tolerance Factor)} \qquad \text{(II.3)}$$

$$\frac{r_B}{r_O} > 0.425 \qquad \textit{(Ochtaedral Ratio)} \qquad \text{(II.4)}$$

where r_A, r_B and r_O are the ionic radii of the constitutive elements.

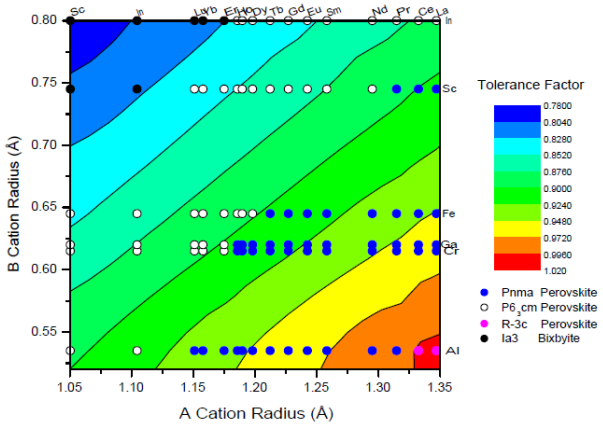

Figure II.10. The wide range of accepted values for tolerance factor as a function of the A and B cationic radii for different A and B ions substitutions. The blue, white, pink and black circles label the predicted crystallographic structure. *[Image taken from Mark Levy Ph.D Thesis (2005)].*

This extremely wide range of existence, sketched in Fig. II.10, clearly demonstrate the perovskite capability of meta-stabilizing significant distortions of the unitary cell and consequently deep modifications of the spatial symmetry. Specifically, several perovskitic compositions have been synthesized within these intervals and, in particular, three principal spatial symmetries have been observed: the cubic, the orthorhombic and the rhombohedral one. In Figs. II.11, II.12 and II.13, the most important perovskitic oxides, in terms of physical properties, are reported for each crystallographic structure.

Compound	Space Group	Lattice Parameter (a) Å
$CeCrO_3$	$Pm\bar{3}m$	3.89
$CeFeO_3$	-	3.9
$CeGaO_3$	-	3.879
$GdMnO_3$	-	3.82
$PrCoO_3$	$Pm\bar{3}m$	3.78
$PrMnO_3$	-	3.82
$SmCoO_3$	$Pm\bar{3}m$	3.75
$SmCrO_3$	$Pm\bar{3}m$	3.86
$SmVO_3$	-	3.89

Figure II.11. A list of cubic perovskite oxides. *[table taken from Mark Levy Ph.D Thesis (2005)].*

Compound	Space Group	Lattice Parameters Å		
		a	b	c
$CeAlO_3$	P4/mmm	3.7669	3.7669	3.7967
$CeVO_3$	Pbnm	5.514	5.557	7.808
$CrBiO_3$	Tetragonal	7.77	-	8.08
$DyAlO_3$	Pbnm	5.21	5.31	7.4
$DyFeO_3$	Pbnm	5.302	5.598	7.623
$DyMnO_3$	Pnma	5.842	7.378	5.28
$ErFeO_3$	Pbnm	5.263	5.582	7.591
$EuAlO_3$	Pbnm	5.271	5.292	7.458
$EuFeO_3$	Pbnm	5.372	5.606	7.685
$GdAlO_3$	Pbnm	5.247	5.304	7.447
$GdCoO_3$	-	3.732	3.807	3.676
$GdCrO_3$	Pbnm	5.312	5.515	7.6 15
$GdFeO_3$	Pbnm	5.349	5.611	7.669
$GdScO_3$	Pnma	5.742	7.926	5.482
$HoFeO_3$	Pbnm	5.278	5.591	7.602
$LaCrO_3$	Pnma	5.479	7.7562	5.5161
$LaFeO_3$	Pnma	5.5647	7.8551	5.556
$LaGaO_3$	Pbnm	5.5245	5.4922	7.774
$LaMnO_3$	Pbnm	5.5367	5.7473	7.6929
$LaRhO_3$	Pbnm	5.524	5.679	7.9
$LaScO_3$	Pbnm	-	-	-
$LaTiO_3$	Pbnm	5.6301	5.5844	7.901
$LaVO_3$	Pnma	5.5518	7.848	5.554
$LuFeO_3$	Pbnm	5.213	5.547	7.565
$NdCoO_3$	Pnma	5.3312	7.5482	5.3461
$NdCrO_3$	Pnma	5.4798	7.6918	5.4221
$NdFeO_3$	Pnma	5.587	7.761	5.4505
$NdGaO_3$	Pbnm	5.4276	5.4979	7.7078
$NdMnO_3$	Pnma	5.7119	7.589	5.4119
$NdScO_3$	Pbnm	5.555	5.744	7.972

Figure II.12. A list of orthorhombic perovskite oxides. *[table taken from Mark Levy Ph.D Thesis (2005)].*

Compound	Space Group	Lattice Parameters Å			Angles		
		a	b	c	α	β	γ
$BiFeO_3$	R3CH	5.5775	5.5775	13.8616	90	90	120
$CeFeO_3$	-	3.9	-	-	90	90	90
$CrBiO_3$	-	7.77	-	8.08	90	90	90
$GdAlO_3$	-	10.56	10.56	12.89	90	90.6	90
$GdCrO_3$	-	-	-	-	-	-	-
$LaAlO_3$	$R\bar{3}c$	5.3647	-	13.1114	60.1	90	90
$LaCoO_3$	$R\bar{3}CR$	5.3416	5.3416	5.3416	60.99	60.99	60.99
$LaNiO_3$	$R\bar{3}CH$	5.4573	5.4573	13.1601	90	90	120
$NdAlO_3$	$R\bar{3}c$	5.3223	5.3223	12.9292	90	90	120
$PrAlO_3$	$R\bar{3}c$	5.3337	5.3337	12.9766	90	90	120
$PuAlO_3$	-	5.33	-	-	56.07	90	90

Figure II.13. A list of rhombohedral perovskite oxides. *[table taken from Mark Levy Ph.D Thesis (2005)].*

From another point of view, also the possibility to exploit more than just one simple substitution on the A and the B site represented an opportunity of development. In principle this means that also quaternary and pentenary compounds based on the perovskite structure, e.g. $(A_{1-x}A'_x)(B_{1-x}B'_{1-x})O_3$ where A, A', B and B' are different metallic cations, can be produced and stabilized. In the latest years, many complex perovskites have been studied following this idea but with different perspectives. In particular, the so-called *quadruple perovskite* class, where the specification "quadruple" refers to the simple perovskite unit formula ABO_3. This class is characterized by the chemical formula $AA'_3(B,B')_4O_{12}$ and theoretically crystallizes in a cubic cell with lattice parameter $a_{qp} = 2a_{sp}$ (so quadruple perovskite owns a 8 times larger cell compared to the simple perovskite).

In this family of heterogeneous compounds, phenomena of multiple ordering, precisely spin, charge and orbital ordering, are often recursive. Important members are the manganites $(NaMn^{3+}_3)(Mn^{3+}_2Mn^{+4}_2)O_{12}$ [41], $(CaMn^{3+}_3)(Mn^{3+}_3Mn^{+4}_1)O_{12}$ [42], $(LaMn^{+3}_3)(Mn^{+3}_4)O_{12}$ [43].

Other types of quadruple perovskites are the Pb and Bi-based ones, as for example $BiMn^{+3}_3)(Mn^{+3}_4)O_{12}$ [27] or $(PbMn^{+3}_3)(Mn^{+3}_3Mn^{+3})O_{12,}$ which display promising properties for the study of multiferroism, magnetoelectricity and/or magnetoresistance.

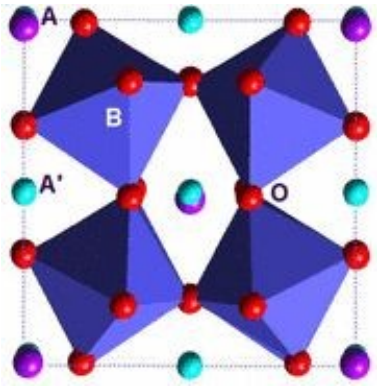

Figure II.14. An example of quadruple perovskite structure. In $(BMn^{3+}_3)(Mn^{3+}_4)O_{12}$ the A' site ion is square planar coordination and the high octahedral tilt is well-visible.

Moreover, there are also the so-called class of the *double perovskite*s that represents one of the most significant frontier in the field of multiferroic materials. Double perovskites are usually identified by the chemical formula $A_2BB'O_6$, where B and B' are usually distinct metallic cations belonging the third, fourth and fifth period; double perovskite basic cell is an orthorhombic cell with lattice parameters $a_{dp} = b_{dp} = \sqrt{2}a_{sp}$ and $c_{dp} = 2a_{sp}$ (so double perovskite owns a 4 times larger cell compared to the simple perovskite one). This structure arises from a tilt of the octahedra of coordination BO_6 and $B'O_6$.

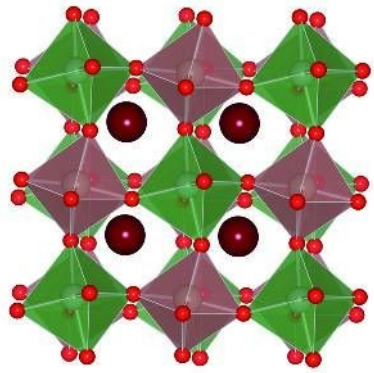

Figure II.15. The highly distorted double perovskite structure of Bi_2MnReO_6. Such distortion, induced by the Bi^{3+} lone pair stereochemical effect, is responsible for ferroelectricity.

The coexistence in the double perovskite B and B' sites of different magnetic interactions often produces an enhancement of the ordering Curie or Néel temperature, even if this sometime happens at expenses of a higher magnetic complexity. This is an extraordinary improvement as far as the seek of a stability range expansion is concerned. Examples of such compounds it will be widely discussed in the following chapter, being the main subject of my Ph.D activity.

F. The need of high-pressure / high-temperature (HP/HT) syntheses

Since the optimal multiferroic magnetoelectric material or hetero-structure is yet to come, scientists have been working to find the reasons of such difficulties: the main issue is still represented by the difficulty to observe the superposition of an high temperature multiferroic phase and the presence of a high magnetoelectric coupling which seem to be competitive characteristics. The solution may be given by the discovery of even more complex perovskite systems. As it has been said, the more these compounds are complex the rarer are in Nature. In parallel, standard high-temperature synthesis techniques in controlled atmosphere had spotted a strong inefficiency in the production of phases with deep structural modifications often characterized by an unsuitable chemical composition and high symmetry distortions.

In this scenario, if for example the quadruple perovskite manganites listed in the previous chapter are concerned, this inefficiency seems to be related to the stabilization of the Mn^{3+} ions on the A' site in square planar coordination (Fig. II.14). This configuration could not be generally obtained by solid state reactions carried out in normal condition. Similarly the effective number of producible double perovskite based compounds varying the metallic chemical substitutions is relatively tiny, either due to limitations regarding the stabilization of too small ions on the A site or even too big ions on the B and B' sites or again to the possibility of attaining unusual cationic oxidation states. A suitable remedy goes through an extension of the perovskite tolerance factor, which generally implies an increasing of the phase stability over strong structural distortions. In most of the cases, this becomes viable by exploiting the action of other external parameters during the synthesis process: for instance, under intense mechanical stresses, the formation of unattended lower symmetries may be observed. I can apply mechanical stress both in 2D and 3D systems precisely by means of two different mechanisms: the stress/strain effect yielded by the intrinsic lattice mismatch at the interface between a substrate and the deposited perovskite film, and/or equivalently by an external isostatic pressure application on a bulk sample instead. These are the recipes more followed nowadays by scientific groups. For the sake of honesty, while the production

of 2D heterostructures is the most immediate and effective method for studying a multiferroic device (substrate + functional film) as well as for the direct technological scalability, on the other hand the bulk multiferroic magnetoelectrics characterization gives the unique opportunity to investigate the intrinsic physical properties and represents also a basilar step towards the resolution of the still opened issues.

F.1 The Multianvil Walker-type press

In the latter phrase of the previous paragraph the reader has to intend the sense of my synthesis activity. What I did is to produce several Pb and Bi-based double perovskite multiferroic magnetoelectrics through high-pressure / high-temperature syntheses by means of a Multi-Anvil (MA) Walker-type press, in hand to IMEM–CNR in Parma (pictured in Fig. II.16).

Figure II.16. The MA Walker-type press at IMEM-CNR.

This apparatus is a highly versatile system for the synthesis of bulk materials under variable isotropic temperature and pressure conditions in the range of $2.5\ GPa < P < 25\ GPa$ and 0

°C < T < 2200 °C. The maximum (P,T) values correspond to the conditions occurring at a depth of *750 Km ÷ 800 Km,* approximately in the boundary zone between the lower region of the Earth crust and the higher region of the Earth upper mantel. Herein the solid state of the matter essentially crystallizes in spinel-based or perovskite based structure. The experimental difficulty occurring in the artificial realization of intense pressures is related to a non-trivial reason: an isotropic force could be easily applied through a fluid compression but for such a high pressure the stable state of the matter is the solid one (neither liquid nor vapor phases do exist). To avoid this drawback I shall transform a directional force into an isotropic force only by means of solid components. The winning idea struck to the American mineralogist David Walker, that in 1991 described his new module designed for producing new synthetic minerals [44], later called Walker-type MA module. The Walker Module is able to uniformly decompose and amplify an unidirectional pressure into an almost isostatic pressure through three different solid media with increasing hardness.

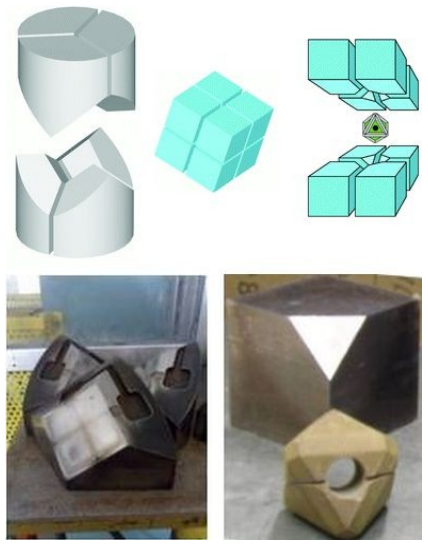

Figure II.17. Scheme of force decomposition elements constituting the Walker type module. In the lower part of the figure, from left to right some tempered wedges, a tungsten carbide cube and the correspondent MgO octahedral reaction cell are shown.

This MA system converts an axial load over a circular surface, due to the controlled push of a cylindrical piston managed by an oil-dynamic circuit, into a three-components force through a set of six wedges, made of tempered steel, whose combination generates a cubic cavity filled by eight truncated tungsten carbide cubes which in turn are assembled together to create an inner octahedral cavity with a four components resultant force, one by one directed perpendicular to the four triangular faces of the octahedron (the mechanical elements are pictured in Fig. II.17). Inside this cavity is putted the reaction cell, a porous magnesium oxide octahedron pierced in its center from one side to the other by a cylindrical cavity in which is located a cylindrical graphite oven which will contain the platinum (or gold) capsule, the ultimate holder of the reactants. In the middle region of the cylinder, where capsule lays, the pressure is quasi-isostatic with a maximum P gradient along the height of the cylinder of about *0.1 GPa/cm* (calculated for a pressure intensity of 6 GPa). The heating is achieved by Joule effect by means of a power unit that connects the upper wedges to the lower wedges via the sole non-insulated path that goes through the two opposite cubes pushing on the pierced octahedral triangular faces where the graphite oven slightly extrude the surface. This electrical control of temperature allows to manage the temperature exactly around the core of the reaction cell, without heat dispersions along the massive anvil structure.

The typical synthesis procedure is characterized by three consequential operations, which are mandatory stages to achieve reproducible results and to prevent mechanical or structural damages:

1. First of all, the pressure is gradually increased from 100 kPa (1 bar, room pressure (RP)) to the chosen set-point pressure of reaction (e.g. 6 GPa) with a typical ramp rate in the range of *500 Pa/m ÷ 700 Pa/m*.

2. Once the set-point pressure is reached, the system is Joule-heated from Room Temperature (RT) to the chosen set-point temperature and then is kept stable for the chosen reaction time (usually few hours).

3. At the end of the reaction, the system is abruptly quenched down to RT by switching off the power unit (or in few cases, the system temperature is slowly decreased with a controlled thermal ramp). Only when the measured external temperature on the outer surface

of Walker-type module is equal to the internal temperature, the pressure is slowly released to RP with a velocity of 300 Pa/min.

The main point to underline is the role of the thermal quenching. This operation usually is applied to “freeze” the obtained HP phase hopefully, since often the RP stable phase owns different crystallographic structure with respect to the HP one; in other words this is an operation of perovskite meta-stabilization. In most cases the final meta-stable phase has an important range of meta-stability. In all the studied compounds no phase separation or transition has been observed induced by thermal variations within the wide interval between 5 K and 600 K. The latter fact is fundamental datum because it preludes to long lasting performances and a complete applicability of these materials also in technology.

In spite of my consciousness about the extraordinary potentialities offered by the MA press, the downside is represented by the straightforward analysis of the time-cost factor. In fact a single HP/HT synthesis takes almost three days from the precursors preparation to the sample extraction whenever in parallel each component of the reacting cell is unavoidably destroyed and cannot be re-used anymore. This gives an idea about the effort being behind a metastable perovskite production and the continuous consumer products supplies that it unavoidably implies. In the actual Italian Research Era this is not a negligible issue.

G. The criticalities in Multiferroic Magnetoelectrics characterization

The production of novel bulk multiferroic magnetoelectrics by means of HP/HT synthesis is just the initial link of a long work chain. The synthesis products are obtained in form of polycrystalline pellets with a variable range of crystallinity and purity. This necessarily means that different thermodynamic conditions shall be explored for each sample, in order to achieve high purity levels and sufficiently good degrees of crystallinity. Once the optimal conditions are found, the later stage is to investigate the structural properties, principally exploiting the joint use of Single-crystal and powder X ray Diffraction (PXRD) together with Neutron Diffraction and Synchrotron Light experiments at European and International facilities (ILL, ESRF, ISIS and NIST, etc. etc,). In fact, as discussed in the previous subchapter, the knowledge of the crystallographic symmetry suggests about the chances of obtaining proper or improper ferroelectrics compounds, while the observation of high structural distortions (for example octahedral tilt and rotation) may suggest the existence of other structural/magnetic effects. Some of these could be responsible for a series of peculiar mechanisms typical of magnetoelectricity: Jahn-Teller distortions, bond hybridizations or also charge ordering, orbital ordering, spin ordering processes, or again spin-coupling effects possibly responsible for magnetocrystalline anisotropy, like Single Ion anisotropy (SIA), and second order contributions to the perovskite magnetic character as for instance Dzyaloshinskii-Moriya interaction (DM).

For all these reasons, the reader will surely understand the importance of such study and it will be conscious of the time investment need in this research. After all is said or done, the structural knowledge still remains a challenging and strategic aspect. Moreover, every magnetoelectric material requires a complete experimental investigation of both the magnetic and the electrical properties. For what concerns magnetism the use of SQuID magnetometry supported by some auxiliary local techniques (Mössbauer spectroscopy, NMR and in the case of a highly crystalline sample Raman spectroscopy) results to be a very incisive method since it often fulfills very efficiently its functions. By the way, the same thing cannot be said for what concerns the electrical properties. Nowadays in

literature, examples of complete electrical characterization of multiferroic materials are extremely rare or rather missing in spite of the large number of publications per year. This depends on several intrinsic criticalities of such kind of measurement, criticalities that I have omitted until now. As previously introduced, ferroelectricity and ferromagnetism are two competing phenomena: ferroelectricity is a polar character of a dielectric/insulating material where electrons are all paired in covalent bonds, while ferromagnetism requires high numbers of free (unpaired) electrons and consequently a semi-metallic or low-gap semi-conducting behavior. This is why in proper ferroelectrics, distinct ions usually contribute to magnetism and ferroelectricity, while in improper ferroelectrics, on the contrary, the occurrence of the magnetic order, typically characterized by a complex magnetic structure (spiral magnetism or frustrated magnetism), is responsible for a dramatic modification of the spatial symmetry, even though confined at very low temperatures. In the former case (i.e. proper ferroelectrics), the dielectric properties are difficult to be measured because of the free carriers large number and thus a significant conductive behavior of the charge transfer. If the pyroelectric and polar properties are considered, the request of insulating character becomes an important constraint instead. In fact, if an electric bias is applied on a material with a possible polar structure but simultaneous high conductivity, the current flow overwhelms the polar current and drops it to zero, so that no evidences of polarity can be recorded. In the extreme conditions of a quasi-metallic system, pyroelectric and ferroelectric characterizations are even impossible operations. This colossal drawback imposes the researcher a fundamental question: How may I extend the number of investigable proper ferroelectrics, even when they are not good insulators?

Fortunately, an answer exists and goes through a simple but effective trick of the trade. The idea consists in the separation between the dielectric and ohmic response of the material. In terms of current intensity, they are described by completely different voltage dependent signals:

$$I = \frac{1}{R} V \tag{II.5}$$

$$I = \frac{dQ}{dt} = C \frac{dV}{dt}. \tag{II.6}$$

If both equations are integrated as function of time, one obtains:

$$Q = \frac{1}{2R}V^2 \tag{II.7}$$

$$Q = CV. \tag{II.8}$$

Consequently, after a Charge vs. Voltage (*Q-V)* measurement: an ohmic or low-gap semiconducting material will display a parabolic trend (Eq. II.7 and Fig. II.18(left-side)), while a linear behavior will be observed for a pure dielectric material (Eq. II.8 and Fig. II.18(right-side)). Hence, for a sample characterized by a superposition of dielectric and ohmic characters, i.e. in first approximation most of the known multiferroics, a convolution of these two trends should be expected: (e.g. it is the case also of a capacitor showing robust capacitive losses). In this scenario, one regime can be distinguished from the other by means of dynamic voltage pulse of variable frequency. In the low frequency regime the resistive nature will be favored whereas in the high frequency regime the dielectric part will dominate. In other words by means of a proper (fast) AC voltage signal I am able to read the dielectric response of the material which includes also information about the possible polarization of the system, cutting out the ohmic contribution.

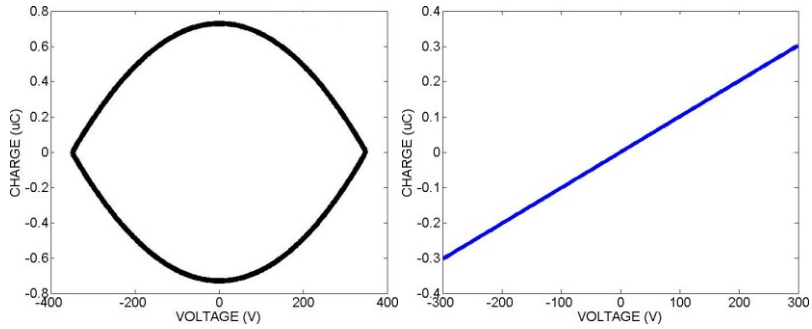

Figure II.18. Typical charge vs. voltage dynamic measurement of a ohmic material (left-side) and a dielectric material (right-side).

G.1 The AIXACCT Ferroelectric Tester

G.1.1 An overview into the Thin-Film Analyzer 2000E

The instrument I exploited to carry out these studies is the Thin-Film Analyzer 2000E (TFA) equipped with the Ferroelectric Module, produced by the German company AixACCT Systems GmbH. This versatile hardware/software package is thought for the ultimate characterization of thin films piezoelectric, pyroelectric and ferroelectric devices, but I have extended its functionalities in order to analyze also bulk samples (e.g. ours multiferroics). In principle a variety of measurement systems are designed with the TFA system as core component to fulfill different measurement tasks (e.g. thin films and MEMS devices, bulk ceramics, and multilayer actuators). For this purpose the TFA can control external hardware components like a temperature controller or a high voltage amplifier, and reads additional data from displacement, temperature, or force sensors. To summarize the experimental methods of this powerful tester, one has to consider that electrical and electromechanical characterization of dielectrics materials are the decisive factors to investigate their suitability for piezoelectric or pyroelectric and ferroelectrics sensor and actuator devices.

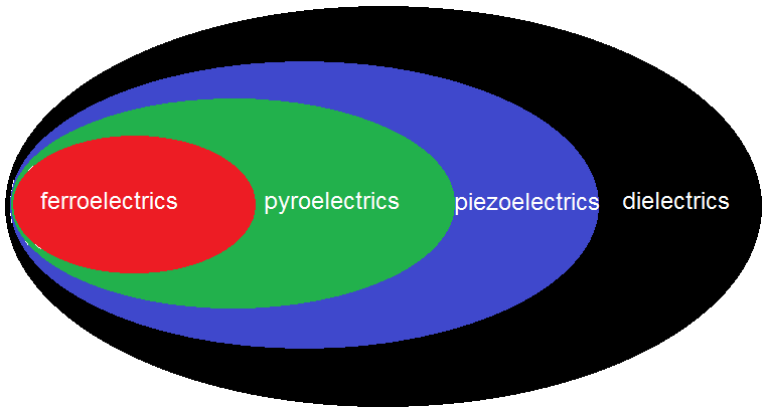

Figure II.19. Classes of dielectric materials. They are distinguished by the non-polar (dielectrics), induced polarization (piezo-), spontaneous irreversible polarization (pyro-) and spontaneous reversible polarization (ferro-) characters.

Substantial for electrical characterization of a sample is the measurement of its current or charge response due to an applied electrical excitation voltage. In piezoelectrics, the electromechanical response can be measured either by applying an electrical excitation signal and measuring the samples mechanical displacement or by applying a mechanical strain and recording the resulting charge displacement. The first method is commonly used as it allows the simultaneous electrical and electromechanical characterization. I try to give an idea of the order of magnitude of the current this system have to record by means of a simple example.

Let us consider the magnitude of the current *I,* given by the charge *Q,* flowing during a polarization reversal in a ferroelectric capacitor; it can be calculated as:

$$Q = D \cdot A \approx P \cdot A \rightarrow I = \frac{dQ}{dt} = A \cdot \frac{dP}{dV} \cdot \frac{dV}{dt}, \tag{II.9}$$

where *A* is the area of the capacitor, *P* the polarization of the material, *V* the applied voltage and *dV/dt* the slew rate of the signal form that is applied.

Based on a typical thin film sample capacitor geometry with an area $A = 0.25\ cm^2$, an operating voltage of *3 V* and a remanent polarization value $P_r = 30\ \mu C/cm^2$ of the material, the switching charge is $Q_{SW} = 150\ nC$. Choosing a triangular excitation signal with *100 Hz* frequency the average current magnitude is roughly calculated as:

$$I = \frac{60\mu C/cm^2 \cdot 0.0025 mm^2}{3V} \cdot \frac{3V}{0.0025s} = 60\ \mu A\ . \tag{II.10}$$

Due to the switching process around the coercive voltage V_C, *dP/dV* is not constant and the peak switching current will increase in one or two orders of magnitude. Besides the current magnitude, it is necessary to know the bandwidth of the current in order to decide how the

current can be recorded. The frequency spectrum of the current will define the bandwidth requirements for the recording amplifier. Furthermore, the noise and ground bouncing is an important aspect, which will finally result in the estimation of the signal-to-noise ratio (SNR). These parameters all together decide how well the electrical properties of a piezo or ferroelectric capacitor can be determined. There exist three established methods to record the charge and current response of the sample: the Sawyer Tower method, the Shunt method and the Virtual Ground method.

- Sawyer Tower Method

The Sawyer Tower measurement circuit is based on a charge measurement method which relies on a reference capacitor in series with the ferroelectric capacitor. The voltage drop at the reference capacitor is proportional to the polarization charge, as defined by $V = Q/C$. But if the voltage on the reference capacitor increases, the voltage at the sample decreases (back voltage effect). Therefore, the reference capacitor has to be much larger than the measured capacitor. For instance, if the reference capacitor is 100 times larger, the voltage drop is about *1 %*. This means the reference capacitor has to be adjusted to each sample. The Sawyer Tower method can be used up to high speeds, which is primarily limited by cable reflections. As parasitic effects, cabling capacitances of the wiring between sample, reference capacitor and the recording amplifier are in parallel to the reference capacitor. For small capacitors, the capacitance of the ferroelectric material is blinded in the total measured capacitance. Furthermore, it is difficult to get precise reference capacitors which typically have several percent tolerance, and in addition, the cable capacitance has to be added to this capacitance. Moreover, the input resistance of the voltage measurement device is in parallel to the reference capacitor. This loads to a discharge with a corresponding time constant, therefore the Sawyer Tower method is less suitable for slow measurements.

- Shunt method

The Shunt measurement substitutes the reference capacitor of the Sawyer Tower circuit by a reference resistance (shunt resistor). This measurement method is a current based method thus the switching current is measured as a voltage drop at the shunt resistor ($V = IR$), and integrated to get the polarization charge Q. Similar difficulties as in case of the Sawyer Tower setup appear. Though it is easier to get precision resistors, the resistance value of

choice depends not only on the sample capacitance but also on the excitation frequency. Thus, the voltage drop increases with increasing frequency and the time constant of ferroelectric capacitor and shunt resistor influences the result at higher speed. Additionally, the cable as well as the input capacitance for the voltage measuring device are in parallel to the reference resistor. Therefore accurate measurements for large systems are possible but become increasingly difficult in case of small areas, where the parasitic capacitances come into effect.

- The aixACCT solution: Virtual Ground method

The two peculiar limits of the presented methods, i.e. the difficulty to measure small ferroelectric capacitors or anyhow there are capacitance losses, can be prevented by a Virtual Ground based circuital methodology.

The Virtual Ground method uses a current to voltage converter which is constituted by current measurement using an operational amplifier with feedback resistor (Fig. II.20). The output of the current to voltage converter is connected to the inverting input of the operational amplifier via the feedback resistance, the non inverting input is connected to ground. The voltage difference between both inputs is ideally zero but in reality just a few microvolts. Therefore, the inverting input is virtually on ground level. This is helpful for the measurement -especially of small capacitors- as the cable capacitance is physically in place but electrically ineffective, because both electrodes of the capacitor are kept on the same potential. Also the sample is always applied to the full excitation voltage, since there is no back voltage. For high speed measurements, or voltage pulses, the inductance of the setup and the impedance mismatch caused by the sample and sample holder will lead to reflection on the cable and thus to a measurable change of the results related to the setup. Also the stability, bandwidth, and phase shift of the operational amplifier must be taken into account. However, as a whole, the Virtual Ground method enables the highest precision for ferroelectric measurements.

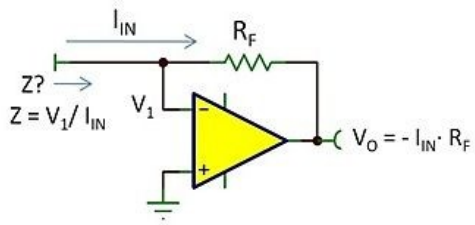

Figure II.20. Equivalent circuit of the Virtual Ground Feedback system.

For all these reasons, matching the aim of the study, Virtual Ground Feedback is used as integral part of aixACCT Measurement System.

G.1.2 A brief measurements description

A list of the TFA specifics is available on the Web at Ref. 45. The reader shall refer to it as a guideline of the methodology used for the presented ferroelectric characterization. In this paragraph, I just want to underline the wide range of instrumental functionalities, which in this configuration allow to perform several dynamic and static charge, current and capacitance measurements:

- Dynamic Hysteresis Measurement (DHM)
- Pulsed Measurement (PUND)
- Static Hysteresis Measurement (SHM)
- Leakage Current Measurement (LM)
- Capacitance Measurement (CM)

In my laboratory, each of them can be performed at two different thermal conditions: at room temperature and at liquid nitrogen temperature. This is a great chance in order to study also low-gap semiconducting samples as some multiferroics; in such a case I can opt for the

low temperature set-up, since a dielectric characterization requires quite high sample resistivity to be carried out. In addition, the system can also work at two different voltage magnitude intervals: specifically the low-*V* regime from *10 mV* to *20 V* and high-*V* regime from *5 V* to *2 kV*. These two configurations give me the possibility to study a wide set of samples with different thickness: from the thinnest films (around 1 *nm*, by means of the low-*V* circuit) up to bulk ceramic hard ferroelectrics (up to few *mm,* by means of high-*V* set ups).

For the sake of the Thesis readability, I just focus the attention on a brief description of the most peculiar and unusual type of measurement among them: the DHM. This dynamic charge measurement for recording hysteresis loops, exploit an excitation bias like a triangular signal (or sinusoidal). The range of signal frequencies, guaranteed by the FE module, goes from 10 mHz to 5 kHz. There will be a prepolarization pulse and three bipolar excitation signals generated if the default settings are used (see Fig. II.21).

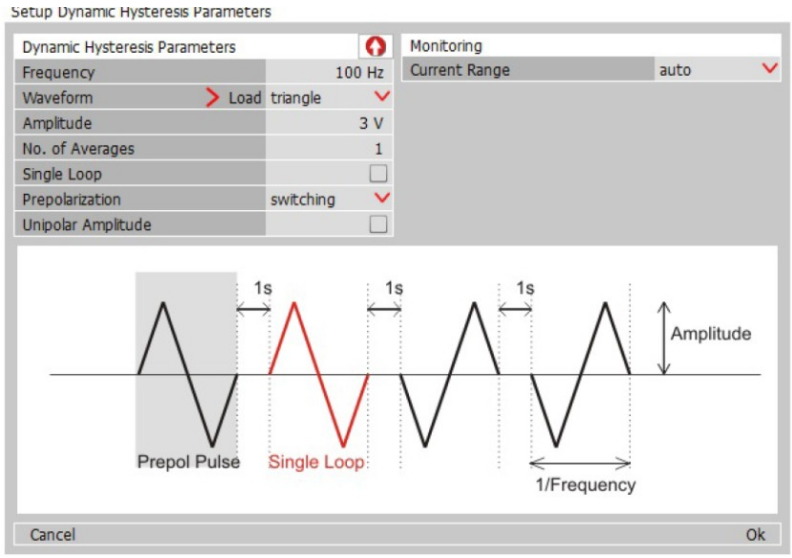

Figure II.21. The typical excitation signal of a DHM measurement preformed with the TFA system.

Each signal is followed by a relaxation time pause of 1 second. The prepolarization pulse and the second pulse of the excitation signal establish defined polarization states. The

prepolarization pulse has a negative state of relaxed remanent polarization. The second pulse ends in the positive state of relaxed remanent polarization. The corresponding hysteresis loop is an elaboration of the recorded charge signal for each step.

G.2 Home-made probes for direct and indirect magnetoelectric characterization

As far as the study of multiferroics proceed and new materials are discovered, the investigation of the electrical properties in multiferroic magnetoelectrics cannot be conceptually separated by that of the magnetic properties and vice versa. Nevertheless, nowadays, this aspect still represents an open challenge for the scientific community due to several theoretical and experimental problems which have already been introduced in the preceding chapters. Since the start of my activity, the main goal, on a par with the synthesis of new compounds and their characterization, was the development of instruments that can mutually:

- measure electric properties in a SQuID magnetometer,

- apply electric field in a SQuID magnetometer.

Such perspectives are very intriguing improvements because they may allow to measure how the material's electrical resistivity is affected by an external magnetic field (i.e. magnetoresistance)[†], how a dielectric constant varies as a function of an external magnetic field (i.e. magnetocapacitance) and how a pyroelectric measurement is conditioned by an external magnetic field (i.e. magnetoelectricity). In parallel the possibility to apply DC electric field in the SQuID magnetometer can in principle permit to characterize all the physical components of the magnetoelectric tensors, at least both the *E*-dependent and *H*-dependent part of the magnetic polarization:

$$M_i = \chi_{ij}^{m} H_j + \alpha_{ji} E_j. \qquad \text{(II.11)}$$

[†] The set-up for measuring electrical resistivity in the SQuID has been completely developed before my arrival

The α_{ji} terms in Eq. II.11 are the magnetoelectric linear coupling coefficients which measure the magnitude of the magnetoelectric effect.

Both these developments have been achieved and optimized leading to fully operative instrumental options for non-conventional magnetic/electric characterizations. Hereinafter a concise description of the three main probes will be presented.

G.2.1 SQuID probe for Capacitance Measurements

The probe, pictured in Fig. II.22, is thought to perform measurement of the electric permittivity (dielectric constant) as a function of temperature and frequency by means of the external Agilent 4284 Capacitance Bridge. The probe location within the SQuID cryostat allows to use directly the software of thermal control equipped with the magnetic apparatus. A homemade routine also permits to control the electrical parameters (e.g. the electrical field intensity and the frequency step at each temperature) before launching the complete measurement. The same routine allows to switch on and off the magnetic field at any time during the procedure.

Figure II.22. Ending part of the capacitance probe for dielectric characterization within the SQuID magnetometer.

The standard sample preparation requires a macroscopic sample of discoid shape, with face area A > 1 mm^2 and thickness $200\ \mu m < t < 2000\ \mu m$. For this characterization, the sample must be properly lapped and smoothed to guarantee a very low superficial roughness and prevent contact inhomogeneity with the planar capacitor, constituted by two metalized mica plates. These act as reference capacitor for the measurement, the sample capacitance is calculated by subtracting its contribution from the mica capacitance. The external structural materials and the cabling elements of this probe are non-magnetic materials to avoid spurious Faraday-Neumann induced currents during the application of a magnetic field.

G.2.2 SQuID probe for Pyroelectric Measurements

The pyroelectric probe (Fig. II.23) is the protagonist of the primary step towards the discovery of possible ferroelectric behavior in magnetic perovskites. The measurement consists in the recording of the produced current intensity during a thermal heating/cooling of the sample in a short-circuit condition. If the material is pyroelectric an electric voltage will be spontaneously generated, at a certain temperature, due to a structural or an electric polarization change occurs. As a consequence a current will cross the sample in order to compensate the voltage. This current is a leakage current and it is a typical marker of the ferroelectricity. This current is thus associated to *depolarization/relaxation processes*. In most cases the magnitude of such signal is very tiny, in the order of tens *pA*. Therefore a strict constraint concerns the sensitivity of the reading Electrometer. My Keithley 6517-B Electrometer fulfills these requirements at full.

Moreover, polarization or structural changes can be also extrinsically induced. For this reason, the whole system is equipped with a Keithley 2400 Sourcemeter which at any moment may apply a DC poling along the sample.

Figure II.23. The inner part of the probe devoted to pyroelectric measurements within the SQuID. The outer cylindrical screen, made of non-magnetic brass material, has not been included in the picture.

The sample preparation is a crucial point also for a pyroelectric measurement. Beside all the described manual re-shaping treatments performed for the dielectric measurement, in this instance the sample need to be properly metalized. I found out that a thin layer of Platinum, deposited by sputtering technique, is the most reliable metallization in terms of junction ohmicity. It has been verified that the layer thickness must be smaller than *25 nm*. At the same time, to avoid spurious contributions on the capacitor, such as border effects, the layer area ought to be smaller than the *85% ÷ 90%* of the total face area of the material under test. Finally, the measuring structure consists in a real planar plate capacitor in which the armatures are precisely those deposited layers of Pt while the dielectric is represented by the sample.

G.2.3 SQuID probe for Magnetoelectric Measurements

The last presented tester is the so called magnetoelectric probe (Fig. II.24). Differently to the above mentioned probes, with this setup I can actively exploit the SQuID also as magnetometer not just as cryostat, thus performing a real magnetic characterization. The introduced novelty consists in the addition of an extraordinary task: the possibility of

managing the magnitude of an DC electrical poling on the sample by means of a Keithley 617 Electrometer. As a whole I can perform as well as the conventional magnetic studies (i.e. Zero Field Cooling (ZFC), Field Cooled (FC) and M(H)), *M(E*) measurements at fixed temperatures and also *M(T)* after Electric Field Cooling (*EFC*) in absence or in presence of a magnetic field. Due to the complexity of these operations, the probe is designed for preventing unwanted and even dangerous effects. First of all, the electric components (e.g. wiring, cabling and contacting ones), in particular those surrounding the sample, are made of non-magnetic metallic alloys and shielded by insulating non-metallic covers.

Figure II.24. The insulated and screened magnetoelectric probe which houses the metalized sample. This asset allow to apply DC electrical poling up to 105 V.

All these attentions are mandatory, as far as the high sensitivity of the SQuID sensor to paramagnetic/diamagnetic contamination produced by all the electrical components is concerned. I verified that with these precautions the mass magnetic susceptibility measured using this probe differs from the one measured for the same sample with a standard SQuID probe by less than 5%.

In addition to avoid electrical bursts within the SQuID, I ought to operate in security conditions, determined essentially by the liquid Helium breakdown voltage (around 120 V). For what concerns the sample preparation, no modifications are necessary with respect to the pyroelectric case.

H. Recap of the Multiferroic Magnetoelectric characterization stages

In conclusion, this subchapter would represent a reference point which charts the course of the results and discussion part that is starting at the end of this chapter. Therefore I decide to recap all the experimental procedures, carried out every time a new material with possible multiferroic magnetoelectric behavior is synthesized by HP/HT techniques.

H.1 Characterization Guide

- Structural characterization (powder X-Ray diffraction, single-crystal diffraction)

The as-grown pellet is cut in two and for a half preserved while for the other half is ground and powdered. Singles crystals, if present, are taken apart. The collected information possibly allow to solve the spatial symmetry and refine the unitary cell.

- Standard magnetic characterization

Preliminary magnetic analyses are performed on fragments of the ground part. In this stage I usually understand if the sample is effectively magnetic, what type of magnetism is observed and if the thermal threshold of the magnetic order is sufficiently high to make the sample promising. Usually also the first magnetic hysteresis loops are measured.

- Neutron diffraction (and/or Synchrotron) analysis

If the sample is considered a good candidate, a proposal for a neutron investigation in international Facilities is done. Neutrons are perfect probes to gather information on the magnetic structure, moreover they give an important insight on the Oxygen positions in the cell, which is difficult to explore with X-ray based techniques.

- Sample preparation for electrical characterization

The preserved half part, usually a corrugated disc, is comprehensively lapped and smoothed in both the face areas reducing the roughness below few μm. Specifically, proper samples for electrical characterization must have face area A ≈ 4÷8 mm^2 and thickness t < 500 μm.

- Electrical resistivity and dielectric characterizations

This conventional characterization is usually carried out to understand the electric character. The sample, prepared as mentioned, is tested as function of temperature. If the sample displays high conductivity in the whole thermal range (low resistivity), it will be studied for verifying the possible occurrence of magnetoresistive behavior, while pyroelectric and ferroelectric test will be exclusively performed in the case of sufficiently high electrical resistivity.

- Sample preparation for pyroelectric and ferroelectric characterization

In the latter instance a new sample manipulation is required. The sample is also metalized by sputtering technique with a thin layer of Platinum on both faces.

- Pyroelectric and ferroelectric characterizations

The metalized sample is tested by means of the pyroelectric probe and at later stage with the TFA ferroelectric tester. This study, in best hypothesis, leads to the recording of the ferroelectric hysteresis loop, establishing so its multiferroic nature.

- Magnetoelectric characterization

As the conclusive stage, dielectric and pyroelectric measurements are re-performed by using the SQuID probes so that an external magnetic field of variable intensity can be

applied. In addition the sample is also tested using the magnetoelectric probe. The evidence of macroscopic variations of the electrical (magnetic) properties as a function of the applied magnetic (electric) field is the confirmation of indirect magnetoelectric effects. Moreover the eventual observation of M(E) hysteresis loop establish the occurrence of a direct magnetoelectric coupling. The first half of the magnetoelectric tensor coupling coefficients can in this case be calculated after the measure of three M(E) on a single crystalline sample oriented in all the three crystallographic directions. This is the most challenging point because of the difficulty in synthesizing sufficiently large single crystals by means of HP/HT techniques.

During this long series of operations, it often happens that some complications or non-clear physical phenomenologies arise. Such difficulties forces me a turn to other supplementary techniques or competences. In the last years, I have usually recurred to TEM analyses for trying to unveil subtle structural anomalies. In other situations I have investigated some very intricate magnetic features, subsidiary to multiferroism, exploiting local techniques as for example Mössbauer Spectroscopy and NMR. In particular the former gave a substantial push in the interpretation of spontaneous magnetization reversal observed in one of my perovskite (it will be thoroughly discussed in following chapter). Some of the still open issues are nowadays stimuli for theoretical and statistical physics studies. Many other minority contributions have also been required along the way (in the field of Raman spectroscopy, microanalysis, atomic force microscopy (AFM), magnetic force microscopy, etc.) and all these efforts slowly built a variegate and wide pattern of collaborations which, beside the fact that positive results are or not achieved, made my daily scientific research an exciting and enriching experience.

References

[1] J. C. Maxwell *Phil. Trans. R. Soc. Lond.* **155**, 459–512 (1865).

[2] W. C. Roentgen *Anna. Phys.* **354**, 264 (1888).

[3] P. Curie *J. de Phis. 3° sèrie vol. 3* **26**, 393 (1894).

[4] P. Z. Debye *Physik.* **30**, 300 (1926).

[5] L. D. Landau *Phy. Zs. Soviet.* **26**, 545 (1937).

[6] L. D. Landau, and E.M. Lifshitz *The Classical Theory of Fields* 2nd ed.: Pergamon, London, (1962).

[7] I. E. Dzyaloshinskii *Sov. Phys. JETP* **10**, 628-629 (1959).

[8] D. N. Astrov *Sov. Phys. JETP* **11**, 708-709 (1960).

[9] J. Wang et al. *Science* **299**, 1719-1722 (2003).

[10] T. Kimura et al. *Nature* **426**, 55-58 (2003).

[11] N. Hur et al. *Nature* **429**, 392-395 (2004).

[12] H. Schmid *Ferroelectrics* **162**, 317–338 (1994).

[13] D. V. Efremov, J. van den Brink, and D. Khomskii *Nat. Mater.* **3**, 853 (2004).

[14] M. Fiebig *J. Phys. D: Appl. Phys.* **38**, R123 (2005).

[15] N. A. Spaldin, M. Fiebig *Science* **309** (5733), 391-392 (2005).

[16] S. W. Cheong, and M. A. Mostovoy *Nat. Mater.* **6**, 13-20 (2007).

[17] J. van den Brick, and D. Khomskii *arXiv:0803.2964v3 [cond-mat.mtrl-sci]* (2008).

[18] D. Khomskii *Physics* **2**, 20 (2009).

[19] H. Zheng et al. *Science* **303** (5658), 661-663 (2004).

[20] A. V. Shubnikov *Symmetry and Antisymmetry of Finite Figures.* USSR Academy of Sciences (1951).

[21] B. B. Van Aken et al. *Nat. Mater.* **3**, 164-170 (2004).

[22] F. Mezzadri et al., *Phys. Rev. B* **78**, 064111, (2008).

[23] J. Neaton et al. *Phys. Rev. B* **71**, 014113 (2005).

[24] R. Seshadri et al. *Chem. Mater*. **13**, 2892–2899 (2001).

[25] A. Moreira dos Santos et al. *Appl. Phys. Lett.* **84**, 91-93 (2004).

[26] D. J. Singh et al. *Phys. Rev. B* **73**, 094102 (2006).

[27] F. Mezzadri et al. *Phys. Rev. B* **79**, 100106(R) (2009)

[28] N. Ikeda et al. *J. Phys. Soc. Japan.* **69**, 1526 (2000).

[29] D. V. Efremov et al. *arXiv:cond-mat/0306651 [cond-mat.str-el]* (2003).

[30] C. Zener *Phys. Rev.* **82**, 403-405 (1951).

[31] Y. Miyamoto *J. Phys. Soc. Jap.* **57**, 2040 (1988).

[32] E. J. W. Verwey *Nature* **144**, 327 (1939).

[33] I. A. Sergienko, and E. Dagotto E. *Phys. Rev. B* **73**, 094434 (2006).

[34] M. A. Mostovoy *Phys. Rev. Lett.* **96**, 067601 (2006).

[35] G. Lawes et al. *Phys. Rev. Lett.* **93**, 247201 (2004).

[36] K. Taniguchi et al. *Phys. Rev. Lett.* **97**, 097203 (2006).

[37] C. Ederer, and N. A. Spaldin *Phys. Rev. B* **74**, 020401(R) (2006).

[38] S. Nandi et al. *Phys. Rev. B* **78**, 075118 (2008)

[39] S. Picozzi et al. *Phys Rev. Lett.* **99**, 227201 (2007).

[40] V. M. Goldschmidt *Die Naturwissenschaften* **21**, 477-485 (1926).

[41] A. Prodi et al. *Nature Mater.* **3**, 48 (2004).

[42] N. J. Perks et al. *Nature Comm.* **3,** *1227* (2012).

[43] A. Prodi *Phys. Rev. B* **79**, 085105 (2009).

[44] D. Walker *Americ. Mineral.* **76**, 1092-1100 (1991).

[45] http://www.aixacct.com/pdfs/tf2000.pdf

III. Experimental Results and Discussion

In writing the central chapter concerning the presentation and the discussion of the achieved experimental results, the model I chose is not a simple sum of my scientific activities but rather a logical and chronological path towards the complete characterization of novel multiferroic magnetoelectric materials. As anticipated, the materials I have studied belong to the Pb and Bi-based double perovskite family. For such a family the mechanism responsible for ferroelectricity is the lone pair stereochemical effect described in section *II.D.2*. Despite the electrical order, the presence of different magnetic ions on the B-site helps in promoting magnetism through an independent way. My bet was to obtain phases with high temperature magnetic order, around or even above the significant threshold of room temperature. At the same time I aimed to achieve an additional lowering of spatial symmetry by means of a complex scheme of fundamental interactions, like the superexchange interactions, the Jahn-Teller effect and anisotropic second order effects, as for instance SIA or DM. Indeed, the necessary condition to interconnect these two independent ferroic orders (i.e. magnetoelectricity) may be satisfied precisely thanks to the action of these mechanisms. However, the superposition of such concomitant effects is often reflected in the increase of physical complexity, which slows down and complicates the understanding of structural, the electrical and magnetic properties.

In the following, all the synthesized materials will be briefly presented; whereas the discussion will just concern two of them, Bi_2FeMnO_6 and Pb_2FeMoO_6, which play the preeminent role in my research activity. Especially, the complementary physical properties they showed allow me to give the reader a wide overview about the potentialities of the exploited characterization techniques (widely described in subchapter *II.G*)

In addition, some findings, subsidiary to magnetoelectricity, have revealed some very interesting and unveiled characters, imposing supplementary scientific efforts. For this reason this chapter will take charge of these aspects too.

Finally, the last two subchapters will be dedicated to the two main external cooperation in which I was successfully involved during the last three years. Since the obtained results

brought to good outcomes, a specific treatise is unavoidable. Moreover these contributions need a self-standing introduction since they refer to scientific topics different from that of multiferroic magnetoelectrics.

A. The reasons of interest about Double Perovskite systems

The term double perovskite, as anticipated in the subchapter *II.E*, is the name given to those materials displaying a formula unit twice that of simple perovskite ABO_3. Basically, double perovskite retains the same coordination numbers for A and B positions; the sole difference is represented by the presence of two distinct B ions in an ordered ($A_2BB'O_6$) or disordered ($A(B,B')O_3$) arrangement.

These compounds are strongly correlated systems, used as sensors and catalyst electrodes in certain types of fuel cells and are candidates for memory devices and other spintronics applications. Many superconducting ceramic materials (the high temperature superconductors) have double perovskite-like structures, often with three or more metals including copper, and some oxygen positions left vacant. One prime example is yttrium barium copper oxide (YBCO), which can be insulator or superconductor depending on the oxygen content. Also some strontium-based ruthenates (e.g. $SrRuO_4$ [1]) are copper-free superconducting double perovskites.

Nowadays many other examples can be found even in the class of multifunctional materials. The first studied compounds of this class are the strontium-based magnetic double perovskites. In particular, some members of the family, i.e. Sr_2CrMoO_6 and Sr_2FeReO_6, are ferromagnetic, while Sr_2FeWO_6, Sr_2MnMoO_6 and Sr_2CoMoO_6 are antiferromagnetic [2,3,4,5]; however almost all show very high Curie or Néel transition temperatures. Indubitably, the most significant compound between them is Sr_2FeMoO_6 [6], which crystallizes in the canonical double perovskite tetragonal unit cell with lattice parameters $a = b = 5.57\ Å \approx \sqrt{2}a_p$, and $c = 7.9\ Å \approx 2a_p$ and space group *I4/mmm* (Fig. III.1). The detected long range alternation between Fe^{2+} (d^6) and Mo^{6+} (d^0) determines a predominant superexchange interaction Fe-O-Fe mediated by Mo.

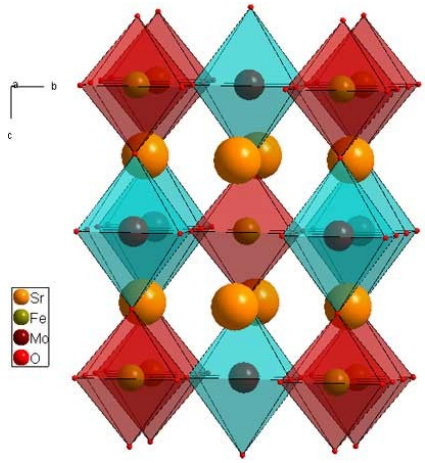

Figure III.1. Unitary cell of Sr_2FeMoO_6 double perovskite. *[image taken from Ref. 5]*.

As a result, Sr_2FeMoO_6 behaves as a semi-metal with a huge ferromagnetic character (as predicted also by *Goodenough-Kanamori semi-empirical rule* [7,8]) below $T_C = 415\ K$ and also a colossal magnetoresistance (CMR). In line with the discussion introduced in subchapter *II.C*, this class of double perovskites seems to perfectly fit the postulated link between ferromagnetism -semi-metallic behavior- magnetoresistance. Coherently, antiferromagnetic Sr-based perovskites are characterized by a more pronounced semiconducting, if not insulating, character and they prefigure the possibility of coexistence of magnetism and ferroelectricity (multiferroism).

Nevertheless, such ordered double perovskites have unfortunately a centrosymmetric structure with no-geometrical frustration, while the high density of unpaired electrons easily promotes free carrier in the conduction band. As far as Fig. III.1 is concerned, the observed lack of tilt and rotation phenomena of the BO_6 octahedra confirmed the invariance for spatial inversion symmetry transformation, excluding de facto a ferroelectric behavior. A possible solution goes through a chemical action on this structure, exploiting the extraordinary tolerance of the perovskite cell (subchapter *II.E*).

B. My proposal: Pb and Bi-based Double Perovskites

The knowledge about those intrinsic setbacks affecting the magnetic Sr-based double perovskites and avoiding the occurrence of multiferroism, push me to blaze a trail seeking a possible "electric solution". The insulating/polar character of the structure can be achieved by means of proper chemical substitutions.

By reasoning on the chemical formula, I chased the ferroelectricity in two different ways.

Pb-based double perovksites

A possible approach is the substitution of Sr^{2+} with the lone pair active Pb^{2+}. This allows to use ions on the B-site belonging to distinct periods and having different oxidation state, as for instance by introducing an ion of the III period (Cr, Mn, Fe, Co, Cu) together with an ion of the IV-V period (Mo, W, Re). In this configuration a cation-ordered distribution on the B-site is favored, due to the significant charges and ionic radius differences. In most cases, however, the eventual structural distortion induced by the lone pair effect of Pb^{2+} is certainly negligible with respect to the main contribution given by the large number of free carriers usually promoted by the ions on the B-sites.

Bi-based double perovskites

Alternatively, I operated substitutions on the B-site, by a modification of the oxidation state on the A-site switching from a divalent to a trivalent stereochemically active ion: Bi^{3+}. This strategy needs to be accompanied by a lowering of the total oxidation state on the B site, typically by means of the introduction of two III period elements. Therefore, contrarily from the first case, the ionic radius and the valence of the B-site cations are similar so that a disordered distribution is promoted. Anyhow the stereochemical effect produced by Bi^{3+} is theoretically higher than that induced by Pb^{2+}. At the same time the ionic radius of Bi^{3+} is smaller than that of Pb^{2+} (*155 pm* vs *175 pm*): this means that the Bi^{3+} perovskite should tilt and rotate the octahedra around the A-site for compensating its lower space occupancy. This mechanism causes a lowering of the structural symmetry and enforces the chance to get polar character in the system; moreover it enhances the gap between valence and conducting band. It is worthy to note that the majority of these operations can just be realized in high-

pressure / high-temperature conditions to satisfy the structural requirements pointed out in this subchapter and, as a whole, also in subchapter *II.F*.

Following the two described chemical solutions, I performed several HP/HT syntheses of bulk Pb and Bi-based double perovskites varying different compositions thermodynamic parameters *(P,T),* reaction times and also the stoichiometric ratio of the precursors. I remark that this kind of syntheses are solid-state reactions of the constituent binary oxides powder mixtures. The quality and purity of each reactant together with the care in the precursors preparation are fundamental aspects of this delicate process. More than one attempt was necessary to find out the better conditions and the high purity for each synthesis product. Hereinafter, I decide to restrict to the sole samples who were obtained with purity larger than 90%, skipping all the subsidiary information about further collateral operations performed to reach the final result.

C. Bi_2FeMnO_6 (BFMO), a HP/HT Bi-Based Double Perovskite

Bi-based double perovskites represented the most studied systems of my doctorate and, more, the interest in this class already came out during my Bachelor's traineeship, in 2010. The ultimate goal of this work was to try to overtake the extraordinary multiferroic properties obtained by $BiFeO_3$ (BFO) and $BiMnO_3$ (BMO). The former, introduced in subchapter *II.A* (Ref. II.[23]), is the most important multiferroic compound, which exhibits a (canted) antiferromagnetic transition below $T_N = 643\ K$ and a para-to-ferroelectric transition below $T_E \approx 1100\ K$. The latter, (Ref. II.[24,25]), revealed a different kind of multiferroism with a debated ferromagnetic transition below $T_C = 105\ K$ and ferroelectricity below $T_E \approx 720\ K \div 750\ K$ [9], which seems to depend both on morphology and stoichiometry [10]. Despite the compositional similarities, the effects of Fe^{3+} (d^5, isotropic electronic structure) and Mn^{3+} (d^4 and Jahn-Teller active) ions on the B-site result in completely different spatial and magnetic symmetries. BFO, in film or bulk ceramic form, crystallizes in a rhombohedral off-centered cell (space group *R3c*) while BMO owns a low monoclinic polar symmetry (space group C2). By analogy, if bulk BFO is synthesizable through standard techniques, bulk BMO needs high pressure environments. However, both compounds are characterized by some drawbacks dealing principally with the high electric leakage.

In the later 2010, I started to mix together BFO e BMO with the aim of creating an intermediate phase of these two compounds, supported by the conviction that a fusion of their properties could have leaded to a greater tendency for the multiferroic magnetoelectric behavior. In February 2011 I successfully synthesized Bi_2FeMnO_6 (BFMO), the first potentially multiferroic system ever produced in our laboratory. Since that moment until mid 2012, I succeeded to produce other Bi-based double perovskites by substituting distinct III period magnetic elements instead of manganese (a) Bi_2FeCrO_6 and instead of iron (b) Bi_2MnCrO_6, Bi_2CoMnO_6 and Bi_2CuMnO_6.

The experimental synthesis conditions together with a collection of their basic structural and magnetic properties are gathered below in Table III.1.

Table III.1. List of the Bi-based double perovskites synthesized during my Ph.D activity together with their structural and magnetic characteristics.

Bi-based double perovskite	***P (GPa)***	***T (°C)***	***time (h)***	***Structure***	***SG***	***type of magnetism***
Bi_2FeCrO_6	*4*	*1000*	*1*	Monoclinic	*Cm*	Spin glass-like
Bi_2FeMnO_6	*6*	*1100*	*1,5*	Orthorhombic	*Pnam*	AFM (T_N = 288 K)
Bi_2MnCrO_6	*5*	*900*	*1,5*	Monoclinic	*C2/c*	AFM (T_N = 22 K)
Bi_2CuMnO_6	*6*	*1000*	*1*	Monoclinic	*C2*	FM (T_C = 323 K)
Bi2CoMnO6	*6*	*1100*	*1*	Orthorhombic	*Ibam*	Canted-AFM ((T_N = 150 K)

As mentioned in the recap of Chapter *II*, a complete and comprehensive preliminary characterization were always performed for each new material. Preliminary PXRD and magnetometric measurements were carried out for all the these compounds. However, due to the extraordinary, exotic and intriguing properties shown by BFMO, my work during the period of my Ph.D Thesis was prevalently devoted to it. As a consequence, I chose to limit the following experimental report (and the connected scientific discussion) to a comprehensive description of this compound.

C.1 Synthesis of BFMO

BFMO was successfully obtained at 6 GPa and 1100 °C after 1.5 h of reaction; then the system was abruptly quenched to room temperature before the pressure was slowly released [11]. The samples form is prevalently polycrystalline, characterized by a single crystal mean dimension of lower than $50\ \mu m \div 100\ \mu m$. The mean sample purity, in these thermodynamic conditions, is around 95%, with the sole contamination of the diamagnetic compound Bi_2CO_5, as will be explained in the next section.

Preliminary single crystal XRD experiments were performed on different samples and confirmed the results obtained also in a previous work [12]. In all the cases, most of the observed reflections could be indexed on the basis of an orthorhombic double perovskite superstructure with $a = 5.5728 \approx a_{dp} \approx \sqrt{2}a_{sp}$, $b = 11.2065 \approx 2a_{dp} \approx 2\sqrt{2}a_{sp}$ *and* $c = 15.7430$

$\mathring{A} \approx 2a_{dp} \approx 4a_{sp}$, 16 times in volume with respect to the fundamental cubic perovskitic cell with lattice parameter a_p and 4 times the double perovskitic theoretical cell. This agrees with the results of powder XRD, where, besides the reflections indicating the presence of the sole extra phase of Bi_2CO_5, no extra peaks were observed by indexing the pattern with the orthorhombic cell.

C.2 Space and time-structure of BFMO

C.2.1 Spatial symmetry (Electricity)

A definitive confirmation of the structure symmetry was offered by transmission electron microscopy (TEM) experiments, indicating the orthorhombic lattice as the true cell of the structure. Selected area electron diffraction (SAED) patterns, taken along the fundamental [001] and [010] crystallographic axes of the orthorhombic cell, are shown in Fig. III.1 (left-side). The existence of a short-scale twinning, involving the exchange of the fundamental perovskite axes (quite similar by the metrical point of view), was clearly evidenced by high resolution electron microscopy (HREM) coupled with SAED, reported in Fig. III.2 (right-side). Despite the large number of examined crystals having suitable dimensions, a more or less notable twinning affection was detected in any case.

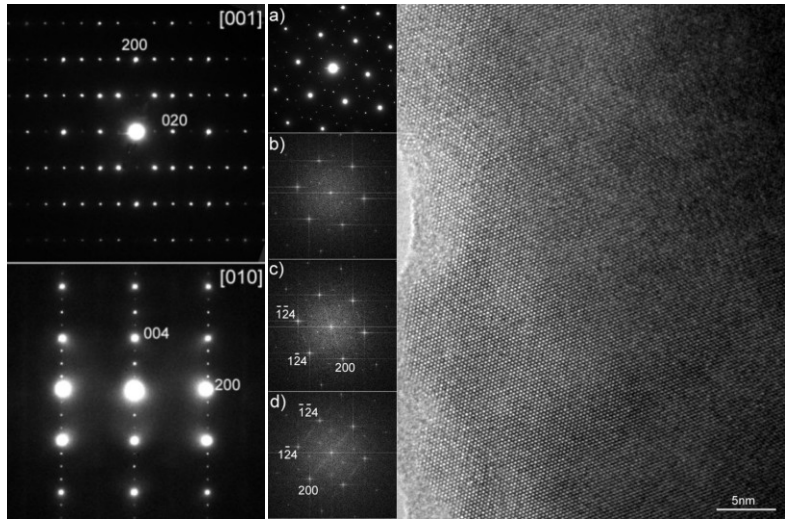

Figure III.2. On the left side, SAED patterns taken on single domain regions of BFMO samples. On the right side, HREM image taken in a [111] projection of the fundamental perovskite structure showing the presence of twinning domains involving a 60° rotation of the orthorhombic superstructure lattice around the zone axis. The corresponding experimental SAED pattern is shown in inset a), compared with the FFT obtained on the whole sample as well as on the upper and lower regions of the image reported in the insets b), c) and d), respectively; c) and d) patterns are indexed on the basis of the orthorhombic superstructure. *[image taken from Ref. 11].*

The structure was solved using SIR2004 [13] in the centrosymmetric *Pnam* space group and refined with SHELX97 [14]. The transition metal sites, TM1 and TM2, were refined by constraining the occupancy of both Mn and Fe to 50%, in agreement with the observed equivalence of their average bond distances. Rietveld refinement of the powder diffraction data, produced by using the structural parameters determined by single crystal XRD, confirmed these results. Crystal data and refined parameters are reported in Table III.2. In parallel, the cation-oxygen bond lengths evidenced large distortions of the coordination around the bismuth atoms, induced by the strong stereochemical activity of the $6s^2$ lone pair. Noteworthy, this effect involves also the iron/manganese coordination octahedra, which appear to be largely distorted. In spite of this, the two TM sites show, as previously pointed out, the same average bond distance confirming the absence of cation ordering. Because of disorder on the B-site, it is more correct to treat the compound as a real solid solution of BFO and BMO imposing hereafter the proper chemical formula formalism of $BiFe_{0.5}Mn_{0.5}O_3$.

Table III.2. Crystal data and refined parameters. *[table taken from Ref. 11].*

Space group	*Pnam*	Reflections collected	16500
Unit cell dimensions	a = 5.5728(5) Å	Data/restraints/parameters	1356/0 /97
	b = 11.2065(10) Å	Goodness-of-fit on F^2	1.249
	c = 15.7430(15) Å	R indices [I>4σ(I)]	R_1 = 0.0561, wR_2 = 0.1291
Volume	983.175 (3) $Å^3$	R indices (all data)	R_1 = 0.0641, wR_2 = 0.1249

	X	Y	Z	s.o.f	$U_{eq}(Å^2)$
Bi1	0.27114(17)	0.13754(8)	¾	1	0.0105(2)
Bi2	0.71523(18)	-0.12525(8)	¾	1	0.0107(2)
Bi3	0.72410(16)	-0.12533(6)	0.51022(5)	1	0.0189(2)
TM1*	0.7429(4)	0.12118(19)	0.62580(14)	1	0.0082(5)

TM2*	0.74827(4)	-0.37683(19)	0.62344(14)	1	0.0055(5)
O1	0.680(3)	0.0769(18)	¾	1	0.0144(4)
O2	0.578(2)	-0.2236(11)	0.6307(8)	1	0.013(3)
O3	0.723(4)	0.1638(16)	0.5057(9)	1	0.035(4)
O4	-0.032(2)	0.2473(11)	0.8433(8)	1	0.010(2)
O5	0.484(3)	0.0052(14)	0.5977(9)	1	0.021(3)
O6	0.971(3)	-0.0198(15)	0.6134(10)	1	0.025(4)
O7	0.815(4)	-0.3877(19)	¾	1	0.020(4)

*site occupancy factors of both Mn and Fe (TM1 and TM2) fixed to 0.50

Furthermore the analysis of the TM-O distances in terms of charge distribution performed using the program CHARDIS99 [15], suggested the exclusive presence of Fe^{3+} and Mn^{3+} within the structure. A representation of the crystal structure projected along the [001] and [100] directions is reported in Fig. III.3. The large superstructure observed in $BiFe_{0.5}Mn_{0.5}O_3$ is quite unusual, as most of the known orthorhombic double perovskites display a crystallographic cell with $a \approx b \approx \sqrt{2}a_p$, $c \approx 2a_p$ related to the tilt of the BO_6 octahedra. The large periodicity is ascribed to the distortions produced by the bismuth atoms, inducing a complex structure in which the TMO_6 octahedra are both tilted along the *c* direction (with TM-O-TM bond angles ranging from *157.6°* to *146.2°*) and rotated in the *ab* plane with a + + – – scheme [16] along c. Noteworthy the displacement scheme of the bismuth ions involves the formation of dimers that are consistent with an antiferroelectric structure, as shown in Fig. III.4.

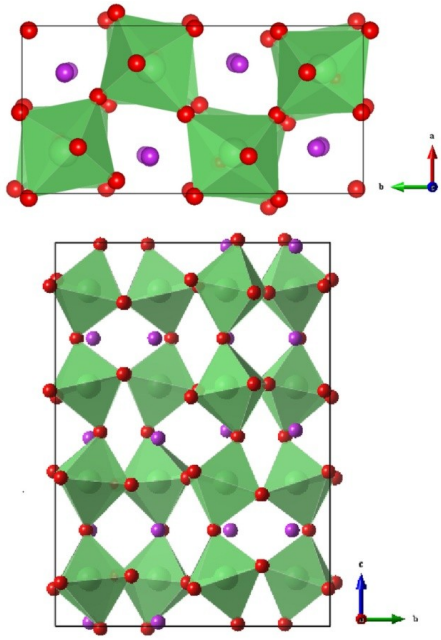

Figure III.3. BFMO crystal structure projected on the *ab* (top) and *bc* (bottom) planes made using the program VESTA [*17*]. The vertex-sharing light-green octahedra are linked by the red oxygen atoms, while the purple spheres represent the bismuth ions. *[image taken from Ref. 11].*

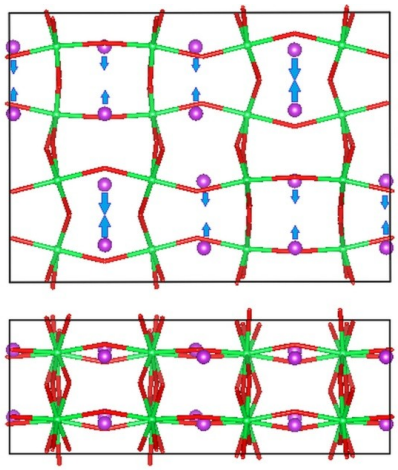

Figure III.4. Relative shifts of the bismuth ions in the crystal structure of BFMO projected on the *bc* (top) and *ac* (bottom) plane. *[image taken from Ref. 11].*

Surprisingly, if one considers the dramatically different structures of the two end members of the $BiFe_{1-x}Mn_xO_3$ solid solution, the structure observed here is very close to the one reported for $BiFe_{0.75}Mn_{0.25}O_3$ [18], in particular for what concerns the scheme of both octahedral distortions and bismuth ions shifts. Within this framework, the observation of similar physical properties in $BiFe_{0.5}Mn_{0.5}O_3$ and $BiFe_{0.75}Mn_{0.25}O_3$ suggests a strong structure-properties relation in this family of compounds. High-resolution neutron diffraction data were collected at 10 K, 310 K and 500 K allowing a thorough refinement of the structural features of the system which points out the absence of symmetry changes in the entire investigated temperature range. In analogy to XRD analyses, two phases, namely $BiFe_{0.5}Mn_{0.5}O_3$ and Bi_2CO_5 in a 20:1 ratio, were necessary to index the patterns. Rietveld plots of the refinements performed at 500 K and 10 K are reported in Fig. III.5.

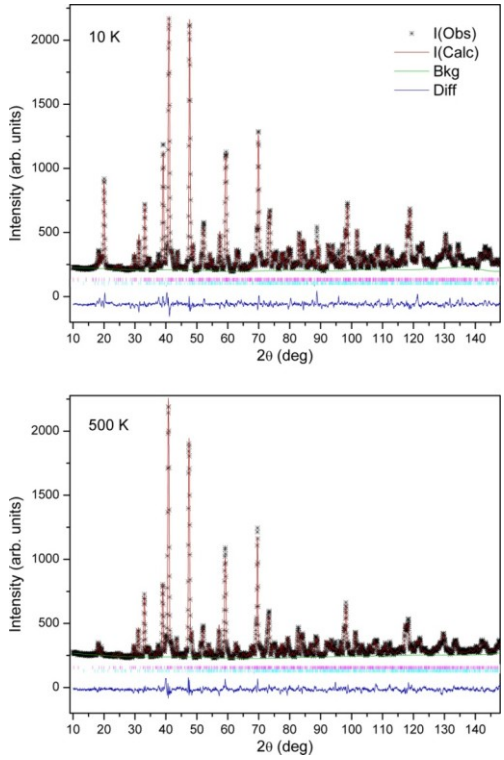

Figure III.5. Rietveld refinements of the neutron diffraction patterns collected at 500 and 10 K (top and bottom respectively). *[image taken from Ref. 11].*

C.2.2 Time symmetry (Magnetism)

Thanks to the neutron diffraction high-resolution data, collected at 500 K, it was possible to study the sample in the paramagnetic phase, confirming the goodness of the previously proposed space-structural model. In particular, due to the difference in atomic scattering factors of the iron and manganese ions in neutron diffraction, it was possible to exclude the presence of B-site cation ordering. The 10 K data show the raising of purely magnetic peaks with $k = (0,0,0)$ propagation vector related to antiferromagnetic G-type magnetic ordering of the B-site transition metals. The spin arrangement is shown in Fig. III.6 and involves collinear atomic moments along the *a* direction, with zero component along *b* and *c*, and the presence of isotropic first neighborhood antiferromagnetic interactions along the *c* direction. This evidence preliminarily excludes the presence of spin canting phenomena, in contrast to what proposed by Mandal et al. in Ref. 12. The observed atomic moment is $5.1\ \mu_B$, slightly higher than that expected ($4.5\ \mu_B$) for an averaged structure containing high-spin Fe^{3+} and Mn^{3+} ions. This is in any case the indicator of a magnetic structure at 10 K, which is long-range ordered and clearly shows the absence of inhomogeneities involving the magnetic structure and sizeable spin fluctuations, at least on the dimensional scale of neutrons sensitivity.

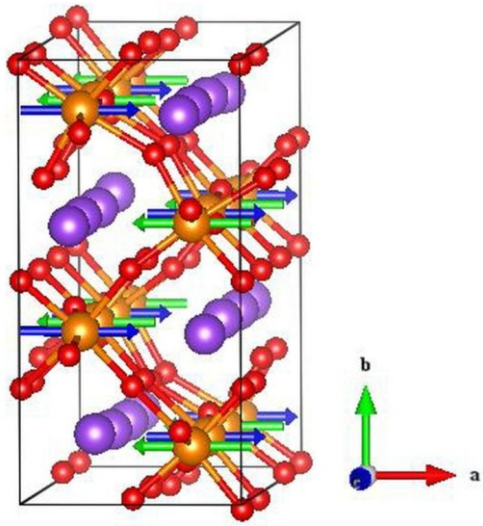

Figure III.6. Magnetic structure of $BiFe_{0.5}Mn_{0.5}O_3$: in orange are represented the transition metal ions, in purple the bismuth ones, and in red oxygen. The blue and green arrows indicate the antiferromagnetic atomic moments. *[image taken from Ref. 11].*

The high-flux data collected between 10 K and 500 K allowed the accurate study of the magnetic structure thermal evolution. No spin reorientations as well as changes in the propagation vector were observed in the entire examined temperature range. Fig. III.7 reports the refined atomic moment as a function of temperature, showing a Brillouin-like behavior up to about 290 K and suggesting the loss of long-range magnetic correlation to be located around this temperature. However, a weak and broad signal, observed in the 2θ regions where the magnetic reflections are detected, persists up to about 400 K, indicating the presence of mesoscopic magnetic structures of the TM ions with dimensions at the limit of neutron coherence length threshold. A similar behavior, as well as a G-type spin structure, was previously observed in $YFe_{1-x}Mn_xO_3$, being ascribed by the authors to the short-range magnetic ordering [19]

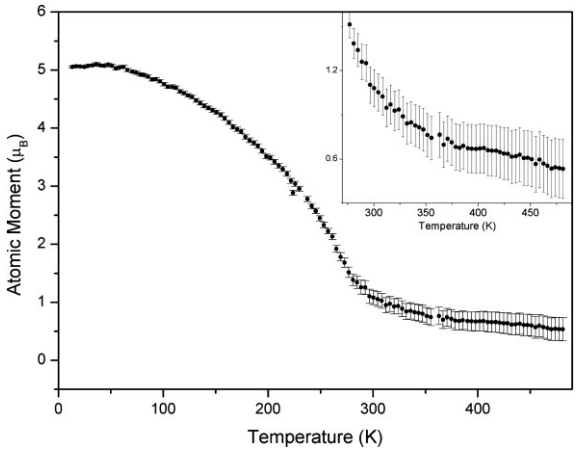

Figure III.7. Refined atomic moment in the 10 K ÷ 500 K range. The inset shows the 280 K ÷ 450 K region, where mesoscopic range magnetic interactions are detected. *[image taken from Ref. 11].*

The thermal evolution of the lattice parameters, reported in Fig. III.8, shows an appreciable anisotropic behavior. Differently from *a*, that shows a linear behavior at high temperatures, both the *b* and *c* parameters display anomalies at 288 K, corresponding to the long-range antiferromagnetic Néel temperature. These anomalies consist in opposite sign slope variations, slight for *b* but noticeable for *c*, suggesting the presence of spin-lattice coupling, which could be indicative of magnetoelectric effects. Moreover, as the temperature is decreased, the linear contraction of the *a* and *b* axes is arrested at about 100 K, while the slope of the *c* thermal evolution restart to increase. This may be associated with a structural change but, at this stage, the origin is unclear.

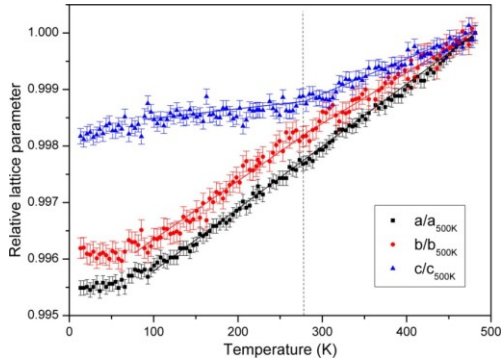

Figure III.8. Lattice parameters variation as a function of temperature. Solid lines are guides to the reader's eye. The dashed vertical line indicates the long-range magnetic ordering temperature. *[image taken from Ref. 11].*

C.2.3 Recap about BFMO structural properties

BFMO crystallizes in an unusual superstructure based on the double perovskite unit cell and with centrosymmetric space group *Pnam*. The stereochemical effect of Bi^{3+} ions causes a high tilt and distortion of the octahedra of coordination, leading to an antiferroelectric character of the structure. Disorder is detected on the perovskite B-site involving the iso-radius ions Fe^{3+} and Mn^{3+} implying a inhomogeneous distribution and coexistence of three different magnetic interactions: Fe-O-Fe, Mn-O-Mn, Fe-O-Mn.

Despite the spatial complexity, at first sight the magnetic structure is rather simple. A G-Type AFM structure is detected from 5 K to the Néel Temperature 288 K. The propagation vector $k = (0,0,0)$ allows to exclude magnetic cycloids and canting of the antiferromagnetism. Nevertheless, some weaker (ferro)magnetic phenomena survive in the paramagnetic phase of the compound suggesting the possible existence of mesoscopic structures (clusters) that yield a spontaneous magnetic moment up to 420 K ÷ 450 K.

Finally, the thermal evolution of the lattice parameters points out a possible spin-lattice coupling affecting the *c* axis when the AFM transition occurs. Spin-lattice effect may prefigure the occurrence of magnetoelectricity. Structural changes are detected also at about 100 K.

C.3 BFMO: Magnetometric characterization

C.3.1 Thermal Magnetization

Field cooling (FC) magnetometry was performed between 5 K and 680 K with applied field H = 100 Oe on an as-grown pellet.

The measurements, recorded both on cooling and warming, are reported in Fig. III.9.

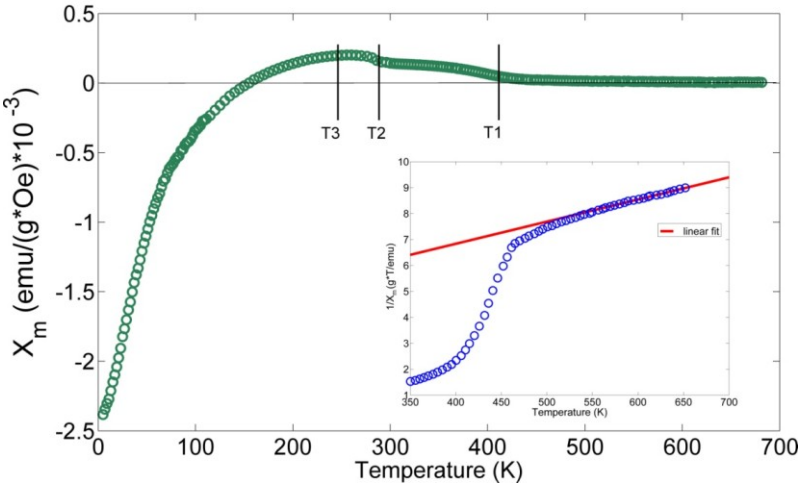

Figure III.9. Magnetic susceptibility of $BiFe_{0.5}Mn_{0.5}O_3$ bulk sample measured during a field cooling (FC) between 5 K and 680 K. In the inset the Curie fit of the paramagnetic region. *[image taken from Ref.11].*

In spite of its clear magnetic structure, BFMO seems not to behave as a common anitferromagnet. Its magnetic susceptibility as a function on temperature displays a quite unusual behavior. The sample shows a primary paramagnetic-to-weak ferromagnetic transition at T_1 = 420 K followed at lower temperature by two interconnected phenomena taking place at $T_2 = T_N$ = 288 K and T_3 = 250 K. This complex mechanism finally leads to a spontaneous magnetization reversal (MRV), whose specific treatise is postponed to subchapter *III.D* (a new interpretation of MRV has been recently proposed by our group [11] and independently by A.A. Belik [20] as a disorder-related phenomenon).

In parallel, high temperature measurements aimed to the study of the paramagnetic region of the compound were performed with applied field H = 10 kOe, due to the weak magnetic signal of the sample for such temperatures and are reported in the inset of Fig. III.9. The fitting of inverse susceptibility linear region (above T_1) allowed to determine the Curie-Weiss temperature $\theta = -400\ K$, confirming the overall antiferromagnetic nature of the interactions, and a number of Bohr magnetons of $5.4\ \mu_B/F.U.$. This value is consistent if compared to the expected value $5.2\ \mu_B$ for high-spin Fe^{3+} ($5.9\ \mu_B$) and Mn^{3+} ($4.9\ \mu_B$) in the case of an equiatomic solid solution. The observed weak ferromagnetic signal between T_1 and T_2 that was detected also with the neutron high-resolution characterization can be possibly ascribed to a second-order mechanism tailored on the long-range antiferromagnetic order and probably related to the disorder and inhomogeneity of the B-site ions. Just below room temperature, the low-field susceptibility undergoes a two-step transition (see Fig. III.9): at T_2 the antiferromagnetic long range order takes place determining an initial increasing of the magnetic susceptibility followed by a maximum reached at T_3; consequently the susceptibility starts decreasing up to a compensation ($\chi = 0$) and finally to a remarkable negative response as the system is cooled. On the contrary, high-field measurements do not show the same mechanism of compensation and the singular temperature T_3 disappears, as shown in Fig. III.10. The interactions responsible for MRV turn out to be completely overwhelmed by the effect of the applied field, and the displayed behavior below T_2 is characteristic of a compensated antiferromagnetic system [21] in high-field conditions. Thus, the weak ferromagnetism observed in $BiFe_{0.5}Mn_{0.5}O_3$, which is possibly related to the intrinsic disordered nature of the transition metals at the perovskite B-site, should be correctly considered as a perturbation superimposed to an overall antiferromagnetic behavior.

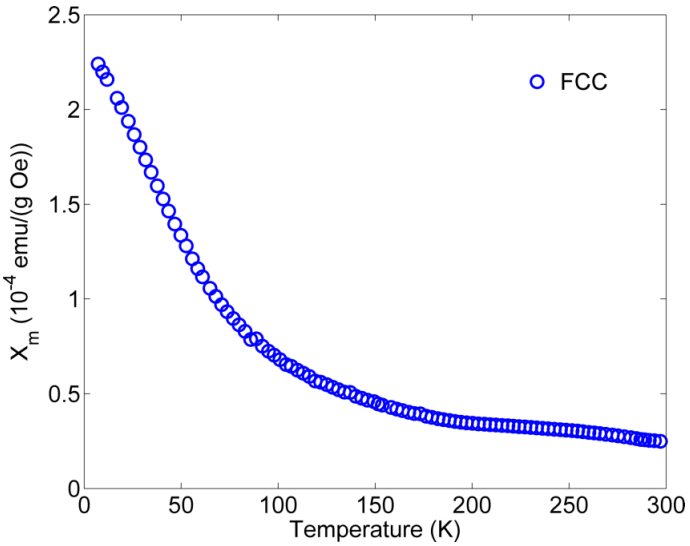

Figure III.10. FC magnetic susceptibility at 10 kOe, measured in cooling as a function of temperature, for a bulk sample of BFMO. *[image taken from sup. Mat. Ref. 11].*

C.3.2 Isothermal magnetization

Figure III.11 reports a series of isothermal magnetization measurements collected at different temperatures between RT and 500 K [22]. Above T_1 = 420 K, the system confirms to be in a paramagnetic state, in agreement with neutron diffraction and thermal magnetometric measurements discussed above.

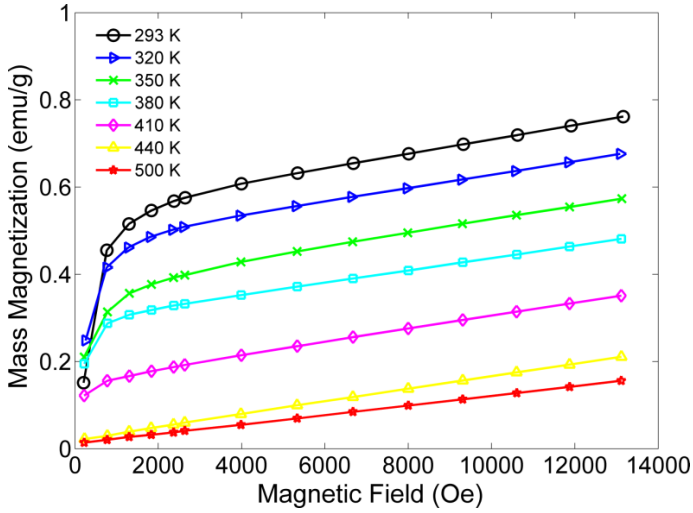

Figure III.11. Set of first magnetization isotherms collected at different temperatures above and below the ordering transition temperature T_1 = 420 K. *[image taken from Ref. 22].*

Below T_1, the isotherms show an increasing initial susceptibility for decreasing temperatures, followed by an antiferromagnetic linear trend for fields higher than about 2 kOe. Below RT the behavior of isothermal magnetization becomes more intricate, and a detailed analysis with a denser number of data is needed.

Figure III.12 reports the measurement of the initial magnetization at 5 K (where all the coexistent magnetic interactions are completely settled) for a BFMO bulk sample after a cooling in zero-field conditions. By decreasing temperature, as expected from Fig. III.10, a magnetization reversal spontaneously occurs, so the measurement starts inevitably from a negative value. The measurement was collected increasing the magnitude of magnetic field from 0 to 13 kOe. Two distinct changes in the slope can be clearly indentified. These two notable points, corresponding to the field values $H_1 \approx 650$ Oe and $H_2 \approx 2.2$ kOe are singular fields of the system, expressions of two different weak ferromagnetic contributions characterized by different value of the coercive field, that is, of a "soft" and a "hard" character (see also hysteresis loops of Fig. III.13 in the following section). The annulment of negative magnetization happens just for higher fields, at about 2.6 kOe for this sample (however this field changes from sample to sample depending on its synthesis history).

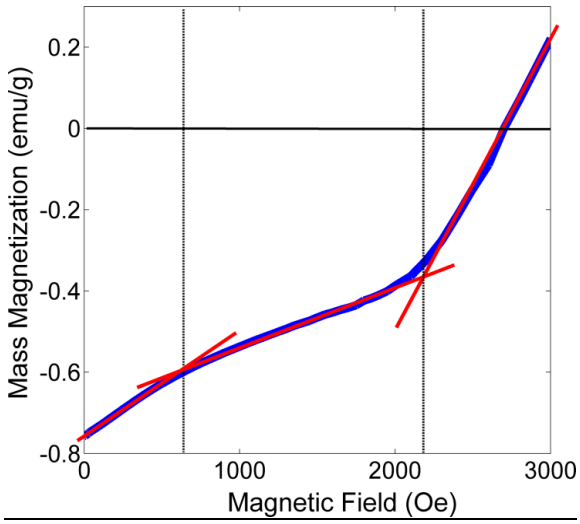

Figure III.12. Isothermal magnetization measurement performed at 5 K for a sample displaying spontaneous N-MRV after a 70 Oe field cooling procedure. The red lines are a guide to the eye, while the vertical dashed lines highlight the slope discontinuity points. *[image taken from Ref. 22].*

C.3.3 Hysteresis measurements

Magnetization hysteresis measurements performed at 300 K, 280 K, 240 K, 100 K and 5 K are reported in Figs. III.13a-b. The hysteresis loops were cyclically measured starting from 50 kOe up to –5 kOe and back after a field cooling in a low magnetic field (70 Oe). All the collected data show high field magnetization trend typical of an AFM system since magnetization increases linearly with the field.

However in the low field regime two different behaviors, taking place below and above T_3 = 250 K respectively, can be discriminated. At higher temperatures curve, the weak ferromagnetic component gives rise to a small remanent magnetization (*0.012 emu/g*) and to a superparamagnetic-like behavior, characterized by a negligible hysteresis. This can be justified by the presence of mesoscopic contributions, the same possibly responsible for the high-*T* broad magnetic signal detected by neutron diffraction. Below T_3, at 100 K, the spontaneous magnetization increases and the hysteresis loop abruptly starts opening out,

showing a complex shape probably due to the overlap of two different weak ferromagnetic contributes (see the blue curve of Fig. III.13b). Finally at 5 K the presence of two symmetrical kinks (Fig. III.13a) suggests for the two weak ferromagnetic components a "soft" and a "hard" character respectively. The obtained value of remanent magnetization is *0.062* μ_B*/F.U.*, while the overall coercive field is about 2500 Oe. These last comments are in complete accordance with the preliminary results of the isothermal characterization. Consequently, another remarkable M(H) characteristics (the increase, below T_3, of the high field susceptibility by decreasing the temperature) could be precisely expected for systems where MRV originates from the competition of two independent magnetic components with different exchange constants, the weaker dominating at lower temperature, as predicted by Néel (see subchapter *III.D* on MRV).

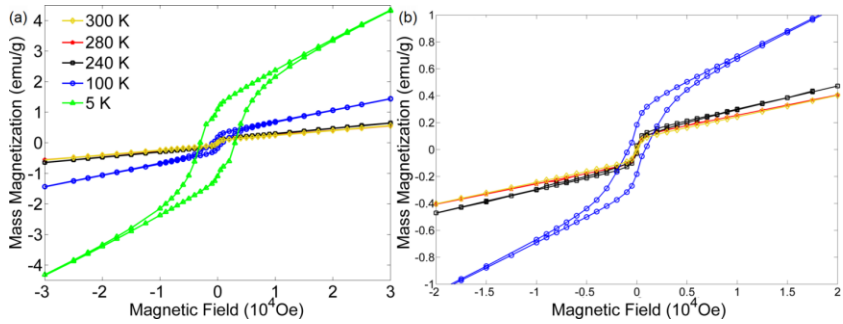

Figure III.13. (a) Hysteresis loops measured at different temperatures from RT to 5 K. (b) Hysteresis loops at 100 K, 240 K, 280 K and 300 K. are enlarged. At 100 K, it is clearly observed the presence of a sensible stricture in the central part of the curve possibly indicating the superimposition of two different magnetic contributions. *[image taken from Ref. 11].*

To sum up, the existence of an hysteretic magnetic behavior, clear at 5 K and less pronounced at 100 K, even though it origins from weak ferromagnetic contributions is a really fascinating aspect in the rush towards multiferroism. Furthermore the concomitant presence of two weak ferromagnetic phases in low field conditions together with the global antiferromagnetic nature, evinced by the linear trend of the M(H) curve above 10 kOe, give a further support to the hypothesis of a second-order nature of BFMO weak ferromagnetism. In addition, a further hypothesis may be proposed: the soft and hard weak ferromagnetic

phases can be competitive entities, and if this statement is accepted, from their competition may arise the MRV process. This suggestive statement arise from the fact that a maximum occurs in the thermal magnetic susceptibility measurement of Fig. III.9, marking the clear presence of two phenomena of equal magnitude but opposite direction. The experimental verification of these hypotheses go at this stage beyond the basilar and crucial goal of this study: the research of multiferroism and magnetoelectricity in BFMO.

C.3.4 Recap about BFMO magnetic properties

The disordered BFMO solid solution shows unpredicted magnetic proprieties. The compound displays a paramagnetic nature above T_1 = 420 K. The calculated Curie-Weiss temperature and the number of Bohr magnetons confirm the AFM non-frustrated magnetic structure and the exclusive presence of Fe^{3+} and Mn^{3+} ions. At the same time, although the global antiferromagnetic response of the compound is confirmed also by a series of isothermal measurements, AFM exclusively appears in high field conditions.

The low field regime pictured a completely different situation:

- a complex two step transition leading to spontaneous magnetization reversal (MRV) is recorded once the sample is cooled below T_N = 288 K;

- a narrow kinked-hysteresis loop with low coercive field and remnant magnetization is measured below 100 K.

Both these phenomena are supposed to be strongly related to the disorder and inhomogeneity affecting the TM ions at the B-site, as proposed in Ref. 11 and Ref. 20. Consequently at least two predominant magnetic contributions, (confined at the mesoscopic scale, since they are hidden at the eye of neutrons), characterized by two different resultant magnetizations, two different magneto-crystalline anisotropy energies and ordering temperatures, compete with each other. Their existence is supported by the observation of two singular fields (H_1, H_2) and two singular temperatures (T_1, T_3).

At this stage BFMO seems to have a promising feature since it is an antiferromagnetic material (and this helps ferroelectricity, as introduced in subchapter *II.C*) but at the same time it behaves as system with magnetic memory, at least in the low magnetic field regime.

C.4 Transport and dielectric properties of BFMO

C.4.1 Transport properties analysis

The preliminary stage of this study was the comprehension of the electrical character of $BiFe_{0.5}Mn_{0.5}O_3$ by means of transport properties characterization [23]. In fact, the choice of the following protocol of characterization depends on the observation of an ohmic or rather a dielectric character of the compound.

BFMO electrical dc resistance, measured for different applied voltages, is reported in Fig. III.14a in a variable thermal range between 77 K and 352 K. The results are fairly independent on the applied voltage and highlight two transitions located at $T_P \approx 140$ K and near $T_2 = T_N = 288$ K, as shown in Figs. III.14b-c. The trend qualitatively reproduces a typical exponential *T*-dependence, at least above T_P. Indeed the cooling of the system below T_P induces a clear transition, detected for each measurement (see Fig. III.14c). Therefore, at low temperatures, BFMO evolves in a pure dielectric state characterized by a very high resistivity (> 10 GΩ·cm); this is why the curves result very noisy in this thermal range.

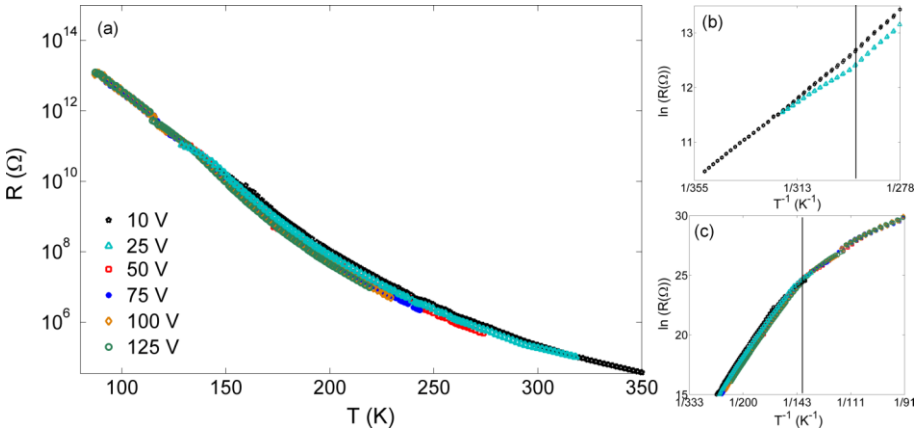

Figure III.14. (a) Electrical dc resistance as a function of temperature measured for different applied voltages and plotted in logarithmic scale. (b) Arrhenius plot showing a clear transition at $T_P \approx 140$ K in the transport mechanism. (c) Arrhenius plot in the high temperature range showing a less pronounced transition at T_N. *[image taken from Ref. 23].*

The detection of such concomitant effects suggests the occurrence of significant variations in the electronic structure. I hypothesize that once the system is cooled, the incoming long-range magnetic order forces the electrons localization. Consequently the system collapses into an insulating phase, so that the transition can be interpreted as a full localization of the electrons on the Mn^{3+} ions. Above 140 K and up to the Néel temperature 288 K, the transport mechanism presents a regular thermal dependence that has been studied utilizing three main models, usually adopted in similar systems [24,25]. These models are: the semiconducting thermal activated transport (TA) [26,27,28], the Adiabatic Nearest-neighbors Hopping of Small Polarons or Holstein polaron model (ANHSP) [29], and the 3D Mott's Variable Range Hopping (3D M-VRH) [30,31] (Eq. III.1, Eq. III.2 and Eq. III.3 respectively):

$$\rho = \rho_0 \cdot \exp\left(\frac{E_A}{kT}\right) \quad \text{(III.1)}$$

$$\rho = \rho_0 T \cdot \exp\left(\frac{E_{HOP}}{kT}\right) \quad \text{(III.2)}$$

$$\rho \approx \rho_0 \cdot \exp\left[\left(\frac{T_0}{T}\right)^{\frac{1}{4}}\right]. \quad \text{(III.3)}$$

In Eq. III.1, the TA law, k is the Boltzmann constant, T the absolute temperature, E_A the activation energy and ρ_0 the value of resistivity at infinite temperature. This equation is usually applied to crystalline semiconductors with a well-defined energy gap, for which the activated character is determined both by the electrons jumping in the conduction band from the valence band or similarly from the impurity levels to the conduction band.

In Eq. III.2, the ANHSP law is obtained through the assumption that the polaronic transport origins from an crystalline system in adiabatic conditions where the mobility of the carriers has still a thermal activated form. In this formula the effective resistivity is defined as $\rho_0 = 2k/(3ne^2a^2v)$, n is the density of charge carriers, e is the electronic charge, a is the hopping spatial distance and v is the longitudinal optical phonon frequency. Finally, E_{HOP} is the hopping threshold energy of the transport process.

The last equation (Eq. III.3) reports the M-VRH expression of resistivity for a non-crystalline disordered magnetic phase characterized by a 3D conductance, in which carriers localized through random potential fluctuations lead the observed transport. Herein, the critical parameter T_0 is directly proportional to the Mott localization energy: $T_0 = \lambda\alpha^3/[kN(E_F)]$, where λ is a dimensionless constant, α corresponds to the inverse of localization length and $N(E_F)$ is the density of states at the Fermi level. For what concerns ρ_0, this parameter owns the dimension of a resistivity but depends on the assumption made on the electron-phonon interaction and for this reason is slightly affected by temperature, but such dependence in most cases is negligible with respect to the exponential term of the equation. I performed interpolations of all the experimental data using those three different models, after the linearization of each curve by means of logarithmic transformations. The results, gathered in Table III.3, identify the M-VRH model as the one that better approximates the data for $T < T_N$, showing $R^2 > 0.9995$ for any applied electric voltage. M-VRH is usually employed to describe the resistivity behavior of disordered phases, in which the transport mechanism is leaded by carriers localized by random potential fluctuations. This model finds support from the consideration that BFMO is a disordered and inhomogeneous compound.

Table III.3. Coefficients of determination (R^2) calculated applying TA, ANHSP, M-VRH and 1D M-VRH models for each $R(T)$ curve in the two regimes $T_P < T < T_N$ and $T > T_N$. *[table taken from Ref. 23].*

Model/Voltage	**TA**	**ANHSP**	**3D M-VRH**	**1D M-VRH**
$T_P < T < T_N$				
10	*0.9817*	*0.9802*	*0.9997*	***1.0000****
25	*0.9845*	*0.9816*	*0.9997*	***1.0000****
50	*0.9818*	*0.9763*	*0.9996*	***1.0000****
75	*0.9887*	*0.9844*	*0.9996*	***1.0000****
100	*0.9990*	*0.9879*	*0.9997*	***1.0000****
125	*0.9991*	*0.9888*	*0.9997*	***1.0000****
$T > T_N$				
10	***0.9996***	***0.9997***	*0.9890*	*0.9931*

***** The value is rounded to the fourth decimal place for uniformity with the other data, even though the uncertainty is at least on the sixth decimal place.

Despite the agreement with M-VRH is visibly better with respect to that with the other models, the goodness of the interpolation could be further improved. The premise in doing this step forward arises from treating BFMO not as a pure magnetic disordered system. Indeed, as it has been shown in previous works [11,20] the strong compositional inhomogeneity is responsible for many significant magnetic features, as for example the spontaneous thermal activated magnetization reversal, a phenomenon that acts in a wide thermal range and well overlaps in temperature with the M-VRH transport mechanism. This inhomogeneity has a clusterized mesoscopic size and in principle may create low dimension paths with different variable range hopping resistivity. The generalized Mott's theory accounts for different degrees of dimensional conductance (and/or resistance) so that Eq. III.3 can be more precisely rewritten as:

$$\rho \approx \rho_0 \cdot \exp\left[\left(\frac{T_0}{T}\right)^{\frac{1}{D+1}}\right], \qquad \text{(III.4)}$$

where *D* indicates the dimension of the conductance.

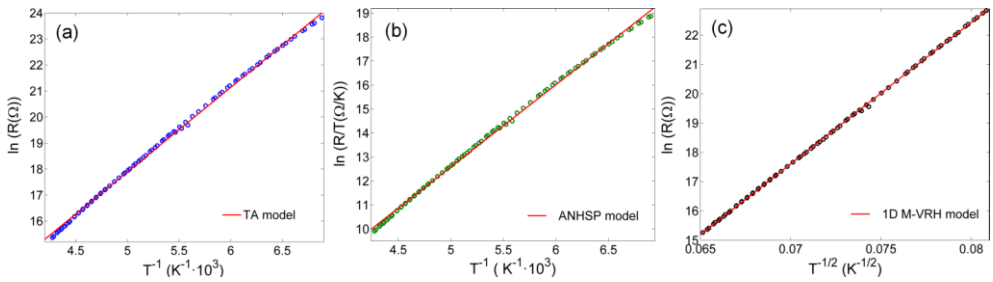

Figure III.15. Resistance data collect at 50 V and fitted by means of different models: TA (a), ANHSP (b), 1D M-VRH (c). Differently from (a) and (b), (c) shows an excellent linear agreement. [image taken from Ref. 23].

The lowered dimensionality $D = 1$ of the transport mechanism permitted to obtain a surprising convergence to $R^2 = 1$ (see Table III.3) of the interpolations for each curve, denoting a perfect agreement with the experimental data (Fig. III.15). Considering this, the best fit parameters obtained within the 1D Mott's Variable Range Hopping (1D M-VRH) have been deduced and then averaged between each applied voltage case. The estimated $T_0 = (2.34 \pm 0.2) \cdot 10^5\ K$ is close to the values found in similar perovskitic systems [23] and suggests a quite high Mott localization energy, considering the definition of Eq. III.3. This result likely corresponds to the presence of 50% of non Jahn-Teller active Fe^{3+} ions on the B-site enhancing the electrical barrier against the polaronic hopping between the 50% of Jahn-Teller active Mn^{3+}, which tends to localize the electrons on the Mn site. Furthermore, I obtained from T_0 the experimental value of the density of states at the Fermi level $N(E_F) = 9.78 * 10^{21}\ (eV \cdot cm^3)^{-1}$, using a value of α (the inverse of the localization length) of $2.22\ nm^{-1}$ and a value of $\lambda \approx 16$, in analogy with other manganites [24,32].

This result is quite significant and needs further considerations. The system seems to be guided by a quasi-mono-dimensional conductivity rather than a three-dimensional one. A possible explanation is given by the observation of the same behaviors in what are usually called "periodical granular metals arrays" predicted by Efros and Shoklovskii [33,34] and then verified experimentally in different compounds and morphologies [35,36,37]. Taking into account this model, together with the known strong compositional inhomogeneity on the B-site of BFMO [11,20] it may be hypothesized that an array of clusters, solely constituted by Jahn-Teller active Mn^{3+} ions on the B-site, may create an almost mono-dimensional macroscopic path and thus vehicle the current flow by means of a polaron mechanism.

In addition, another picture arises from the electric transport analysis in the high-T regime, above the Néel temperature. In this temperature region I performed a resistance vs T measurement for an applied voltage of 10 V. The preliminary analysis revealed an intriguing scenario: just above T_N the trend of the resistivity moves away from the M-VRH models and tends to converge towards a kT-model (TA and/or ANHSP, Eq. III.1 and Eq. III.2, respectively), as evidenced in Table III.3. This outcome seems to prove that the process of magnetic disordering modifies the nature of transport in correspondence of the AFM-to-

paramagnetic transition. In this context, there is no more distortive effects due to the Jahn-Teller effect of Mn^{3+} responsible for a polaronic mechanism, and so I am not able to distinguish Mn ions from Fe ions at least in terms of electric transport. Hence it is reasonable to picture the whole system, for $T > T_N$ as a pure disordered system and to state the space-invariance of the electrical potential. Through this hypothesis the M-VRH models are no more applicable and the Boltzmann thermal activated mechanism is favored. From the fit analysis, it turns out that the transport is now characterized by an $E_A = 350\ meV$, which corresponds to a temperature of almost $4000\ K$. This high thermal gap confers a resistor-like character to the compound and would permit a complete dielectric characterization, at least from RT to lower temperatures.

C.4.2 Dielectric properties analysis

The BFMO dielectric constant was characterized as a function of temperature and frequency of the applied electric field. A selection of curves corresponding to four particular frequencies (3 kHz, 11 kHz, 600 kHz and 1 MHz) is shown in Fig. III.16. First of all a huge decrease of the relative dielectric constant is detected as the system is cooled, namely the dielectric constant changes from ~*50* in the high frequency-high temperature limit to ~*38* in the static low temperature limit.

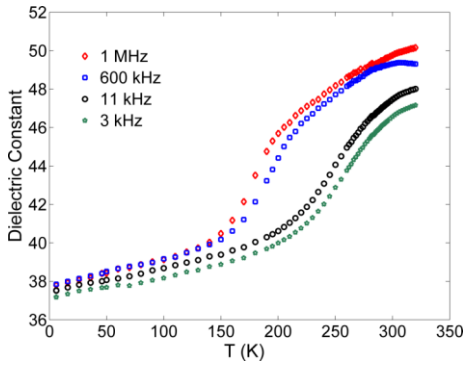

Figure III.16. Dielectric constant of $BiFe_{0.5}Mn_{0.5}O_3$ as a function of temperature for different frequencies of applied electric field. *[image taken from Ref. 23].*

This phenomenon starts at around T_N = 288 K ending up between 150 K and 200 K for the high and low frequency measurements respectively. Below these temperature thresholds the system behaves as a real dielectric, evidencing a weak and linear temperature dependence of the dielectric constant as the system is cooled.

The dynamics of lowering and stabilization of the electrical permittivity roughly overlaps the same temperature interval necessary to the magnetic long-range order of the system to completely settle (see Fig. III.9). This distribution in temperature probably arises directly from the inhomogeneity on the B-site of the perovskite; in particular, the presence of regions highly rich in Mn^{3+} which require lower temperature to become magnetically ordered.

C.4.3 Recap about BFMO transport and dielectric properties

The electrical properties of the bulk polycrystalline double perovskite $BiFe_{0.5}Mn_{0.5}O_3$ are characterized by three distinct thermal regimes: $T > T_N = 288$ K, $T_P \approx 140$ K $< T < T_N$ and $T < T_P$, where T_N is the Néel temperature and T_P is the insulator-semiconductor transition temperature. It is worthy to note that the Néel temperature is also a critical temperature for both transport and dielectric properties.

$T > T_N$

This regime overlaps with the paramagnetic region of the material; here the system behaves as a band gap semiconductor, the transport is managed by a thermally activated mechanism characterized by an activation energy $E_A = 350\ meV$.

$T_P < T < T_N$

This regime begins, on cooling, at the antiferromagnetic transition temperature T_N, when the Fe-O-Mn superexchange interaction sets in. This interaction acts in localizing the electrons that are partially involved in the magnetism. The Jahn-Teller active Mn^{3+} ions promote a

different transport mechanism, typical of cationic disordered systems: the Mott's Variable Range Hopping. In this scenario, the variable electrical potential is created by the Fe^{3+} ions which are statistically interposed between the active manganese ions. Therefore, the polaronic transport is accompanied by a huge increase of the macroscopic resistivity of the material as the temperature is lowered. Furthermore, the compositional inhomogeneity, already responsible for the intriguing spontaneous thermally activated magnetization reversal, also affects the electrical transport in this regime. In particular the mesoscopic regions (clusters) mainly constituted by Mn^{3+} ions represent a low resistive path for the current since the effective potential barrier is lowered by the negligible number of Fe^{3+} ions. Accepting this hypothesis, supported by the excellent reliability of the interpolations, the polarons may preferably jump from a Mn-rich cluster to another along those macroscopic percolative paths (periodical granular arrays), determining the observed transport mechanism.

$T < T_P$

In the lower T regime, at T_P, the system crosses a clear electrical transition, individuated by both dielectric and resistivity characterization; consequently, it collapses in a pure dielectric insulating state as the system is cooled.

The fascinating correlation between disorder, transport and dielectric properties and also magnetism discussed in this section, preludes to the possible existence of macroscopic magnetoelectric effects also in other bulk polycrystalline Bi-based perovskites and potentially in other similar bulk disordered magnetic systems.

C.5 Pyroelectric, ferroelectric and magnetoelectric characterization of BFMO

C.5.1 Pyroelectric and ferroelectric characterization

Once determined the BFMO dielectric regime, pyroelectric measurements were performed to investigate the eventual presence of polar properties. The pyro-current signal was collected during a time-controlled heating ramp from 5 K to 320 K. Before that, a DC electric poling of about *1.4 kV/cm* (*50 V*) was applied at 125 K for thirty minutes and then the system was cooled down to 5 K. The overall behavior of pyro-current is quite complex, characterized by two principal regimes with opposite sign of current flow (see Fig. III.17).

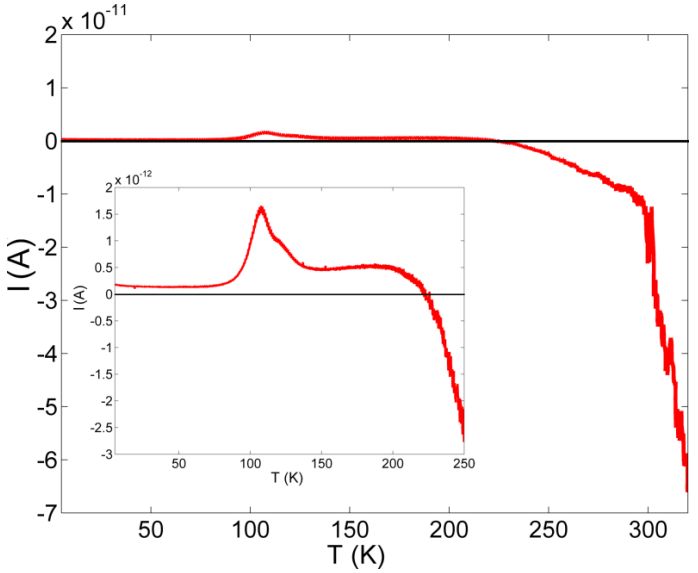

Figure III.17. Pyro-current response during a time regulated thermal heating. In the inset, the zoomed low temperature displacive region. *[image taken from Ref. 23].*

The negative sign region is characterized by conductive losses through the sample, as it can be argued from the activation energy $E_{A,p} = 360\ meV$ obtained by the Arrhenius plot of Fig. III.18 in the range $T > T_N$: in fact such a value is very close to the value $E_A = 350\ meV$ obtained from DC-electrical resistance measurements in the previous section. The discontinuity at $T \approx 345$ K does not affect the value $E_{A,p}$ and could be due to possible contact effects. The pyro-current region characterized by a positive sign originates from the sample

thermal depolarization. This is coherent with the preexistent knowledge about this compound. As previously reported, the space group of the system is indeed centrosymmetric, but the spatial symmetry arises from an antiferroelectric arrangement of the Bi ions that are significantly shifted from the neutral position and at the same time compensated from an identical but opposite shift of the surrounding Bi ions. However, looking at the inset of Fig. III.17, the effect of the dc electric poling (performed at 250 K) seems to induce an antiferroelectric-ferroelectric transition since a current peak has been measured in a relatively short thermal region between $T_P \approx 140$ K and 90 K.

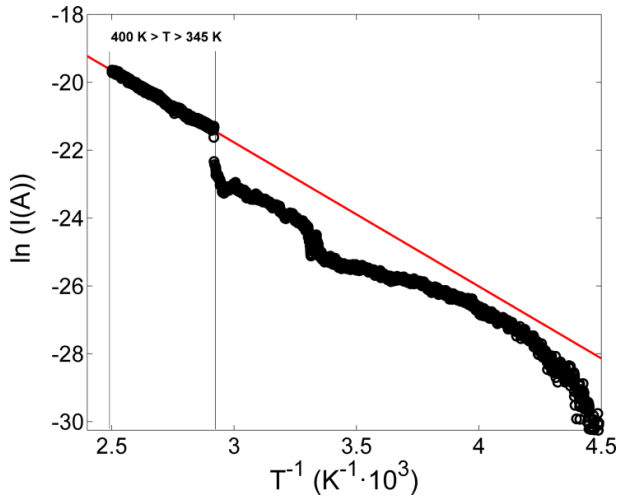

Figure III.18. Pyro-current Arrhenius plot fitted with a thermal activated model between 350 and 400 K. *[image taken from Ref. 23].*

This peak may be associated with a depolarization current that moves the system from the induced polar symmetry back to the centrosymmetry (that implies antiferroelectricity) precisely when the M-VRH polaronic transport sets in at the expense of the dielectric response. The temperature T_P can be thus defined as the critical temperature of an insulator-to-semiconductor transition, being observed simultaneously with three different characterization techniques: dielectric, transport and pyroelectric measurements.

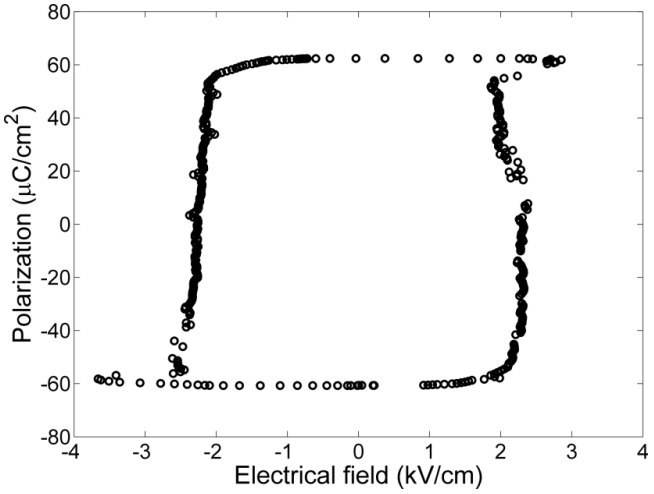

Figure III.19. Ferroelectric loop obtained with a DHM protocol, exploiting fast triangular electric pulses with frequency of 2000 Hz. The measurement was performed at 77 K. *[image taken from Ref. 23].*

In Fig. III.19 I present the first ferroelectric hysteresis loop ever reported in literature on a bulk phase of $BiFe_{0.5}Mn_{0.5}O_3$, collected at 77 K. Ferroelectricity is induced through an external electrical field poling $E_P \approx 5.7\ kV/cm$ and collected by a Dynamic Hysteresis Measurement (DHM). The obtained saturation polarization $P_S = 60\ \mu C/cm^2$ and the coercive electric field $E_C \approx 2.2\ kV/cm$ indicate a material with a very significant polarization and a soft character. I tentatively checked the RT electric charge vs. voltage behavior, but in this regime, the pure conductive contribution (as evidenced by all the previous characterizations) becomes predominant with respect to the dielectric one so that I were not able to observe the persistence of this polar character at higher temperatures.

C.5.2 Magnetoelectric characterization

The demonstration of a thermal range in which magnetism and ferroelectricity coexists, does not say anything about the presence of magnetoelectricity. To verify the presence of a magnetoelectric coupling a measurement of electric properties as a function of temperature at different applied magnetic field and a measurement of the magnetic response as a function of the applied electric field is needed. So I performed a magneto-dielectric study

measuring the dielectric constant thermal dependence with the application of an external magnetic field of different intensity (0 Oe, 500 Oe, 1000 Oe and 2000 Oe), exploiting the so-called dielectric probe described in section *II.G.2*. Some of those results are plotted in Fig. III.20 by selecting six different frequencies of the applied electric field. Noteworthy, the tested sample was the same that was previously poled and which gave rise to the ferroelectric hysteresis displayed in Fig. III.19.

At first sight, in the dielectric range between 5 K and 150 K, a strong modification with respect to the same sample measured in Fig. III.16 is evident for each electric field frequency. Specifically a peak appears positioned around 60 K ÷ 70 K. This is probably due the occurrence of a transition from the antiferroelectric non-polar arrangement in favor to the polar one. Indeed, a similar structural transition justifies and theoretically implies a peak in the dielectric order parameter. This is surprising because denotes the occurrence of an irreversible process appeared after the poling operation, performed as mentioned at 77 K. Even more surprising is the light but visible dependence of the peak magnitude on the applied magnetic field intensity. In particular, slight changes are detected comparing the curve measured at 0 Oe and 500 Oe; but for fields higher than H_1 = 650 Oe the intensity of this anomaly is sensitively reduced for each frequency (e.g. it goes from $\varepsilon_R \approx 40$ to $\varepsilon_R \approx 39$ of maximum intensity for the measurement collected at 160 kHz). In addition, a broad shoulder is observed also around 100 K, clearer for the curves collected at high frequency.

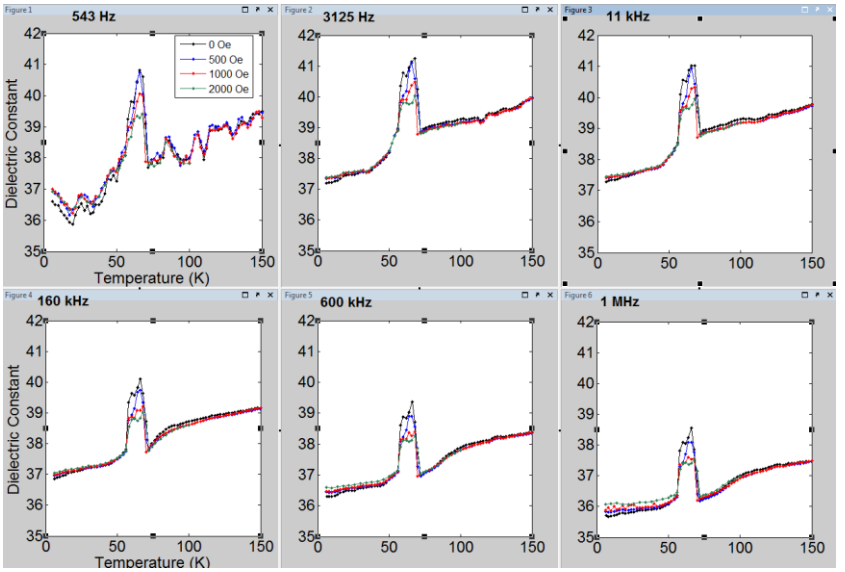

Figure III.20. Thermal dielectric constant evolution without applied magnetic field (black curve) and with different applied fields of 500 (blue) 1000 (red) and (2000 Oe) for six different frequencies of the electric field 543 Hz, 3125 Hz, 11 kHz, 160 kHz, 1 MHz.

In this framework the magnetic field seems to work competitively with respect to the induced ferroelectricity, acting to recover the structural symmetry. Nevertheless, this is the first important evidence of a magnetoelectric coupling: a clear magnetocapacive effect of BFMO can be rapresented plotting the thermal dependence of the relative variation of in-field dielectric constant with respect to the zero-field one (see Fig. III.21).

As it can be appreciated, the effect of the magnetic field in lowering the dielectric constant results in three different peaks located at 60 K, 64 K and 70 K. In the case of 500 Oe the maximum magnetocapacitive effect is observed at 60 K, with a relative variation of 1.8%. In the case of 1000 Oe the maximum effect is at 64 K and 70 K with a relative variaton of about 2.6%.

In analogy, the same sample thermal resistivity and pyroelectricity is studied under magnetic field application. Nevertheless, for these two parameters have not been observed significant *H*-induced changes.

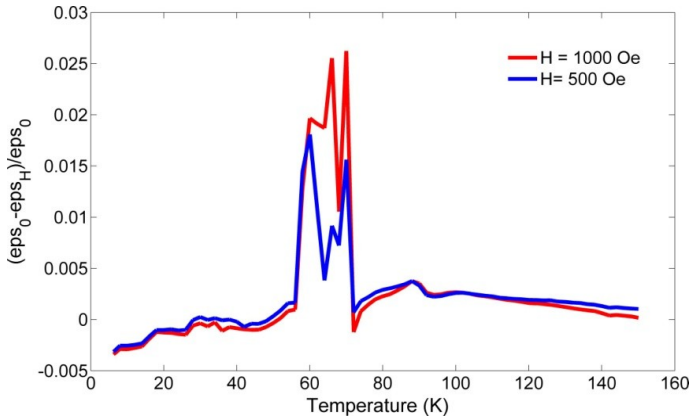

Figure III.21. Mangnetocapacitive effect on BFMO in the case of 1000 Oe and 500 Oe measurement with respect to the zero magnetic field curve collected at 160 kHz.

The demonstration of structural changes and magnetolectric correlation persuaded me to investigate, by means of the magnetoelectric probe (introduced in section *II.G.2*), also the thermal behavior of zero-magnetic field spontaneous magnetization as a function of an applied electric field.

The protocol of the measurement is listed below.

- Annulment of any residual magnetic field of the SQuID magnetometer.

- Centering of the sample at H = 0.

- Cooling procedure down to 6 K.

- First ZFC measurement without any field applied from 6 K to 320 K (blue dots curve in Fig. III.22).

- Cooling down again to 125 K: at 125 K the electric DC field poling is switched on and then the system cooled down to 6 K. This is the Electric Field Cooling (EFC) procedure.

- The electric field is switched off, then a new ZFC measurement is performed without any applied fields from 125 K to 6 K.

The choice of 125 K as starting temperature for the application of the electric field originates from observation of a peak in the pyroelectric current measurement around this temperature, but also because such operation can be effective only below T_P, or rather in the dielectric regime of BFMO.

The results are plotted in Fig. III.23.

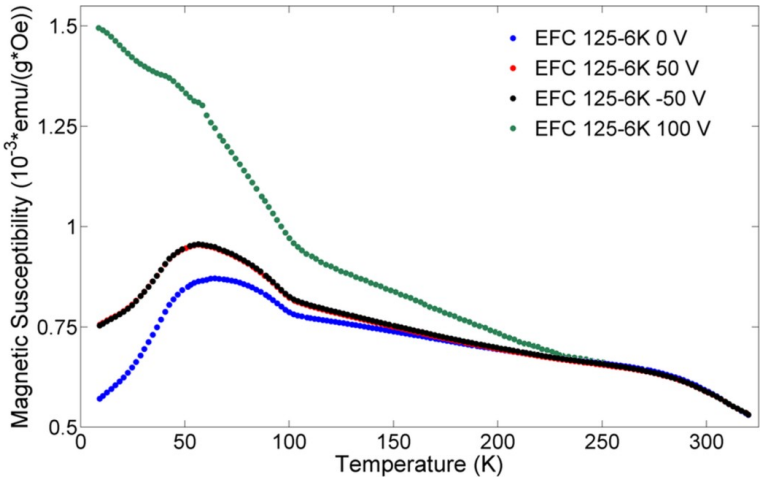

Figure III.22. ZFC characterization with H = 0 recorded in the thermal range between 6 K and 320 K for the poled sample showing ferroelectric hysteresis of Fig. III.19. The curves have been collected after different EFC between 125 K and 6 K. During the ZFC measurement the electric field is swtiched off.

The phenomenology of BFMO spontaneous magnetization is very intriguing. In analogy with the huge variation detected on the poled sample in the dielectric characterization under standard conditions (i.e. H = 0), this measurement confirms that the poling process causes, besides the irreversible structural modification, a deep change of the magnetization characteristics with respect to the virgin case reported in Fig. III.9: above all, the cancellation of the MRV process.

In EFC 0 V (blue dots curve of Fig. III.22), the antiferromagnetic transition is still present at T_N, but once the temperature T_3 is reached, the expected maximum in the magnetization does not occur, and as the system is cooled, it follows an almost linear trend up to ~100 K .

Here a second big difference appears. Below 100 K, the magnetization starts to increase followed by a maximum located in the range 60 K ÷ 70 K where a peak in the dielectric constant is observed (Fig. III.22). Below 50 K and down to 6 K, the curve shows a typical low-*T* antiferromagnetic behavior. Therefore, the hypothesized structural polar transition deletes the second-order competition responsible for MRV, and gives rise to a simpler phenomenology. Furthermore, looking at the series of ZFC measurements performed after EFC procedure with different electrical poling intensities (in chronological order 50 V, 100 V and –50 V), the recorded behaviors show extraordinary features. The main effect related to the electric field intensity is the large increasing of the magnetic susceptibility, at least in the low temperature region. Specifically, the measured susceptibility at 6 K increases with respect to the zero-electric-field susceptibility by ~ 50% and by ~ 300% in the case of 50 V (red dots curve) and 100 V (green dots curve), respectively. Moreover, no sign dependence has been detected, being 50 V and –50V (black dots curve) completely overlapped. In addition, it is worth to note that the trend of the 100 V ZFC is similar to that of an antiferromagnetic material under sufficiently high magnetic fields, with the lack of the typical cusp.

Finally, the BFMO electric DC stimulation has strong consequences on its magnetic susceptibility thermal behavior, pointing out a clear interconnection between the lattice and the magnetic properties. In other words, the information written in the electric domains of BFMO by electric field poling turns out to affect the magnetic response of the material thorough a structural mediated coupling. As I showed commenting Fig. III.8 in subsection *III.C.2.2*, neutrons diffraction discriminated an effective spin-lattice coupling below the AFM order transition T_N confirming this last statement. Unfortunately, the same coupling is not detected by hysteresis measurement after electric field poling or rather by direct M(E) measurements. I learnt, to my cost, that temperature plays a key role in transferring the written electric (magnetic) information in the magnetic (electric) part. This is probably the main difference between a proper ferroelectric type-I multiferroics, as BFMO is, and a magnetically induced ferroelectric type II-multiferroic.

In order to confirm the validity of the conclusion carried out by the analysis of Fig. III.22, I performed a contradictory test, to exclude the presence of spurious effects on the magnetic

signal and due to electric components and contacts. To this aim I performed analog measurements on a virgin (never poled) sample. The results are gathered in Fig. III.23.

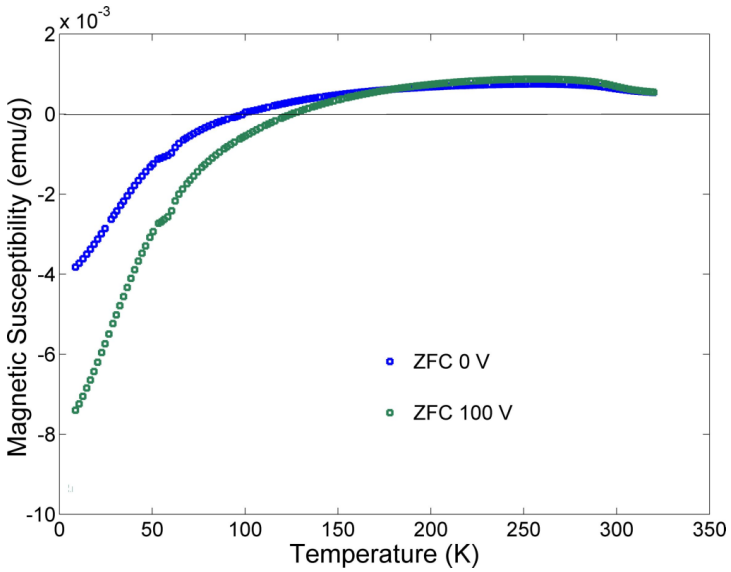

Figure III.23. ZFC characterization with H = 0 recorded in the thermal range between 6 K and 320 K for a virgin sample. The curves have been collected after zero EFC (blue curve) and 100 V EFC (green curve) between 125 K and 6 K.

In the present case ZFC collected after zero electric field cooling shows the same trend expected by BFMO in absence of an applied magnetic field under standard magnetometric characterization. The magnetic susceptibility is characterized by MRV occurring with the behavior observed in Fig. III.9. After the poling treatment with 100 V DC electric bias, the MRV process and the critical magnetic temperatures are both retained. Similarly to Fig. III.22, an enhancement of ~ 100% in modulus of the susceptibility with respect to zero-EFC is detected at 6 K. In addition, I report in Fig. III.24, the consistent increase of ~ 20% occurring also at 250 K, demonstrating that in this case, differently from the poled sample, the high-*T* ordered phase also responds actively to the electric field. The anomaly around 60 K ÷ 70 K is however well visible also in the virgin sample.

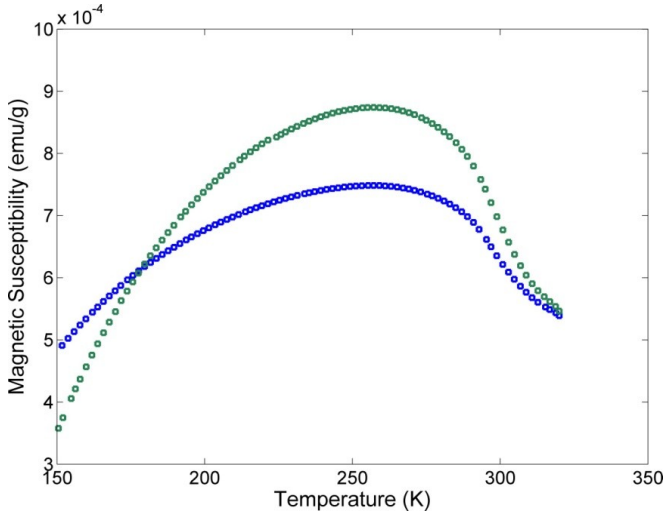

Figure III.24. Zoom of Fig. III.23 in the temperature range between 150 K and 320 K.

For the sake of completeness, as a final consideration I want to show the magnetic field cooling measurements. The aim of this further study was to figure out the eventual cumulative effect of the two fields.

Unexpectedly, the effect of a 100 Oe magnetic field, switched on during the crossing of T_N is to nullify the effect induced in the system by the electric field and recorded in the previous ZFC. As a consequence, Fig. III.25 displays an almost perfect superimposition of 0 V and 100 V EFC-FC curves. Moreover the anomaly around 60 K ÷ 70 K is substantially cancelled. In other words magnetic field recovers the magnetic response on non-poled conditions. This fact supports once again the competitive effect of the magnetic field on structure polarity, as already deduced from magneto-dielectric characterization.

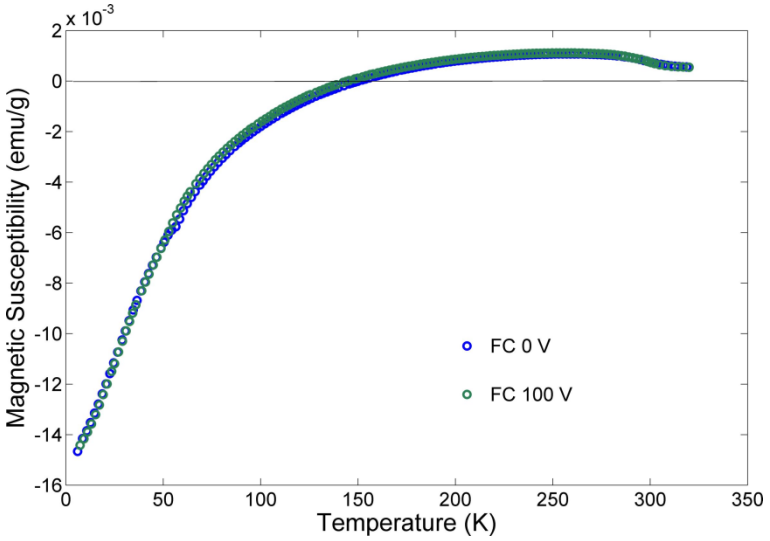

Figure III.25. FC susceptibility measured in cooling between 320 K and 6 K after the EFC procedure in warming at 0 V (blue circles curve) and 100 V (green circles curve).

C.5.3 Recap about the pyro and ferro-electric and magnetoelectric characterization

Pyroelectric characterization highlights that an external DC electric bias is able to induce in BFMO a net polarization which relaxes through a warming process around between 90 K ÷ 140 K with the classical depolarization peak. At higher temperature the pyro-current sign-reversal demonstrates the presence of a high leakage that can be fitted considering a thermally activated mechanism of a low-gap semiconductor with activation energy compatible with that calculated by the electric transport characterization.

Ferroelectricity has been directly measured at 77 K, by the AIXACCT tester, evidencing saturation polarization $P_S = 60\ \mu C/cm^2$ and the coercive electric field $E_C \approx 2.2\ kV/cm$, typical values of a material with a very significant polarization (comparable with that of BFO) and a soft character.

The induced polar transition is an irreversible process. It was characterized by dielectric constant measurements ε_R as a function of temperature, which displays the occurrence of a peak in correspondence to a short thermal range between 60 K and 70 K. This peak is possibly related to a structural phase transition from a low temperature ferroelectric

structure to a high-temperature centrosymmetric structure. In addition, dramatic effects of this induced polar character were observed also in the thermal magnetic susceptibility with the cancellation of the MRV process and the recovering of a pure antiferromagnetic behavior.

Specific magnetoelectric measurements brought to promising outcomes. The effect of an external complementary field is well visible both on the dielectric constant (magnetic field) and on the magnetization (electric field) responses. In particular:

1. the magnetic field is in competition with the polar structure, as it attenuates the intensity of the peak anomaly, reducing and potentially cancelling the occurrence of the structural phase transition, hence BFMO is a magneto-capacitive compound;

2.the electric DC poling increases the magnitude of thermal magnetic susceptibility at low temperature and gives rise to a new critical temperature at about 100 K. This fact is likely related to spin-lattice coupling, as already deduced from both neutron diffraction data (section *III.C.2*) and magneto-dielectric characterization.

Consequently, BFMO could be considered a weak magnetoelectric compound, with a lattice-mediated indirect coupling.

C.6 Conclusions on BFMO characterization

In this section I would like to sum up the main results that candidate bulk $BiFe_{0.5}Mn_{0.5}O_3$, for the first time in literature, as a multiferroic magnetoelectric material.

Bulk BFMO is a disordered Bi-based double perovskite only synthesizable under HP/HT conditions. It crystallizes in a highly distorted orthorhombic superstructure with *Pnam* centrosymmetric space group. This distortion is provided by a complex scheme of tilt and rotation of the coordination octahedra BO_6, ascribed to the stereochemical effect of the lone pair $6s^2$ orbital of Bi^{3+}. Strong compositional disorder affects the Fe^{3+} and Mn^{3+} distribution and it is responsible for many exotic properties, the most important of which are:

- the spontaneous magnetization reversal process (thoroughly treated in the following section)

- 1D Mott's Variable Range Hopping as mechanism of electric transport (see subsection *III.C.4.1*)

Despite the global antiferromagnetic nature of the interaction (T_N = 288 K), the compound revealed the coexistence of magnetic and electric hysteresis below T_P, the critical temperature of the semiconductor-to-insulator transition. This low T (weak)ferromagnetism arises from the antiferromagnetic structure, due to the presence of at least two kinds of mesoscopic clusters characterized by different magnetic interactions (and so different resultant magnetizations, coercive fields and critical temperatures) and probably by uncompensated magnetic moments, and thus producing a resultant weak ferromagnetic response in the low magnetic field regime. An electric poling forces a symmetry breaking just around 100 K inducing ferroelectricity: this process is irreversible.

The procured spatial symmetry breaking as well as the application of a DC electric poling seriously affects the magnetization response deeply modifying its thermal dependence. On the other hand, the dielectric anomalies detected at the occurrence of the spatial symmetry

breaking can be reduced directly by means of an external magnetic field application. Moreover a direct magneto-capacitive effect was also observed.

In conclusion, besides the proven superimposition of electric and magnetic order, a lattice-mediated weak magnetoelectric coupling was also demonstrated, allowing to define BFMO as a multiferroic magnetoelectric material.

Despite these extraordinary and novel results, the experimental activity on this compound is yet to end. Single crystal magnetic and electric measurements are needed to carry out some quantitative data on magnetoelectricity. This point is quite complex due to the difficulties in obtaining sufficiently great single by means of HP/HT synthesis in MA press. However the use of alternative techniques, as for example hydrothermal growth, are now under exploitation, even if a good outcome has not come yet. It also misses the crystallographic verification of the argued symmetry breaking, hypothesized to describe the development of the ferroelectricity after poling treatment. As far as the starting structural complexity is concerned, a subtle variation of the symmetry is not easy to see with standard X-Ray diffraction. For this reason, I am going to propose in 2015 an experiment to a European Synchrotron beam line facility. Although four years have passed since the first synthesis of BFMO, it still continues to astonish with new intricate issues.

D. On the nature of magnetization reversal in BFMO. A tale of a thorough study

I decided to commit a specific part on the description of magnetization reversal (MRV) mechanism, observed in BFMO and previously introduced. This unusual phenomenon attracts my attention since the first observation even though initially I considered it subsidiary to the search of multiferroism and magnetoelectricity. However the more magnetic characterizations I performed the more frequent were the occurrence of this physical property. At every turn, the way in which it appeared, seemed to me more complex. Therefore, in 2013 I started a specific study of MRV surely stimulated at first by my personal scientific interest but also by the laxity with which the majority of the scientists treated this unsolved issue in their papers (often treated as a spurious effect, not worthy and not valuable). In the following pages I discuss a thorough summary of this research activity that took time and energy. Finally, after one year and a half, I could say that I consider it as the most satisfactory result of my still short career.

D.1 MRV definition and brief state of the art

MRV is a magnetization sign change that occurs each time the system is cooled below a certain temperature (i.e. compensation temperature) but that can be switched on/off by modifying the intensity, and not the sign, of an applied magnetic field. MRV discovery hailed from L. Néel [38], that in 1948 theoretically predicted this mechanism in ordered ferrimagnets as a consequence of the presence of two different temperature dependences of sublattice magnetizations arising from magnetic ions at non-equivalent crystallographic sites.

Since Néel prediction, several systems (many of which are perovskites) showed MRV [39,40,41,42,43,44,45,46]. It should be noted that most of them are characterized by an ordered distribution of the magnetic ions.

Recently the occurrence of MRV was recorded also in some partially ordered or disordered magnetic perovskites, as for instance in $YFe_{0.5}Cr_{0.5}O_3$ [47] and $(La_{1-x}Bi_x)Fe_{0.5}Cr_{0.5}O_3$[48]; however in this case the explanation appeared not so simple and different mechanisms were take into account. Nowadays, an univocally accepted theory for the MRV description is still missing. For what concerns $BiFe_{0.5}Mn_{0.5}O_3$, the two current explanations ascribe the process to a thermally activated competition between DM interaction and single ion anisotropy [12] (hypothesis that is not strengthened by any experimental confirmations), or to an extrinsic process favored by the presence of inhomogeneities (but through contradictory and incomplete magnetic data) [20]. From a practical point of view, MRV phenomenon results to be highly sensitive to both the thermal and magnetic measurement conditions; so that a comprehensive characterization strategy must be planned. Strengthen by the belief of those criticalities, I used a combined approach made of in-field and standard Mössbauer spectroscopy on a 48% ^{57}Fe-enriched $BiFe_{0.5}Mn_{0.5}O_3$ sample together with specific series of magnetometric measurements in order to clarify the nature of MRV in the system. It will become clear that in principle the adopted strategy has a large applicability in the study of disordered perovskites showing a similar phenomenology.

D.2 BFMO MRV. An intrinsic phenomenon

The primary debated aspect was about the intrinsic or extrinsic nature of MRV in BFMO. In 2013, with the synopsis of Ref. 20, a scientist affirmed that in two BFO-BMO solid solutions (namely $BiFe_{0.7}Mn_{0.3}O_3$ and $BiFe_{0.6}Mn_{0.4}O_3$): *"... it was found that the magnetization reversal is dependent on magnetic prehistory of a sample and measurement protocols. No magnetization reversal was observed when the virgin samples were measured below T_N. Magnetization reversal effects appeared only when the samples were cooled in small magnetic fields from temperatures above T_N or after the samples were magnetized"* and it concludes *"…. tunable exchange bias effect was also observed on isothermal magnetization curves. Our findings allowed to propose the extrinsic origin of the magnetization reversal effect in these two compounds"*.

The big turning point concerns the fact that the MRV problem in BFMO is at last faced in this work. However another peculiar aspect fundamental and ever considered before, is that the author introduces the role played by the sample magnetic history and the applied measurement protocol together with the link (missing in this citation) with disorder, in the occurrence of MRV.

Nevertheless, the author of Ref. 20 unconsciously committed a small error that, in my opinion, invalidates the conclusion of the extrinsic nature of the MRV phenomenon. In fact, the claimed experimental evidence of the underlined affirmations is based on ZFC and FC measurements performed with a standard magnetic protocol: that is, in presence of a little magnetic field (10 Oe ÷ 100 Oe). This protocol commonly corresponds to the measurement of spontaneous magnetization: this is surely true for several materials, but BFMO.

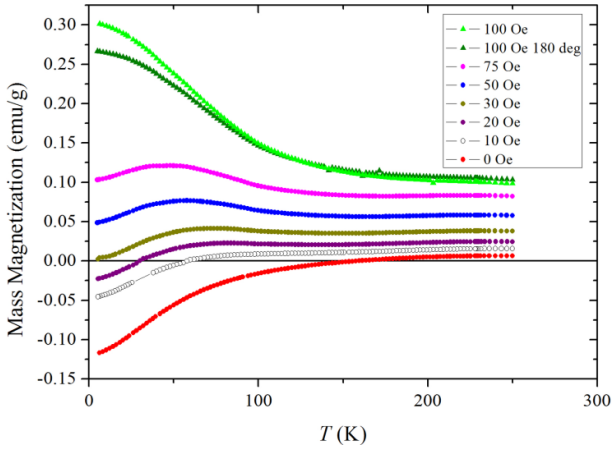

Figure III.26. The dependence on the applied magnetic field of the FC MRV effect for a virgin pellet measured starting from below T_N = 288 K, representing the long-range magnetic ordering temperature. MRV is suppressed for applied field equal or higher 30 Oe the MRV, otherwise the sign reversal always occurs, showing reproducible thermal dependence. *[image taken from Sup .Mat of Ref.11].*

In fact, with the results displayed in Fig. III.26, I demonstrated that MRV is present also collecting a FC measurement, if measured on a virgin sample below T_N, despite the cited sentence. At 0 Oe, 10 Oe and 20 Oe, magnetization reversal occurs and shows the expected trend as a function of temperature. As a confirmation of the author's observation, the green curve, measured at 100 Oe, do not show magnetization reversal anymore. Therefore, a measurement of *spontaneous* magnetization of BFMO can exclusively be performed at 0 Oe, after proper operations of field annulment in the SQuID magnetometer, because small fields, even of a few oersteds, seriously modify the magnetic response of the compound.

In addition to these considerations, also the second underlined sentence was contradicted by my tests. At least in the case of 50% Fe 50% Mn, BFMO solid solution does not highlight appreciable exchange-bias effects in the field cooled hysteresis loop, as reported in Fig. III.27.

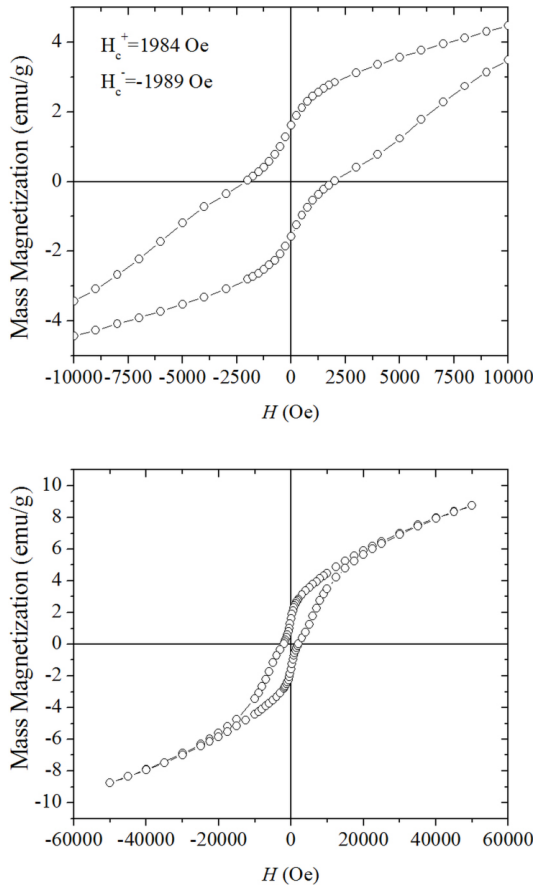

Figure III.27. Hysteresis loop after a fied cooling to 5K with an applied field of 50 kOe, following the procedure of Ref. 20. The upper panel shows an enlargement of the loop. No evidence of exchange bias is detected, excluding it as a possible explanation of an eventual extrinsecity of MRV. *[image taken from Sup .Mat of Ref.11].*

To conclude this section, BFMO magnetization reversal owns an intrinsic nature; this opens the doors to several possible explanations that shall be scientifically demonstrated.

D.3 BFMO MRV thermal dependence in zero-field condition

D.3.1 Magnetometric characterization

Zero Field-Cooling (ZFC) magnetic measurements in zero-field conditions, shown in the following, were performed on bulk pieces of HP/HT synthesized samples by using a SQuID magnetometer. Before each measurement, the residual field of the magnet was properly cancelled (< 0.1 Oe).

ZFC magnetization measurements were carried out by this procedure: the system was cooled to 5 K with no applied magnetic field, then, without switching on the magnetic field, the spontaneous magnetization was measured in warming.

I reaffirm once again that the magnetic behavior of this system (and by analogy of all the other disordered systems showing MRV), is dramatically influenced by the measuring procedure, in particular by the initial condition of the sample, the temporal/thermal operational sequence and the intensity of the applied field during the measurements. In zero-field condition, MRV is always observed and the system shows a Negative or Positive Magnetization Reversal (N-MRV or P-MRV, respectively), where N or P defines the orientation of the low temperature magnetization resultant (antiparallel or parallel) with respect to the positive direction of the field in the SQuID magnetometer. A reliable analysis of the magnetization data thus requires the exploration of all the possible variables which become accessible only by a number of measurements carried out in different conditions. Only in this way, a complete description of MRV in the system becomes possible and reliable.

In absence of an applied magnetic field the ZFC measurements (Fig. III.28) always reveal the occurrence of a magnetization reversal with respect to the initial room temperature (RT) spontaneous magnetization. Consequently, when the initial RT magnetization is positive (see black dots in the inset of Fig. III.28), an N-MRV is observed at low temperatures, while a negative initial RT magnetization (see red dots in the inset of Fig. III.28), gives rise to a P-MRV. In other words, this means that if N-MRV is measured for one orientation of the sample (black curve in Fig. III.28), a sample rotation of 180° must necessarily determine a P-MRV (red curve in Fig. III.28), as indeed detected. This feature clearly confirms the

intrinsic character of the MRV process, which is not related to possible residual field within the superconducting magnet or other spurious signals, but which simply derives from the RT spontaneous magnetization.

Similarly to the FC measurement of Fig. III.9, the curves of Fig. III.28 denote the same criticalities: precisely the AFM transition at $T_2 = T_N = 288$ K and, just below $T_3 = 250$ K, a maximum in the magnetization. The latter temperature represents a threshold marking the start of MRV process, as the system is cooled. The magnetic compensation occurs at 186 K and for lower temperatures, the system shows an opposite response.

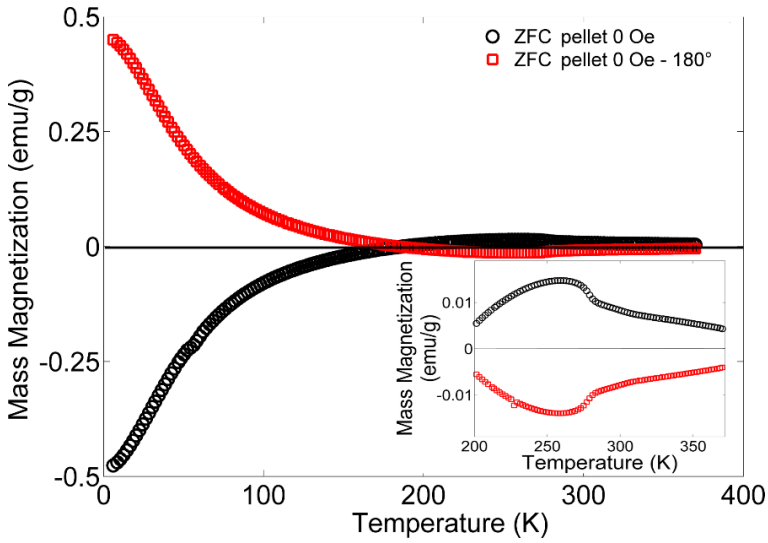

Figure III.28. $BiFe_{0.5}Mn_{0.5}O_3$ spontaneous magnetization collected in absence of applied external magnetic field for two different orientations of the RT resultant magnetization, parallel (black circles) and antiparallel (red squares) with respect to the positive magnetic field direction as highlighted in the inset plotted between 200 K and 370 K. *[image taken from Ref. 22]*.

D.3.2 Mössbauer characterization

Mössbauer spectra collected at different temperatures in the range 293 K ÷ 68 K are reported in Figs. III.29a-b. At high T values, the spectra are marked by a saturated, winged doublet, which arises from an unsaturated magnetic structure, extending from –8 to +8

mm/s, corresponding to hyperfine fields ≈ *45 T (450 kOe)*. By decreasing the temperature, the progressive disappearance of the wells between the magnetic lines indicates the growing of medium field components *(≈ 25 T = 250 kOe)*, rising from the simultaneous fall of the doublet intensity: around T = T_3 the external lines are flat and the depth of the doublet lines is comparable to the ones of the magnetic lines.

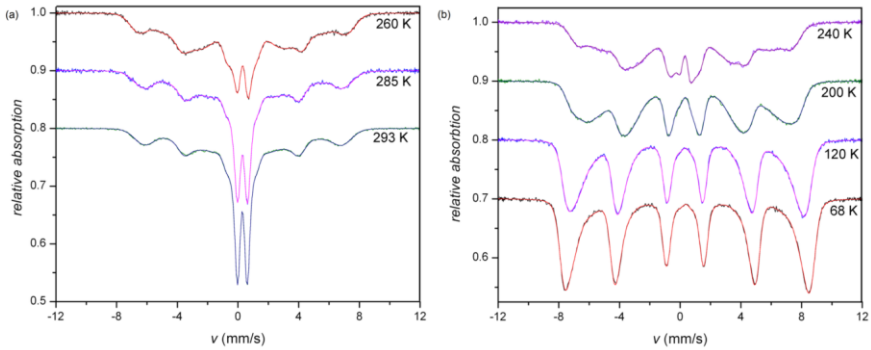

Figure III.29. Mössbauer spectra collected (a) above and (b) below T_3. *[image taken from Ref. 11].*

A further decrease of T affects the line-shape making the external lines to become well-defined again, suggesting a falloff in the medium field components (see Fig. III.29b). Therefore, the evolution of the Mössbauer cross-section is described by means of a doublet (sub-5) and four magnetic components, characterized by Gaussian field distributions, which lead to sextets of Voigt profiles [49,50]. One of them (sub-4) is used to fit the wings of the doublet and it should be considered as that part of the superparamagnetic-like component which takes into account inhomogeneous effects.

The three remaining magnetic structures describe the magnetically ordered part of the cross-sections:

- sub-3 describes the medium field component and a strong hyperfine mean field variation, starting around T_3 = 250 K,

- the last two (sub-2 and sub-1) are necessary to outline the high field components, since the low temperature spectra show asymmetric external lines.

All of these subspectra are also able to take into account inhomogeneous broadenings of the electric parameters (quadrupolar splitting and isomer shift) by means of an additional Gaussian distribution, whose line width returns to values lower than $2\Gamma_N = 0.2\ mm/s$. The electric parameters of the magnetic sextet used to fit the wings of the doublet were obviously constrained to the same values of sub-5 component.

The obtained RT values for the chemical shift of all the subspectra are in the $0.25\ mm/s \div 0.35\ mm/s$ range; as far as the quadrupolar splitting is concerned, the doublet and the associated magnetic component have Qs = 0.65 mm/s while all the other magnetic subspectra have $Qs < 0.30\ mm/s$. Moreover, for what concerns sub-4, the angle between the hyperfine field direction and the principal axis of the electric field gradient tensor results to $\beta \approx 0.8\ rad$. The obtained parameters for T = 68 K, 120 K, 200 K, 240 K, 285 K and 293 K confirm that the iron oxidation state is $3+$.

All the subspectra fields but the one related to sub-4 grow by decreasing T. Sub-1 can be associated to the high temperature order of the system preexistent at $T > T_2$, while sub-2 is involved in the low temperature magnetic transition since it shows a discontinuity in the thickness and in the hyperfine mean field at T_2, as shown in Fig. 12a. Moreover, around T_3, where the mechanism of reversal is thermally activated, the plot shows a substantial quenching of the sub-3 thickness and a maximization of the sub-2 one. The temperature dependence of the Gaussian broadenings for all the magnetic subspectra is illustrated in Fig. III.30b. Sub-4 is characterized by the highest relative variation and a Gaussian broadening. The Gaussian broadenings of the other components are of the order of few tesla and they decrease smoothly with T, making the spectral lines sharper.

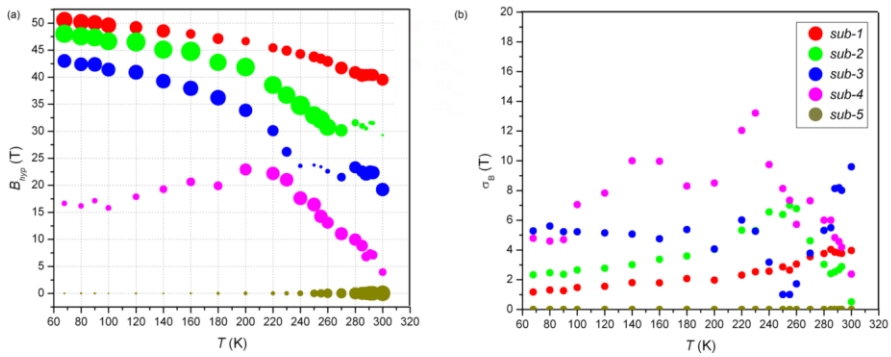

Figure III.30. (a) Thermal trend of magnetic hyperfine mean fields for the five subspectra (the areas of the dots are proportional to the corresponding Mössbauer thicknesses); (b) Gaussian width of the magnetic field distributions vs. T. The legend refers to both the graphics. *[image taken from Ref. 11].*

The magnetic fields distributions are derived from the parameters reported in Figs. III.30a-b and they are illustrated in Fig. III.31 for selected temperatures. They represent the key point for the MRV interpretation.

In correspondence to the high fields region, a peak emerged from a flat trend of the high-*T* distributions. By lowering T the distributions become double-peaked and finally they tend to collapse into a single peak. The main feature in the line shape thermal evolution concerns the thickness of the superparamagnetic-like doublet with its wings (sub-5 and sub-4), which starts to decrease exponentially with T at T_N, from 50% of the total thickness to a practically negligible percentage under 200 K. This transformation perfectly reproduces the incoming long-range antiferromagnetic transition that emancipates the statistically predominant Fe-O-Mn interactions depopulating the superparamagnetic contribute to the advantage of sub-2 and sub-3. In particular the slow dynamics of Mössbauer thickness enhancement and hyperfine field saturation shown by sub-3 well overlaps the dynamics of completion of the MRV process.

A second element to be noted in the thermal evolution of Mössbauer spectra regards the hyperfine field mean values of the sub-1 component, whose relative thickness is almost 20% of the total thickness over 200 K. Although its values are a few tesla smaller, the thermal trend of hyperfine field relative to sub-1 follows the one of $BiFeO_3$ [51,52] suggesting that

these iron ions are prevalently surrounded by irons ions in confined mesoscopic regions (clusters).

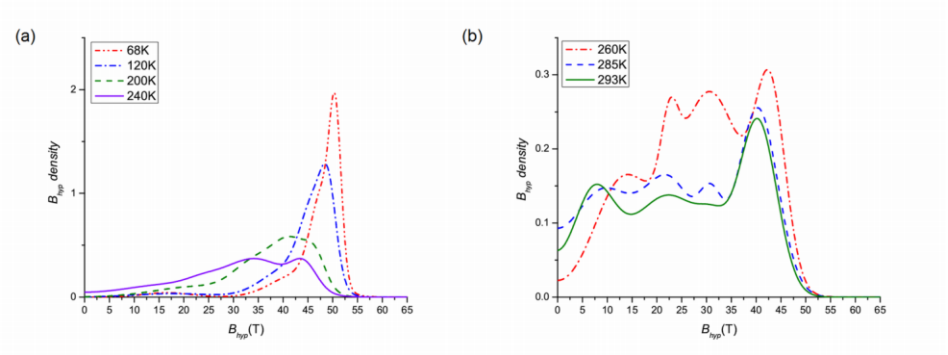

Figure III.31. Hyperfine magnetic field density at selected temperatures in the low (a) and high (b) T ranges, corresponding to strong and weak superparamagnetic-like components. The different scales for the vertical axis reflect the collapse of the superparamagnetic-like structure. *[image taken from Ref. 11].*

D.3.3 Interpretation of MRV thermal mechanism

The key for the interpretation of the MRV behavior is given by the Mössbauer data, showing above RT the presence of an ordered component (about 20% of the iron atoms) characterized by high hyperfine field values, together with partially ordered states and a superparamagnetic-like doublet. The latter shows an exponential decrease of the thickness as the temperature is decreased, disappearing at about 200 K. Since $BiFeO_3$ and $BiMnO_3$ display very different magnetic ordering temperatures (643 K and 105 K, respectively), it is likely to consider that also in a disordered solid solution, inhomogeneity is responsible for the occurrence of mesoscopic iron and manganese-rich clusters with different critical temperatures. The MRV phenomenon arises due to the disorder at the B-site.

In particular the iron-rich clusters give rise to the Mössbauer sub-1 component (Fig. III.30a). This interpretation also agrees with the broad and weak signal observed in neutron diffraction above the ordering temperature $T_2 = T_N$, suggesting the presence of short-range magnetically ordered diffraction domains. Since above T_1 = 420 K the compound is paramagnetic, the 420 K ÷ 288K magnetic behavior is ascribed to a confined G-type

antiferromagnetic spin arrangement involving solely the iron-rich clusters which display a weak ferromagnetic resultant, possibly due to an uncompensated magnetic moments or rather to a slight spin canting (DM interaction), and characterized by a very soft character.

At T_N the magnetic ordering process involves both Fe and Mn ions; here the Fe-O-Mn superexchange interaction sets in and long-range AFM is stabilized on the basis of a G-type structure, as determined by neutron diffraction analysis (subsection *III.C.2.2*). Despite this relatively simple picture, magnetometric measurements collected cooling down the system across T_2, revealed a spontaneous two-step transition with a thermally activated evolution. The first stage is characterized by a prompt increase of the magnetization just below T_2, pointing out a concordant arrangement with respect to that of the pre-existent internal magnetization. Such increase possibly depends on the ordering process of manganese ions just around iron-rich clusters (sub-2); such process is guided precisely by the internal field of iron-rich clusters. The second stage, showing slower dynamics, promotes a low-*T* state characterized by a competitive magnetization with respect to that of the iron clusters and a harder anisotropic character. Mössbauer analysis evidenced that this third magnetic population (sub-3), again characterized by weak ferromagnetic response due to spin canting or to the presence of uncompensated moments with resultant in the opposite direction, is the one responsible for MRV. Such magnetic component reasonably gathers all the clusters at high manganese content that for assumption get ordered at lower temperatures.

Noteworthy is that the observation of the reversal process is always related to the initial orientation at RT of the small resultant moment of the iron-rich clusters. As demonstrated by zero field ZFC characterization of section *III.D.3*, N-MRV and P-MRV are detected depending on the sign of RT iron rich clusters magnetization.

D.4 BFMO MRV field dependence

D.4.1 In-field magnetometric characterization

In this section the in-field magnetometric characterization on MRV is presented. For the sake of clarity, all the reported Zero Field-Cooling (ZFC) and Field-Cooling (FC) magnetization measurements were carried out by the standard procedure. In the ZFC measurement the system is cooled to 5 K with no applied magnetic field, then the selected field is switched on and magnetization is measured in warming. The FC measurement, that starts directly at the end of the ZFC measurement, is performed upon cooling in the same field. The isothermal magnetization data were collected with increasing fields starting from 0 Oe. Before each ZFC and isothermal magnetization measurement, the residual field of the magnet was properly cancelled (< 0.1 Oe).

As already described, ZFC curves in zero-field condition of Fig. III.28 demonstrated how spontaneous N-MRV or P-MRV can be observed simply depending on the positive or negative sign of weak ferromagnetic iron rich cluster magnetization at RT and so on the sample orientation with respect to the direction fixed as positive in the SQuID magnetometer.

Once ZFC-FC measurement is performed, the application of a positive magnetic field, even of few oersteds, changes dramatically the scenario and the induced modifications are completely different as far as N-MRV or P-MRV sample is concerned, as pointed out by Figs. III.32 (N-MRV sample) and III.33 (P-MRV sample).

N-MRV case

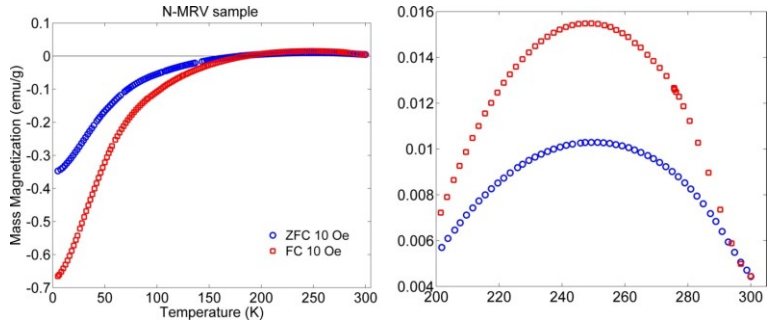

Figure III.32. ZFC-FC measurement collected in a field of 10 Oe between 5 K ÷ 300 K for a sample displaying spontaneous N-MRV. On the right, an enlarged view of the thermal region between T_3.

The ZFC curve (blue circles) show the expected trend observed in Fig. III.28. Neither $T_2 = T_N$ nor T_3, critical temperatures of the system, are affected by the field. The action of a 10 Oe positive field is pictured in the FC curve (red squares), providing an increase of the magnetization maximum value at T_3 (Fig. III.32(right-side)) and of the magnetization minimum negative value at 5 K (Fig. III.32(left-side)), with respect to the relative ZFC curve. The compensation temperature (defined as the temperature at which magnetization goes to zero) is equal to that of the ZFC case. In short, a 10 Oe positive field enhances the global magnetic response of N-MRV.

P-MRV case

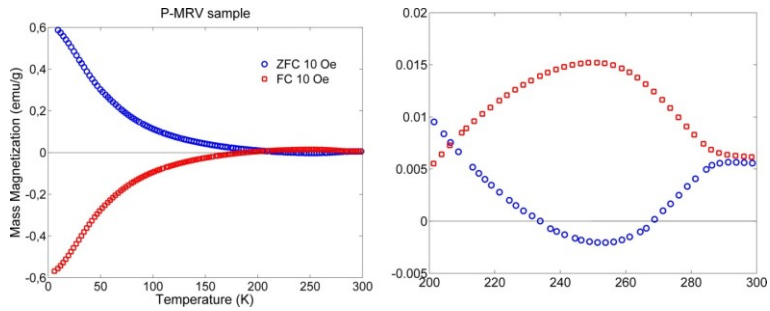

Figure III.33. ZFC-FC measurement collected with a field of 10 Oe between 5 K ÷ 300 K for a sample displaying spontaneous P-MRV. On the right an enlarged view of the thermal region between T_3.

More significant is the case of a P-MRV sample; where the action of a 10 Oe positive field is even substantial. When in fact the ZFC measurement starts, a positive magnetization is correctly detected at 5 K. However, as the system is warmed, the compensation temperature just occurs in proximity to T_3, where the minimum of the magnetization is reached, as can be seen in Fig. III.33(right-side). However differently for the P-MRV spontaneous magnetization reported in Fig. III.28, just above T_3 the magnetization goes back to positive values crossing $T_2 = T_N$. Above T_N the magnetic response is concordant to the field. This means that the iron clusters responsible for the RT magnetism are polarized and rotated by the field parallel to them. Therefore, when the FC measurement (red curve) is launched, the positive RT signal determines the N-MRV process and magnetization goes to a negative response as the system is cooled down (Fig. III.33(left-side)). As a result, the low-*T* part of the FC curve is symmetric to the corresponding part of the ZFC curve with respect to the zero magnetization axis.

This description may not appear so surprising, but it truly hides a very important outcome. At least for BFMO, every FC performed with a weak positive field shows N-MRV although the sample is in a spontaneous N- or P-MRV; consequently N-MRV is the positive field-favored magnetic response.

For these reasons a wide set of such measurements is presented in the following in order to describe how magnetization reversal depends on the external field intensity. Since it is a thermal activated mechanism, the analysis is based on ZFC-FC characterization. This study is performed on a sample characterized by a spontaneous P-MRV. This choice was made because P-MRV is the unfavorable state of the sample in the common magnetometric condition of positive applied field, giving me the opportunity to investigate all the magnetic criticalities of the compound (the N-MRV behavior is a simplification of the P-MRV one and so it was not treated).

During the measurement sequence, the sample was not removed from the SQuID apparatus. Between one ZFC-FC cycle and the following one, the sample was warmed up to 350 K or 380 K and the magnetization was checked to be negative in order to verify the invariance of initial conditions.

D.4.2 The external magnetic field effect on P-MRV

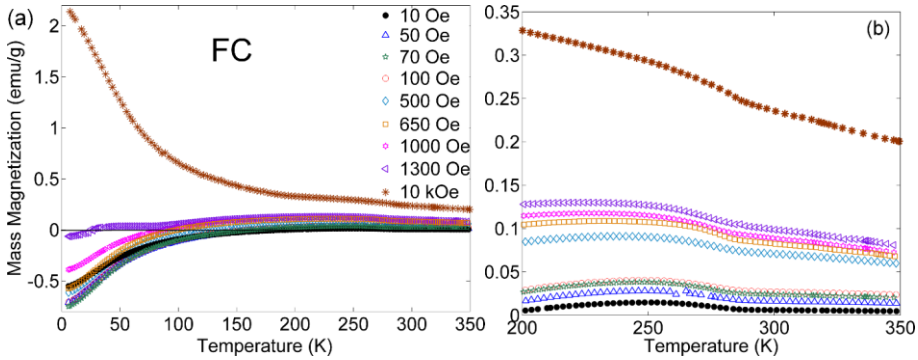

Figure III.34. (a) FC magnetization measurements as a function of temperature collected with different applied magnetic fields. (b) Enlarged view of the region between 200 K and 350 K. *[image taken from Ref. 22].*

Figure III.34 reports on the FC magnetization measurements collected at different applied magnetic fields for a sample showing spontaneous P-MRV. Such measurements are all characterized by an change of concavity in correspondence to T_2 = 288 K, the Neél temperature of the system. It can be noticed that all FC curves, except that at 10 kOe, display N-MRV once the system is cooled down, independently from the initial orientation of the sample (and hence from the RT spontaneous magnetization).

These measurements confirm that it is the sign of magnetization at RT (always positive, see Fig. III.34b) to drive the sign at 5 K (negative), as previously verified. Moreover, they put in evidence the strong influence of the field intensity on the MRV behavior. In particular, two key points have to be underlined:

- the modulus of magnetization at 5 K (at the end of FC curves) increases with the field up to 70 Oe and then it decreases tending to zero at about 1300 Oe ÷ 1400 Oe, causing a corresponding decreasing of the compensation temperature T_{comp};

- for a field larger than 1300 Oe ÷ 1400 Oe the MRV no longer occurs in the FC curve.

It is worth noting that a best-fit of the magnetic field dependence of T_{comp} reported in Fig. III.35 (iso-magnetization curve) shows an inflection point at about 650 Oe. Specifically, T_{comp} decreases as H is increased and it can be interpolated by means of a cubic binomial of Eq. III.5:

$$T_{comp} = k_1 + k_2(H - H_0)^3, \qquad \text{(III.5)}$$

where $k_1 = 106\ K$, $k_2 = -3.02 \cdot 10^{-7}\ K/Oe^3$ are the best fitting parameters and $H_0 = 655\ Oe$ the inflection point. This trend is quite unusual since the sign invariance of the second derivative should be reasonably expected in absence of a significant change of the magnetic properties. However it should be noted that H_0 is very close to the value of H_1 = 650 Oe.

I will consider hereafter H_1 as a singular field of the system, which marks the occurrence of a continuous phase transition. It corresponds indeed to a change of concavity of both the isotherm at 5 K (Fig. III.12 in subsection *III.C.3.2*) and the iso-magnetization curve at M = 0 (Fig. III.35). The same remarks apply also for the second singular field H_2, determined by the isothermal characterization too, which defines the onset of an antiferromagnetic behavior for the FC magnetization.

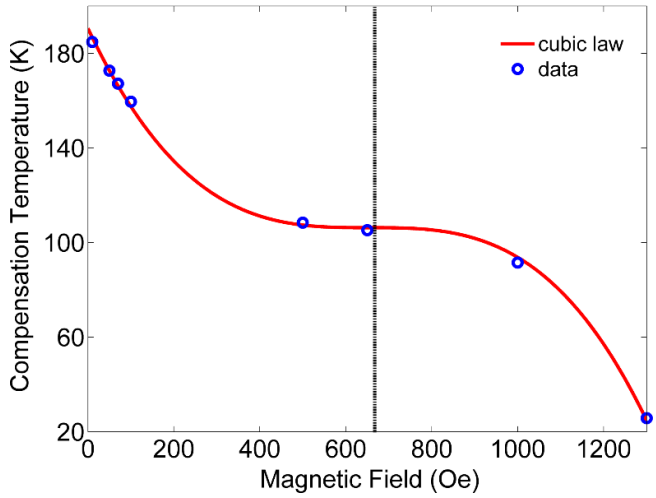

Figure III.35. Iso-magnetization at M = 0. The evolution of the compensation temperature, collected for each FC curves of Fig. III.34, is plotted as a function of the applied magnetic field; the trend is fitted by a cubic binomial red line (see Eq. III.5);vertical line marks the inflection point. *[image taken from Ref. 22].*

Therefore, a reliable description of the magnetic properties of BFMO (and similar systems) requires a systematic collection of magnetization iso-fields measurements in three different field regions: $H < H_1$, $H_1 < H < H_2$ and $H > H_2$.

Regime $H < H_1$

For H = 100 Oe the ZFC-FC curves show the same qualitative behavior with respect to the same characterization at H = 10 Oe, plotted in Fig. III.33; precisely P-MRV is detected in the ZFC, while N-MRV is observed in the FC (see Fig. III.36a).The ZFC curves show a clear minimum at about T_3 = 250 K, just the opposite happens for the FC curves. However, differently from the effect at 10 Oe of ZFC curve of Fig. III.33, a field of 100 Oe applied during the warming process is sufficient to completely reverse the ZFC magnetization at high temperature, without the occurrence of a sign reversal (Fig. III.36b), pointing out once again the soft magnetic character of the compound, at least in these temperature and field conditions, together with the weak ferromagnetic nature of the iron-rich clusters component.

A further point to be noticed is that the measurements at 100 Oe show a strong reduction of the magnetic susceptibility over the whole temperature range with respect to the 10 Oe ones.

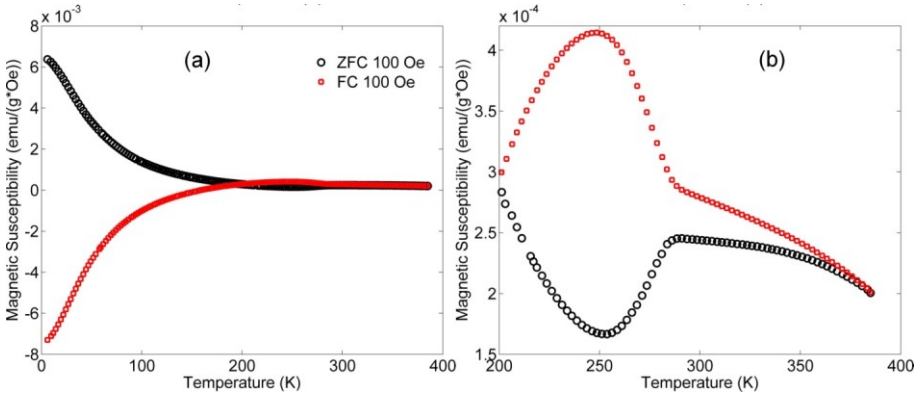

Figure III.36. (a) ZFC and FC curves measured at H =100 Oe; (b) is zoomed graph. *[image taken from Ref. 22].*

Regime $H_1 < H < H_2$

Applied fields larger than H_1 strongly affect the overall behavior of the compound. In this case, it displays N-MRV directly in the ZFC curve even if the sample is mounted with spontaneous P-MRV, (see Fig. III.37), due to the action of the 1 kOe magnetic field switched on at 5 K. The disappearance of P-MRV is related to the absence of the minimum observed for lower applied fields at T_3, indicating that applied fields higher than H_1 hide the occurrence of the competition which is the basis of MRV. The fact that a relatively low field is enough to flip the 5 K magnetization of the system suggests that the nature of the involved interactions cannot be explained using a simple superexchange-mediated model and it should rather be related to the coexistence and a competition of two different weak ferromagnetic components. This indication follows from the observation of a "soft" and a "hard" component in the M(H) loops at 5K in Fig. III.13 of subsection *III.C.3.3*, with coercive fields close to H_1 and H_2, i.e. the two singular fields deduced from the presented magnetometric analyses. The two components are due to the intrinsic inhomogeneity of Fe

and Mn in BFMO, which gives rise as mentioned to mesoscopic regions of the sample (clusters) richer in Fe or in Mn.

It is worth to stress that in this quite narrow field regime the magnetic behavior of the compound (showing MRV or antiferromagnetism) is rather uncertain, in that it depends on the degree of inhomogeneity of the specific sample and on the mean dimensions of the iron-rich clusters, both unpredictable consequences of the synthesis.

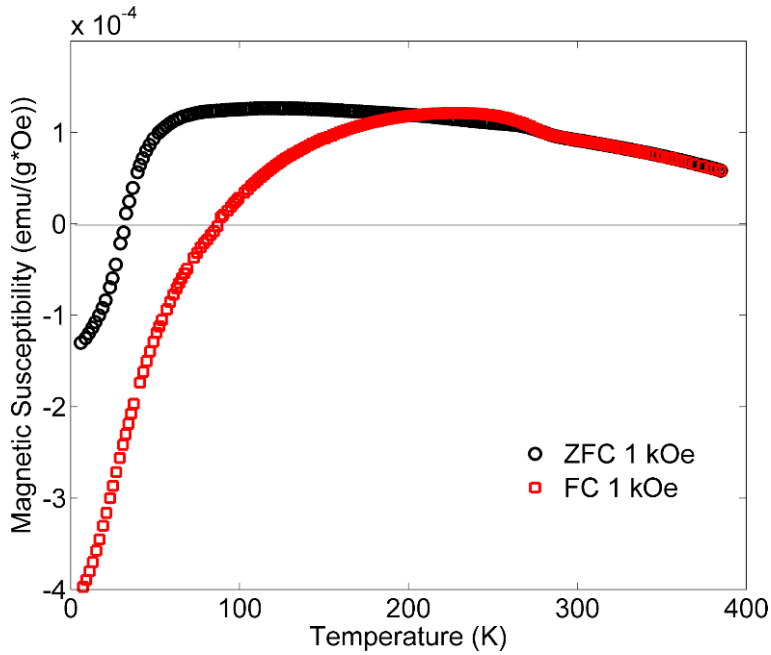

Figure III.37. ZFC and FC curves collected with applied magnetic field H = 1 kOe. *[image taken from Ref. 22].*

Regime $H > H_2$

The application of fields higher than H_2 yields a further change of the magnetic properties of the system, as reported in Fig. III.38.

Regardless of the initial state of the sample, both the ZFC and FC measurements result to be superimposed and positive in the whole investigated thermal range. The interactions

responsible for MRV turn out to be completely overwhelmed by the effect of the applied field, and the highlighted behavior below T_N is characteristic of a compensated antiferromagnetic system in high-field conditions, in agreement with neutron diffraction data. Thus, the weak ferromagnetism observed in BFMO, which is related to the intrinsic disordered nature of the transition metals at the perovskite B site, shall be considered as a perturbation superimposed to an overall antiferromagnetic behavior, as previously well described.

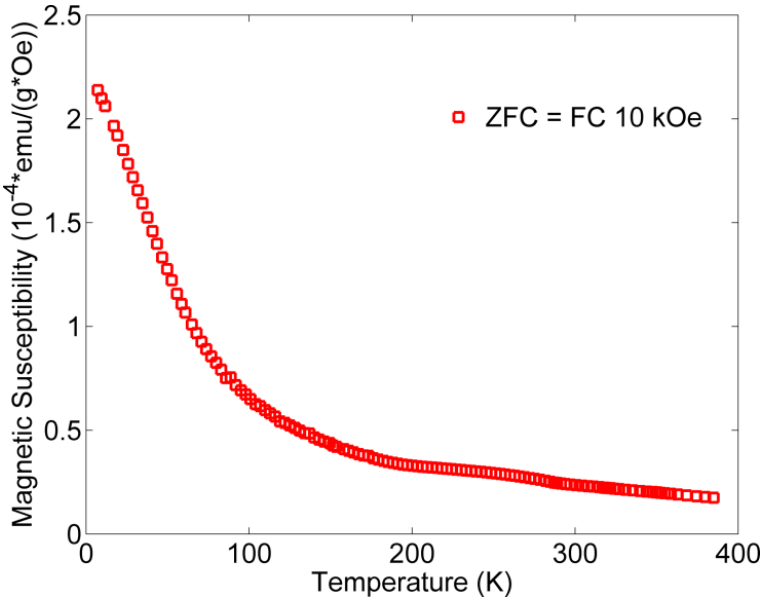

Figure III.38. ZFC and FC curves collected with 10 kOe external magnetic field. *[image taken from Ref. 22].*

The complex phenomenology of MRV resulting from the application of the above-described measurement protocol is summarized in Table III.4. The evolution of the magnetization sign is there gathered in terms of applied field as a function of the thermal range involving the three critical temperatures. The table reports, going from left to right, the expected sign of the magnetization during the standard ZFC-FC measurement cycle.

Table III.4. Magnetization sign dependence of a ZFC-FC measurement performed in the 5-350 K range for different applied fields. For each field regime both the cases of spontaneous N-MRV and P-MRV are reported in rows, above and below respectively. [table taken from Ref. 22].

Temp. ranges / Applied Field (Oe)	ZFC				FC			
	5 K	below T_3	between T_3 and T_2	between T_2 and T_1	between T_1 and T_2	between T_2 and T_3	below T_3	**5 K**
H = 0	-	-	+	+	+	+	-	-
	+	+	-	-	-	-	+	+
$H < H_1$	-	-	+	+	+	+	-	-
	+	+	-/+[a]	+	+	+	-	-
$H_1 < H < H_2$	-/+[b]	-/+[b]	+	+	+	+	-/+[b]	-/+[b]
	-/+[b]	-/+[b]	+	+	+	+	-/+[b]	-/+[b]
$H > H_2$	+	+	+	+	+	+	+	+
	+	+	+	+	+	+	+	+

[a] Negative or positive sign is observed for fields smaller or higher than the minimum field for which the MRV is no longer present in FC collected starting from $T < T_N$ (this result is reported as supplementary data of Ref. 11).
[b] Negative or positive sign is observed for fields smaller or higher than compensation field respectively.

D.4.3 In-field Mössbauer characterization

Figs. III.39a-b-c show the comparison of in-field and zero-field Mössbauer spectra collected at three relevant temperatures (300 K, 285 K and 250 K). The spectra consist of two contributions: the first is due to Fe-rich clusters and is characterized by hyperfine fields similar to those of $BiFeO_3$. The second contribution, due to the remaining part of the compound in the investigated temperature range (constituted by the statistically predominant Fe-Mn clusters but also by Mn-Mn clusters with a low concentration of iron), is the super-paramagnetic (SP) sub-spectrum, composed of a doublet-like structure and low field magnetically ordered components.

The thermal evolution of the spectrum line shape consists in the collapse of the SP doublet-like structure into the SP low field component, already observed in the zero-field spectra described in section *III.D.3*. The application of the external field just determines a reduction of the absorption at *(–4, –3) mm/s* and *(3, 4) mm/s*, i.e. in the velocity ranges corresponding

to the intermediate lines of the sextet with the highest field. This reduction, well observable at RT and less visible at lower temperatures, can be explained either assuming that the external magnetic field strongly affects the distribution of the hyperfine inner fields or with a polarization of the highest field part of the material due to the orientation of the corresponding magnetic moments along the applied field direction. For the reasons reported below, I opt for the latter explanation, although this could seem to disagree with the AFM nature of the compound. In fact, if the external field interaction is high enough to overcome the anisotropy barrier, it should give rise to the so-called spin-flop process and consequently to an increase of the absorption in the cited velocity ranges. On the contrary, if the anisotropy interaction predominated, the line shape should not change significantly [53].

The main feature of the spectra, i.e. the exponential decrease of the SP doublet-like component on decreasing temperature, is typical of AFM nanoparticles with uniaxial magnetic anisotropy [54]. The fact that this feature is not accompanied by a conventional line broadening at intermediate temperatures may also suggest the presence of quantum effects [55] similar to the ones characterizing AFM molecular nanoclusters [56]. In $BiFe_{0.5}Mn_{0.5}O_3$, the inhomogeneity is responsible for the presence of distinct magnetically active mesoscopic clusters with different Fe^{3+} and Mn^{3+} concentrations; such clusters may be assimilated to a sort of weak of interacting "*nanoparticles*" nestled in the solid solution.

The fitting procedure of the spectra line shape, following the scheme adopted in Ref. 11, was based on the superposition of the two contribution cited above. Therefore, I chose to express the Mössbauer cross-section $\sigma_M(E)$ by the sum of seven Voigt sextets following a standard procedure applied in the case of hyperfine field distribution [57]. One of the Voigt sextets (sub-1) describes the component that is magnetically ordered in the whole thermal range, i.e. the highest field contribution, which the external lines of the spectrum are mainly due to. Four sextets (sub-2 ÷ sub-5) deal with the low-energy levels of the SP Fe-Mn clusters characterized by a non-null mean magnetic moment. Finally, the last two sextets (sub-6 and sub-7) reproduce the inner doublet-like structure due to the high-energy levels of the same clusters. The high quality of the fits of both in-field and zero-field spectra at all the temperatures ($980 \leq \chi^2 \leq 1075$) indicates that the estimated Mössbauer cross-sections are good enough to be compared each other temperature by temperature.

Fig. III.39d shows the residual contribution of the Fe-Mn clusters at 270 K, due only to their low-energy levels, i.e. without the super-paramagnetic (SP) doublet-like part.

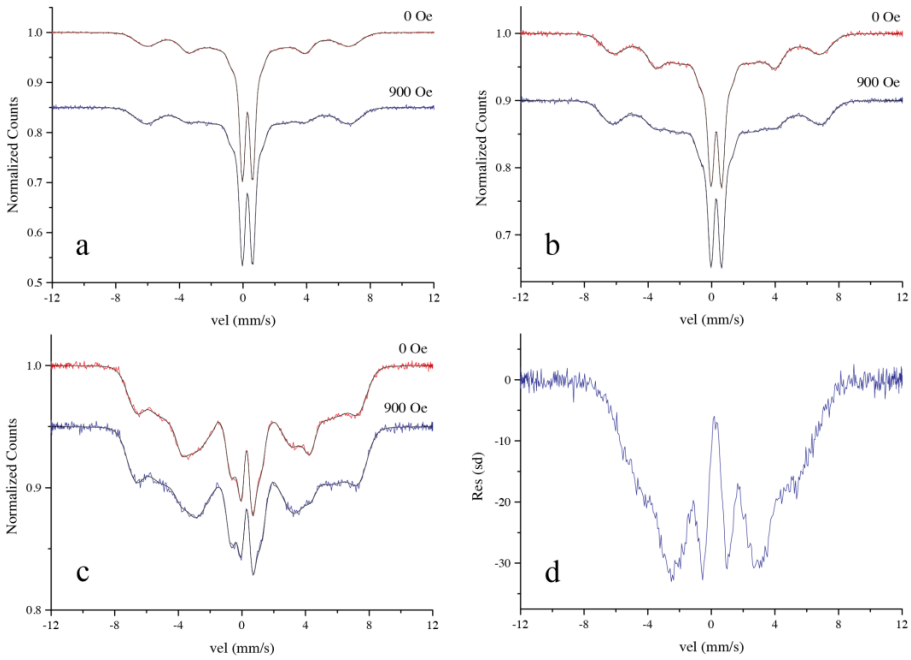

Figure III.39. (a), (b), (c): Comparison between Mössbauer absorption spectra collected at 300 K, 285 K and 250 K with and without external field. (d): Residual counts in standard deviation units at 270 K, obtained by subtracting the contributions due to the sub-1 component and to the SP doublet-like structure from the whole spectrum. *[image taken from Ref. 22].*

Figure III.40 illustrates the differences of the $\sigma_M(E)$ values obtained with and without applied field at 300 K and 250 K. For what concerns the sub-1 component, one observes similar wells corresponding to the positions of the external and internal lines of the highest field component and peaks corresponding to the two intermediate lines of the same component. This feature, revealed in the entire investigated temperature range, is a fingerprint of the polarization effect of the sub-1 component, introduced above. Moreover, the independency of the sub-1 percentage contribution from the field application, a condition resulting from the fixed dimension of the Fe-rich clusters, can be obtained only by

excluding random orientation. This implies that the absorption reduction at *(–4, –3) mm/s* and *(3, 4) mm/s* is due to a polarization effect of the highest field component. In the temperature range (275 K, 300 K) the texture parameter, defined as the ratio between the intensities of intermediate and inner lines, results to be about *0.8*, corresponding to an easy-plane magnetic ordering similar to the one of the parent compound $BiFeO_3$. By lowering *T* below 275 K, it increases up to *~1.4* at 245 K. It is worthy to note that the values obtained for the texture parameter of sub-1 are not in disagreement with the AFM nature of the interactions, among the metal ions. The clusters of AFM-coupled spins are indeed expected to show uncompensated moments, which can be localized both on the surface of the clusters and inside them as a consequence of Mn-Fe substitutions.

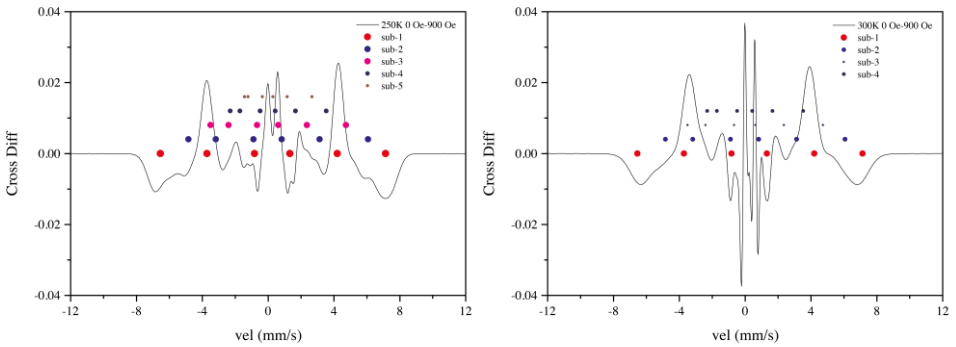

Figure III.40. Plots of the difference between the zero field and applied field cross-sections at 250 K (left-side) and 300 K (right-side). The coloured dots stay for the position of the sextets lines and their areas are proportional to the corresponding contributions to the sample thickness. *[image taken from Ref. 22]*.

Figure III.40 shows also the effects of the applied field on the remaining part of the spectrum components (i.e. those related to the Fe-Mn clusters containing Mn and Fe ions according to the ratio $1/(1- t_1) \approx 1.2$, where t_1 is the relative thickness of sub-1). I note the presence of dips at the line positions of the sub-2 components (blue dots), whose depth increases by decreasing T because of the increase of the ground state thermal population in clusters characterized by uncompensated magnetic moment. Moreover, the applied field

affects the spin dynamics of the high-energy states and, consequently, the shape of the SP doublet-like contribution changes, giving rise to a sequence of sharp peaks and deep wells in the velocity range corresponding to the sub-6 and sub-7 components.

The SP contribution to $\sigma_M(E)$ is characterized by a texture parameter value of *2*, typical of randomly oriented magnetic moments. However, this value could also be obtained in the case of magnetically ordered structures belonging to powdered compounds characterized by axial anisotropy. The latter situation is just what one expects, on the basis of the long range ordered magnetic structure determined by neutron diffraction, which indicates a spin alignment along the crystallographic *a* axis. For what concerns the quadrupolar splitting value and the angle between the hyperfine field and the quantization EFG principal axis *z*, the fitting procedure returned values near $\Delta Q_S = 0.65\ mm/s$ and $\beta = 0.77\ rad$ in the whole temperature range independently of the application of an external magnetic field. An estimation of the lattice contribution to the EFG tensor was carried out to verify the agreement of the Mössbauer spectroscopy results with the crystallographic data and with the spin alignment along the crystallographic *a* axis resulting from the powder neutron-diffraction experiments. Therefore, the orientation of the easy axis extracted from the Mössbauer spectra can agree with the atomic moment direction derived from powder neutron-diffraction data.

In-field and zero-field Mössbauer measurements reveal the presence in the material of two components with different magnetic properties. One of them, consisting of iron-rich clusters, contains 20% of the total iron in the compound and shows soft magnetism since it can be strongly polarized just by a weak applied field. The other component belongs to 80% of the total iron, corresponding to 80% of the magnetic interactions, and is characterized by an easy-axis anisotropy and by a thermodynamic equilibrium between the occupation probabilities of the low energy states localized inside the anisotropy barrier and the high-energy states with null mean magnetic moment, localized over the barrier. Since the low energy states with a non-null mean magnetic moment are connected by transitions involving the high-energy states in the second perturbation order, a high population of the levels over the barrier forces the magnetic character of the compound to be soft. By decreasing T, the population of these high levels decreases exponentially and consequently the magnetic

character of this component becomes harder and harder. Therefore, as shown in Fig. III.12, the isotherm at 5 K evidences the superposition of two different phases with very low (iron-rich clusters) and high coercivity (Fe-Mn clusters); this hypothesis is further confirmed by the opening at low temperatures of a kinked hysteresis loop, as reported in Fig. III.13.

The thermal trend of the total absorber effective thickness under 250 K shows an unexpected strong deviation from the characteristic temperature dependency usually well described by the Debye model (see Fig. III.41). This behavior indicates the presence of low-temperature anharmonicity in the adiabatic potential of the Mössbauer ion and was detected in several compounds [58], including high-T_c superconductors [59] and ferroelectrics [60]. By applying the method of analysis described in [61,62], a flat region of *0.1 Å* in the adiabatic potential is derived from the temperature dependency of the mean square displacement of the Mössbauer ion.

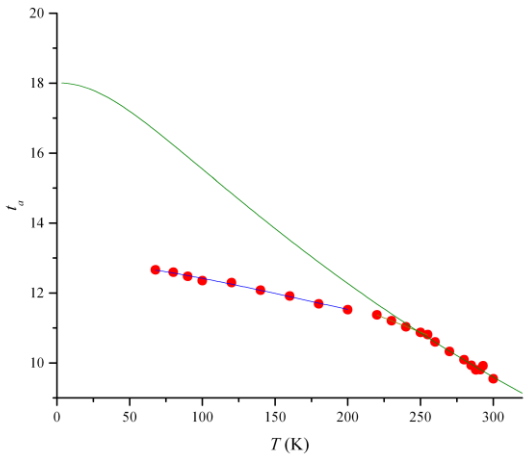

Figure III.41. The thermal trend of the total effective thickness of the absorber is illustrated: the green line represents the expected dependency on the basis of the Debye model, whose zero intercept is in agreement with the amount of active material in the sample. *[image taken from Ref. 22]*.

D.5 Conclusions on MRV mechanism in BFMO

A specific set of magnetometric measurements together with zero-field and in-field Mössbauer spectroscopy have been performed in order to understand the complex mechanism responsible for the thermal activated field dependent MRV in bulk polycrystalline $BiFe_{0.5}Mn_{0.5}O_3$. The B site cation disorder displayed by this double perovskite structure gives rise to clusters with different iron and manganese concentrations, showing inhomogeneous magnetic properties. Below T_1= 420 K the iron-rich clusters get ordered, while at $T_2 = T_N$ = 288 K an antiferromagnetic long-range transition occurs, corresponding to a global AFM G-type magnetic structure. Mössbauer spectroscopy indicates that above T_N all the magnetic components of the material, specifically the iron-rich clusters, are characterized by a very soft/superparamagnetic-like behavior. The MRV process is a secondary but spontaneous magnetic effect superimposed to the long-range antiferromagnetism and due to the competitive arrangement of cluster clusters characterized by uncompensated moments. The magnetic characterizations reflect this complex situation, giving different results depending on the applied field intensity, on the sample thermal history and on its orientation with respect to the measurement system. The intrinsic sign of MRV in $BiFe_{0.5}Mn_{0.5}O_3$ can be individuated by means of zero-field ZFC measurements: in such a case P-MRV and N-MRV, with respect to the positive direction fixed by the measurement equipment, are observed at low temperatures depending only on the direction of the room temperature ($> T_N$) resultant magnetization. The isothermal measurements allowed to individuate two distinct singular fields, H_1 = 650 Oe and H_2= 2.2 kOe, which mark the onset of different magnetic contributions.

For an applied field larger than H_2 the interactions responsible for MRV are gradually cancelled and the behavior becomes that of a typical compensated antiferromagnet. On the contrary, for fields lower than H_1, the system displays MRV, with a different appearance of ZFC measurements depending only on whether the sample is in its spontaneous P-MRV or N-MRV state. In parallel all FC measurements with an weak external field $< H_1$ show N-MRV, even for a sample in the spontaneous P-MRV state.

In the intermediate regime $H_1 < H < H_2$, the energy of the interaction between the two magnetic components becomes comparable to the Zeeman energy of the system under field

application. Therefore, the singular temperature T_3 (as the marker of the competition) disappears and the thermal evolution of the system becomes unpredictable as the system is cooled below T_2. This means that MRV can be seen or not depending on the particular measured sample and on the specific degree of inhomogeneity. Mössbauer spectroscopy carried out in zero field and in a field of 900 Oe reveals that the presence of an external field affects in different ways the distinct magnetic components of the system. $H_1 < 900$ Oe $< H_2$ applied field compared with zero field Mössbauer spectroscopy reveals the presence in the material of two components with different magnetic properties. One of them, i.e. that associated to the iron-rich clusters, is characterized by an easy-plane magnetic anisotropy and it shows soft magnetism. The remnant part of the material is characterized by an easy-axis anisotropy and by a thermodynamic equilibrium between the populations of the low-energy states localized inside the anisotropy barrier and the high-energy states localized over the barrier. Therefore, the magnetic character of this part changes from soft to hard by decreasing *T*. Such magnetic phase hardening entails a gradual cancellation of the competition on the basis of MRV process this means that the orientation of Fe-Mn clusters magnetic resultant is no more affected by the weak interaction with the iron-rich clusters and evolves independently following the external magnetic field.

Moreover, the analysis of absorber recoilless factor shows that, below 250 K, low-*T* anharmonicity sets in the adiabatic potential, justifying the observation of ferroelectric properties, as reported in section *III.C.5*.

In conclusion, the gathered data indicate that structural inhomogeneity and cationic disorder in $BiFe_{0.5}Mn_{0.5}O_3$ are directly responsible for the intrinsic MRV process embroidered on an AFM character. The interactions at the origin of MRV, corresponding to regions of the sample characterized by variable concentrations of iron and manganese, respond in different ways to the application of an external field. As a consequence, a complex phenomenology is detected, requiring great caution while performing magnetic characterizations: the entity of the applied field, the measurement protocol together with the chosen thermal intervals and the sample initial conditions are fundamental variables for a reliable study of compounds showing inhomogeneity-related MRV.

E. Pb_2FeMoO_6 (PBFMO), a HP/HT Pb-based Double Perovskite

As formerly introduced in subchapter *III.B,* another way to produce lone-pair driven multiferroics materials, consists in substituting Pb^{2+} instead of Bi^{3+} on the A-site of perovskite structure. In this case, the presence of a smaller oxidation state on the A-site allows to expand the number of possible magnetic ions on the B-site. For instance high oxidation state ions of the IV or V period (as Mo, Nb, W, Re etc.) can be mixed with a III period metal cation in order to obtain a double perovskite in close analogy to Bi-based perovskites. The advantage of Pb-based perovskites is the chance to yield compositional order on the B-site and consequently to simplify the magnetic character or the material. In fact, III-IV(or V) combinations often lead to strong magnetic response, but they are also responsible for high conductive behavior, which competes with the occurrence of ferroelectricity, in close linking to what observed in the parent family of the strontium based perovskites reported in subchapter *III.A*.

Three different compounds belonging to the class of Pb-based double were synthesized during the Ph.D activity. However, in the contest of this discussion, I chose to list just two of them because they are intimately correlated materials.

The first one, obtained in early 2013, was Pb_2FeMoO_6 (PBFMO). In this compound, as the reader could appreciate in the following, the Mo ion shows an unusual valence number of 5+. The stabilization of this oxidation state in octahedral coordination needs the fundamental engagement of high pressure synthesis techniques. Since the first preliminary structural and magnetic characterization, PBFMO displays intriguing perspectives, above all a ferromagnetic-like response just below RT.

In spite of such positive outcomes and accordingly to what already predicted, PBFMO unfortunately revealed an important drawback: i.e., high conductance in the entire thermal range. In the rush towards multiferroism, this represents an insurmountable obstacle. In front of such a intrinsic hindrance, I had to come back retracing my steps. Once again the solution was found within the incredible tolerance of the perovksite structure.

To decrease the conductive character I had to reduce the number of free electrons, which is usually promoted by metallic cations on the B-site and their d^n external shells, principally whenever the shell is occupied by unpaired electrons. In the present case on the B-site are located Fe^{3+} and Mo^{5+}ions with electronic configuration d^5 and d^1, respectively. Since the iron shell is quite inactive due to the half occupancy, the sole electron of molybdenum can be easily delocalized by a jump in the conduction band. Therefore, the only way to decrease conductivity goes through an enhancement of the molybdenum oxidation state. To force such higher oxidation state ion on the structure I had to lower the electric charge in another crystallographic position, i.e., on the A site. Consequently, I made a partial substitution with a less oxidized ion with respect to Pb^{2+}, namely with the alkaline cation potassium since it owns a similar steric hindrance.

I succeeded in this goal just at the end of 2013, when $KPbFeMoO_6$ was finally synthesized in very extreme pressure conditions (9 GPa), after a large number of failed attempts.

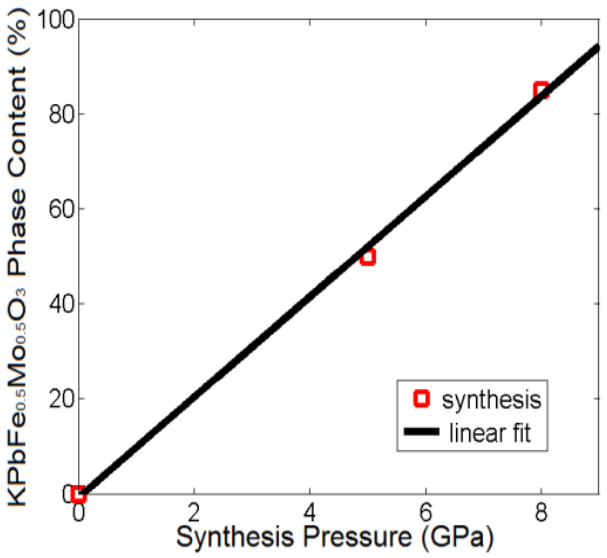

Figure III.42. The percent content of the $KPbFeMoO_6$ double perovskite in the final product of a HP/HT synthesis as a function of the applied pressure. The point distribution evidences a linear dependence vs P, and states the impossibility to produce such compound in standard condition.

This compound correctly displayed a dielectric behavior, thus resulting a good and novel candidate to multiferroism. Preliminary evaluations confirmed that in $KPbFeMoO_6$, molybdenum seems to be in the expected oxidation state +6.

Reached this point of the discussion, it was quite tough for me to decide the way to proceed. Initially I thought that it would have been better to describe PBFMO and $KPbFeMoO_6$ separately in two different sections or rather treating them together in one by elaborating a detailed comparison for each step of characterization. However now I am sure that these two options were both wrong. The amount of written pages has quickly increased and I am aware that it is extremely important to give the reader the idea of how many different properties and materials I was able to characterize. In fact, during the last three years, the time investment in installing instruments for characterization is almost equal to the time spent to synthesize and to analyze my multiferroics. For this reason I chose to write just about PBFMO that, instead of being a multiferroic magnetoelectric, it is a complex compound which hides important different multifunctionalities. I hope that this decision can be sincerely supported.

E.1 Synthesis of PBFMO

PFMO was successfully obtained at 5 GPa and 950 °C after 1 h of reaction; then the system was abruptly quenched to room temperature before the pressure was slowly released [63]. The samples form is prevalently polycrystalline, characterized by a single crystal mean dimension lower than 40 μm. The mean sample purity, in these thermodynamic conditions, reaches about 100%, with non-appreciable contaminating phases (less than 1%). Preliminary powder XRD diffraction experiments reveal that PBFMO crystallizes in a pseudocubic structure with lattice parameters in line with those of quadruple perovksite $a'=2a_p$ = 7.968 Å. These results suggest a high symmetry incompatible with the occurrence of ferroelectricity.

E.2 Space and Time-Structure of PBFMO

E.2.1 Space Symmetry (Electricity)

Single crystal XRD experiments were performed on different samples and confirmed the results obtained also in a previous work [64].The TEM diffraction images reported in Fig. III.43 show the presence of superstructure spots, requiring the doubling of the simple perovskite axes in all the directions. Therefore, all the observed reflections can be indexed in a pseudocubic cell with lattice parameter $a'=2a_p$. In addition the $h+k,\ k+l,\ h+l=2n$ extinction condition is detected, implying F-centering of the lattice.

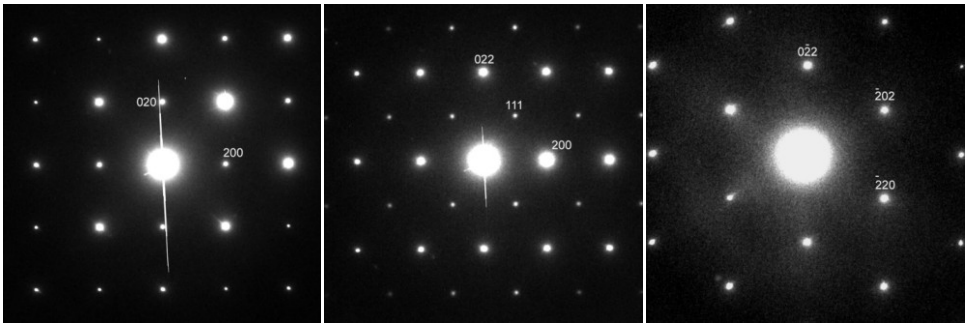

Figure III.43. TEM diffraction images taken in the [001], [01-1], [111] (left to right) zone axes. The reflections are indexed on the basis of the supercell with $a'=2a_p$.

The simultaneous use of synchrotron and time of flight (TOF) neutron data allowed the accurate refinement of the RT crystal structure of Pb_2FeMoO_6. No deviation from the cubic symmetry was detected, and therefore, according to electron diffraction, the *Fm-3m* space group was used in the refinement with cell parameter $a = 7.968$ Å; weak satellite reflections are indeed detected in both the synchrotron and neutron data. The F-centering suggests the possible presence of cation ordering, thus the occupation of the B-site was initially set to a Fe/Mo ratio equal to 1, and freely refined in order to evaluate the degree of cationic order. Rietveld plot corresponding to the synchrotron data is shown in Fig. III.44, while the refined parameters and crystallographic data are gathered in Table III.5. A representation of the crystal structure of PBFMO is shown in Fig. III.45.

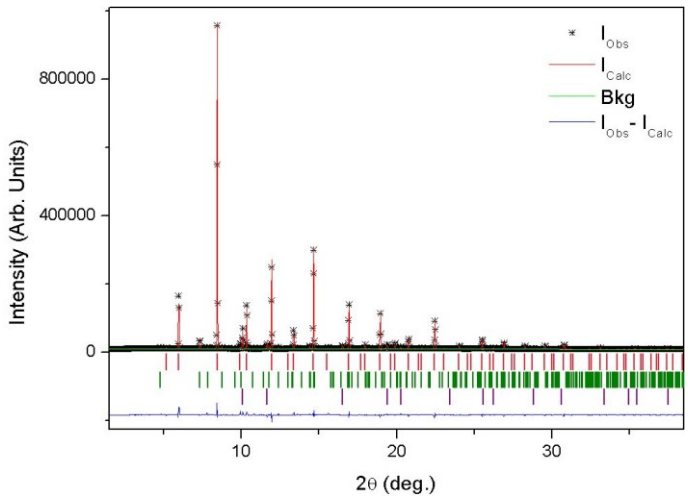

Figure III.44. Rietveld plot of the synchrotron diffraction pattern collected at 310 K synchrotron, showing a good accordance between the experimental spectra and that calculated on the basis of the refinement.

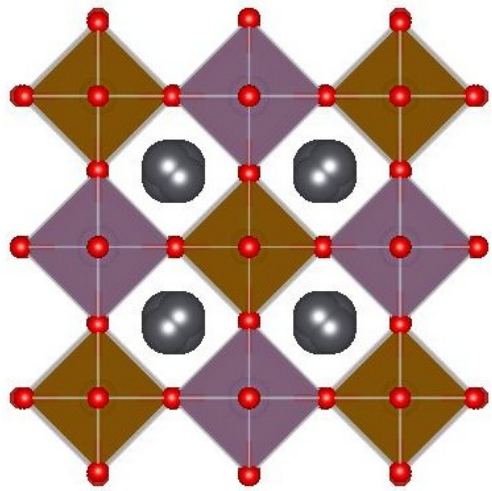

Figure III.45. Calculated crystallographic structure through the Rietveld analysis plotted in Fig. III.44.

Rock salt-like cation ordering is detected, both the B-sites being characterized by a 80/20% occupation, thus involving the presence of anti-site defects. Hereinafter the two sites will be indicated as Fe1 and Mo1, corresponding to the species with major occupancy within each site. It should be noticed that the *Fm-3m* space group involves high symmetry, not allowing the tilt or rotation of the TMO_6 coordination octahedra nor polyhedral distortions (as for example Jahn-Teller effect or ion off-centering), however different TM-O bond distances are permitted, according to the presence of (partial) cation ordering.

Table III.5. Crystal data and refined parameters.

Pb_2FeMoO_6 310K

Space Group: (225) Fm-3m

Lattice Parameters: a = b = c = 7.96609(4) Å

Volume = 505.516(7) $Å^3$ (Z=1)

Density = 8.701 g/cm^3

Atom (site)	X	Y	Z	s.o.f.	$U_{iso}(Å^2)$
PB1	0.22963(17)	0.22963(17)	0.22963(17)	0.25	0.0081(6)
FE1	0	0	0	0.780(9)	0.0074(2)
MO1	0	0	0	0.780(9)	0.0074(2)
FE2	½	½	½	0.220(9)	0.0074(2)
MO2	½	½	½	0.220(9)	0.0074(2)
O1	0.7493(3)	0	0	1	0.0127(3)

Number of reflections = 386

Number of parameters = 33

Refinement (F^2) = 0.0860

Rp = 0.0922

wRp = 0.1309

The Fe1-O bond length is *2.003 Å*, while Mo1-O one is *1.983 Å*, suggesting the presence of Fe^{3+} and Mo^{5+} within the structure. Noteworthy, local distortion of the Pb environment is detected. Indeed, when refinements were carried out with the lead atoms at the (¼,¼,¼) position, anomalously large isotropic displacement parameters were observed, requiring the ions to be shifted out of the high symmetry position, with non-integer occupation, which yielded a normalization of the thermal parameters. This reveals the presence of a statistical displacement giving rise to shorter and longer Pb-O bonds in the *2.591÷ 3.054 Å* range, in line with the typical phenomenology of the Pb^{2+} ion, which, due to the stereochemical effect generated by the $6s^2$ lone pair, is known to induce off-centering, and, in some cases, ferroelectric properties.

E.2.2 Time symmetry (Magnetism)

The refinement of TOF data collected below room temperature allowed the thorough study of the evolution of both the nuclear and magnetic structures of Pb_2FeMoO_6. No structural phase transitions are observed, with the cubic symmetry persisting in the whole range explored (1.5 K ÷ 300 K), while no additional peaks with non-integer indices are detected. Just below RT the intensity of the [111] reflection increases sharply, suggesting the development of a magnetic structure with propagation vector *k = (0,0,0)*. Since the *Fm-3m* space group does not allow magnetism, a symmetry lowering is required in order to fit the magnetic signal. This is in agreement with the phenomenology of Sr_2FeMoO_6, where the onset of long-range magnetic interactions induces a cubic to tetragonal transition, which however is reported to involve also the nuclear structure; in the present case, as previously reported, no transition is detected involving the Bragg peaks, and thus just the magnetic structure is expected to have a lower symmetry. The highest symmetry compatible space group, namely *R-3m'*, was used for the refinements, yielding excellent results. The Fe1 and Mo1 atomic moments were refined independently, converging in an antiparallel arrangement with atomic moments 3.*8* μ_B and *0.8* μ_B, respectively. A sketch of the magnetic structure is reported in Fig. III.46.

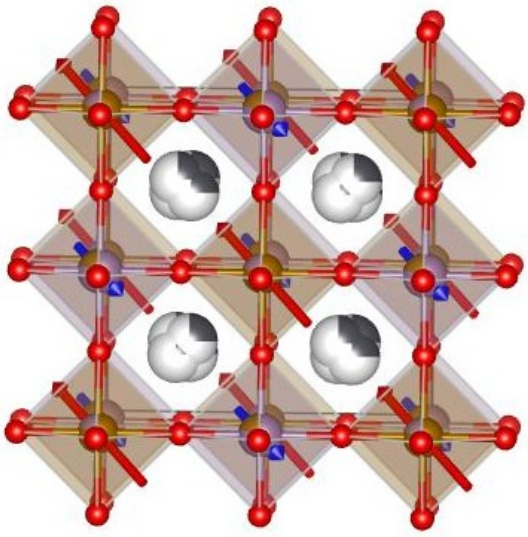

Figure III.46. Magnetic structure of PBFMO expressed on the basis of the *R-3m'* space group and revealing a ferrimagnetic arrangement of Fe^{3+} and Mo^{5+} spins.

The obtained values are not as expected for equal compositional Fe^{3+} and Mo^{5+} distributions (*5* μ_B and *1* μ_B, respectively), however the antisite fraction must be taken into account, whose contribution acts in introducing disorder, thus lowering the observed magnetic moments at both the TM sites. The thermal evolution of the atomic moments is reported in Fig. III.47, showing different behaviors for the two species. Between RT and 200 K indeed the Fe ions develop 80% of their moment, reaching saturation at about 60 K; on the other hand molybdenum shows a smoother increase of the magnetization, which is fully developed below 50 K.

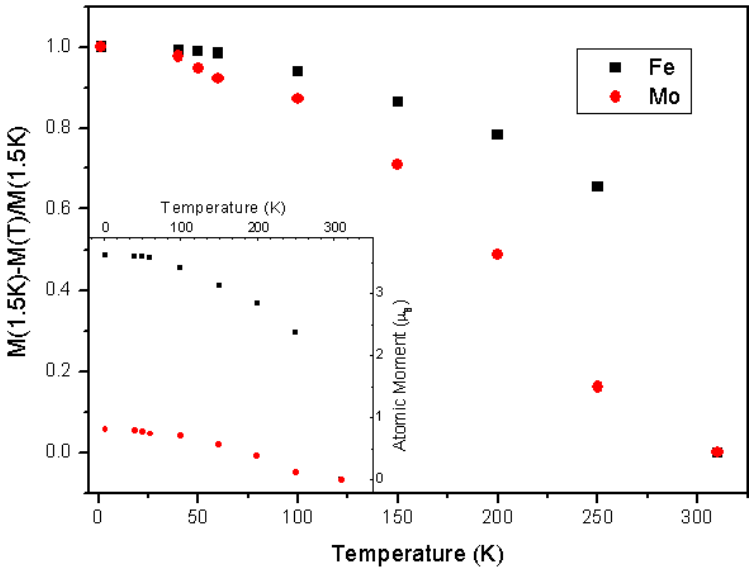

Figure III.47. Relative variation of the atomic moments of iron and molybdenum. Inset: absolute values expressed in Bohr magnetons.

As a result, the evolution of the ferrimagnetic resultant magnetization can be calculated as M(Fe1)-M(Mo1) (i.e., respectively the magnetic moments of the iron and molybdenum ions). The plot, shown in Fig. III.48, is characterized by a sharp increase right below room temperature ($T_N \approx 275$ K) and then by a stabilization of resultant magnetization below 60 K, as the system is cooled. Basing on these data, the expected saturation moment is about *2.8* μ_B.

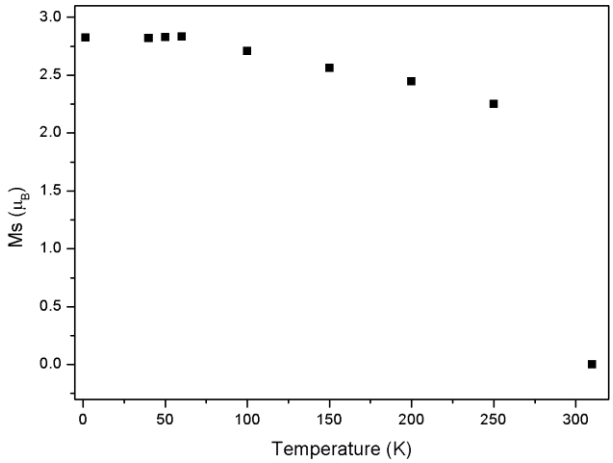

Figure III.48. Saturation magnetization for formula unit as obtained by refining of the neutron diffraction data.

The temperature-dependent neutron diffraction data allowed the study of the structural evolution between 1.5 K and 310 K. The cell volume dependence on temperature is shown in Fig. III.49. Below RT, as expected, the volume decreases with temperature, reaching however a minimum at about 100 K; below this temperature the system displays a negative expansion coefficient with a cell increase down to 50 K, where the volume stabilizes at an almost temperature-independent value. In addition, an anomaly was observed in proximity to the magnetic transition, with a sharp reduction of the volume once the superexchange interaction sets in, suggesting the presence of a weak spin-lattice coupling.

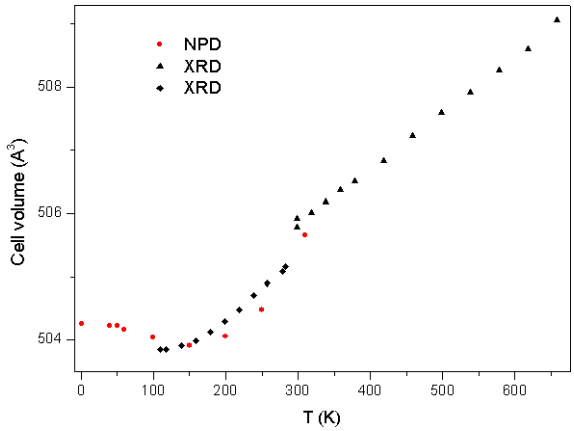

Figure III.49. Cell volume vs. temperature plots calculated by neutron diffraction data (red dots) between 300 K and 1.5 K, and by X-Ray diffraction between 680 K and 300 K /black triangles) and between 300 K and 100 K (black crosses).

The analysis of the TM bond distances as a function of temperature (Fig. III.50) reveals the nature of this phenomenon. While the Fe-O bond distance follows as expected a decreasing trend up to 50 K (then becoming almost invariant), the Mo-O bond length gradually tends to increase starting just below the Néel temperature as the T is decreased causing precisely the volume expansion appreciated in Fig. III.48.

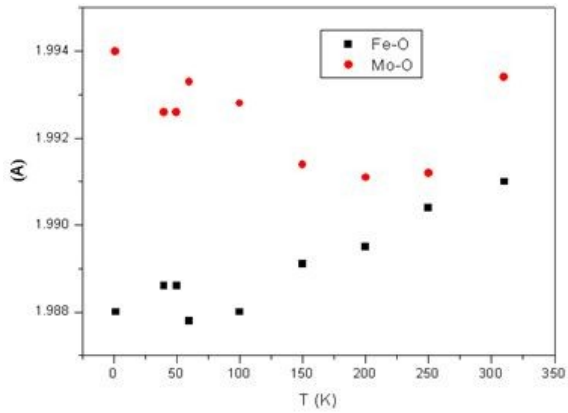

Figure III.50. Evolution of Fe-O (black squares) and Mo-O (red circles) bond lengths as a function of temperature.

E.3 PBFMO magnetometric characterization

The magnetic characterization of Pb_2FeMoO_6 was prevalently performed by means of SQuID magnetometry through a thermal and in-field data analysis.

E.3.1 Spontaneous thermal magnetization response of PBFMO

The measurement of spontaneous magnetic susceptibility have been recorded versus temperature using a combined ZFC-FC procedure applying a very weak (10 Oe) external field (Fig. III.51).

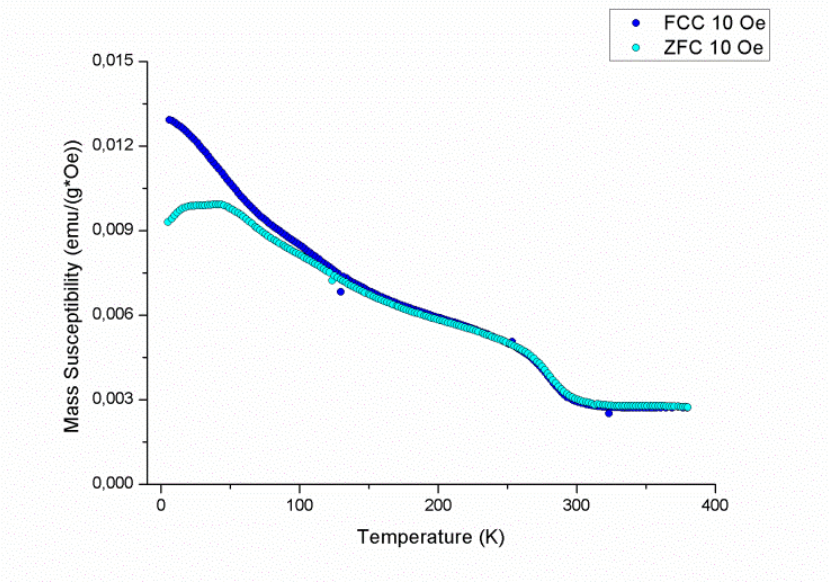

Figure III.51. ZFC (light blue dots) and FC (dark blue dots) susceptibility of a polycrystalline pellet sample of Pb_2FeMoO_6, performed at 10 Oe in the range 5 K ÷ 380 K.

At first sight, a sharp ferromagnetic-like transition is observed centered at T_N = 272 K, indicating a clear long range magnetic order arising from a paramagnetic disordered state. Nevertheless at lower temperature the ZFC curve highlights a second weaker phenomenon

which brings to a maximum at about 50 K and then to a lowering of the susceptibility as the system is cooled down to 5 K. This suggests the possible existence of a macroscopic component with pure antiferromagnetic nature of the interactions.

To interpretate and describe the global nature of the interactions, high-T magnetization measurements have been performed at higher temperatures, reaching the thermal region in which the paramagnetic state engages all the volume of the material. In this region, it is possible to study the magnetic response and to get information of two fundamental parameters: the Weiss temperature Θ and the number of magnetons for magnetic ion in the cell. This operation has been succesfully carried out with an applied magnetic field of 10 kOe and only above 400 K, where the system effectively shows a pure paramagnetic behavior.

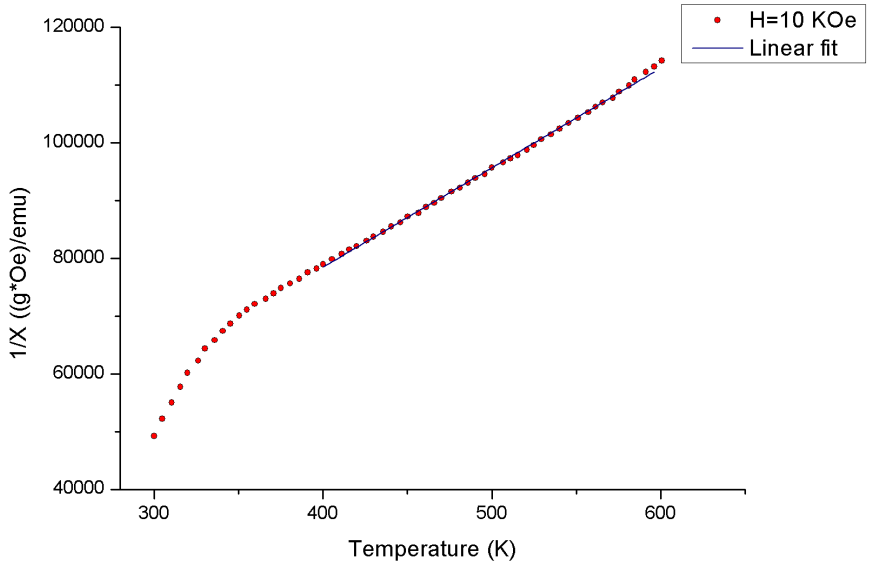

Figure III.52. Curie Weiss fit in the paramagnetic regime of PBFMO of inverted magnetic susceptibility collected at 10 kOe.

The need of such a higher field is due to the weak sensitivity of the used technique (the stationary pendulum magnetometer) toghether with the small quantity of sample in terms of mass. In this way, by means of a linear fit of the inverse of magnetic susceptibility (Fig.

III.52), I was able to obtain the experimental values of $\Theta = -55\ K$ and $3.92\ \mu_B$, with a good statistics. The negative sign of Θ, related to the mean negative sign of the exchange integral, is compatible with an antiferromagnetic and/or a ferrimagnetic order of the system. Because the magnetometric data show a sharp transition at 272 K, which is scarcely consistent with an antiferromagnetic character, a plausible hypothesis is the ferrimagnetic nature of the compound. Furthermore, the previously reported structural analysis pointed out a predominant ordered distribution of Fe^{3+} (d^5) and Mo^{5+} (d^1) magnetically active ions characterized by different intense magnetic moments (section *III.E.2*). An antiparallel arrangement of such moments brings inevitably to a ferrimagnetic pattern. However, the expected number of Bohr magnetons for magnetic ion in this scenario is $4.23\ \mu_B$ that is lightly underestimated but consistent with respect to the experimental value of $3.92\ \mu_B$.

E.3.1 In-Field Magnetometric analysis

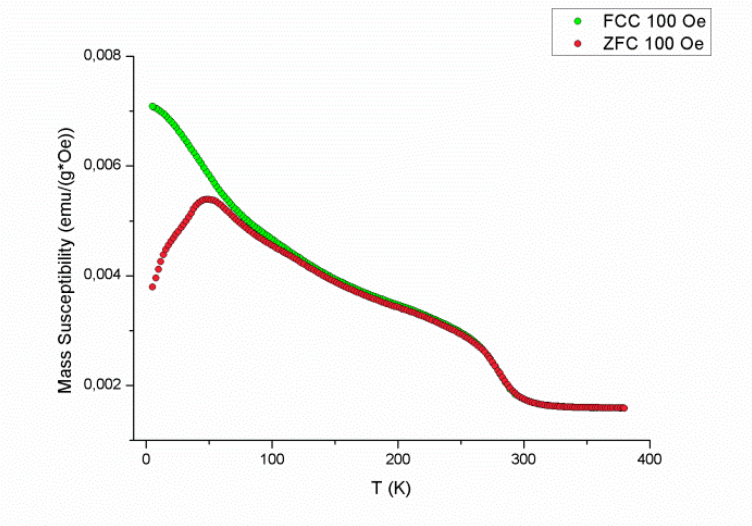

Figure III.53. ZFC (red dots) FC (green dots) susceptibility of a polycrystalline pellet sample of PBFMO, performed at 100 Oe in the range 5 K ÷ 380 K.

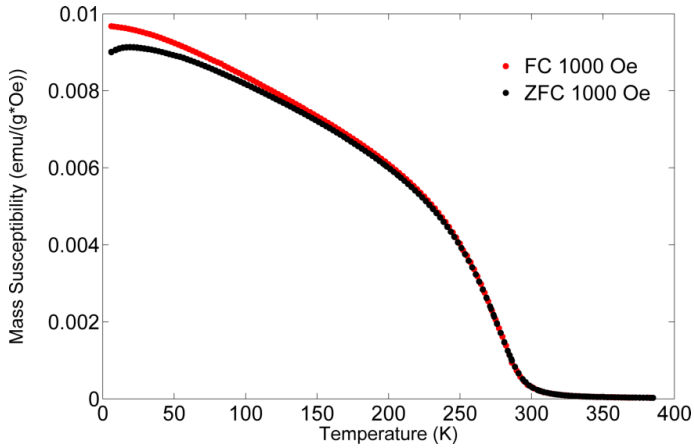

Figure III.54. ZFC (black dots) FC (red dots) susceptibility of a polycrystalline pellet sample of PBFMO, performed at 1000 Oe in the range 5 K ÷ 380 K.

In Fig. III.53 and Fig. III.54 are plotted a couple of ZFC-FC measurments collected with higher applied fields (100 Oe and 1000 Oe respectively).

In comparison with the data reported in Fig. III.51, both the curves show the occurrence of the same ferrimagnetic transition at T_N. But at lower temperatures if the 100 Oe ZFC curve shows again the same low-*T* antiferromagnetic-like feature with respect to that at 10 Oe (even amplified, the higher the lowering the narrower the maximum), the 1000 Oe ZFC curve did not display this behavior anymore and the curve is very close to that expected for a pure ferrimagnet. This evidence is very important and allows to consider the low-field lowering as second-order effect in the suscepitibility. Moreover the 1000 Oe FC curve results almost superimposed (aside just light differences at low T) to the corresponding ZFC, confirming that the ferrimagnetic contribution is completely predominant and almost saturated at 5 K. The so-deduced saturation of the ferrimagnetic response indirectly suggests the possible soft character of this magnetic phase. On the other hand the analysis of the low-field magnetometric data result to be much more complicated. Here, a coexistence of two magnetic contributions in the low magnetic field measurement conditions (ferrimagnetic at high-*T* together with a low T antiferromagnetic tail) is detected in analogy to what observed by means of the structural analysis, where 80% of the system is characterized by an ordered distribution of iron and molibdenum on the B-site of the perovskite while the 20% remnant

part shows acompositional disorder. The magnetic signal of the latter part is clearly lower because it is generated by a pattern of different superexchange interactions, such as the antiferromagnetic Fe-O-Fe. As a consquence they can become significant in term of magnetization only cooling in zero-field; an eventual external field on the contrary rapidly accentuates the ferrimagnetic resultant arising from the 80% of the compound.

In order to confirm the ferrimagnetism of the system I performed a study of the 5 K magnetization as a function of the applied magnetic field, cyclically spanning the range –50 kOe (–5 T) ÷ 50 kOe (5 T); the measurement is plotted in Fig. III.55. A ferromagnetic-like trend is observed, showing a saturation of the magnetization with symmetric values at –5 T and 5 T. The presence of this saturation confirms that the system behaves as a ferrimagnetic material and not of as an antiferromagnet. On the other hand, the loop highlights the absence of coercivity, implying that the direction of the resultant magnetization can be easily rotated and maximized by an opposite magnetic field. Hence, in this scenario the Fe-O-Mo antiferromagnetic interactions results to be highly polarizable. In parallel, this also means a negligible magnetic anisotropy of the material. In addition the value of saturation magnetization, around *1.75* μ_B for magnetic ion, is quite low, with respect to both the expected value of *4* μ_B for a ferrimagnetic arrangement of Fe^{3+} (d^5) and Mo^{5+} (d^1) and the value calculated at 5 K through the analysis of neutron diffraction data (see Fig. III.48).

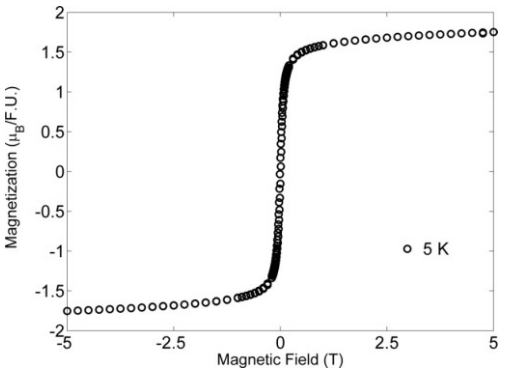

Figure III.55. Hysteresis loop measurement of PBFMO collected at 5 K, highlighting a superparamagnetic-like behavior with low saturation magnetization.

It is quite difficult to imagine such a lack of magnetic anisotropy in a polycrystalline compound. In fact a negligible residual magnetization and consequently a negligible coercive field are basic properties of the well known ideal superparamagnetism, which is usually displayed by non-interacting magnetic nanostructures. This last parallelism is even more surprising and probably deserves further investigations. By the way, in the first place, some considerations can be put forward. A low coercivity and high polarization can be observed in some cases also in bulk interacting magnetic systems characterized by magnetic disorder and inhomogeneity [11,20,22] (BFMO). On the basis of this consideration, I hypothesize that, in the case of PBFMO, the 20% disordered magnetic part may interrupt the long-range of the superexchange mediated Fe^{3+}-O-Mo^{5+} chains and may generate localized ferrimagnetic mesoscopic regions that cannot interact with each other. Due to this fact, a strong reduction of the coercive field can occur, making these regions non-interacting but highly sensitive to field variations, thus explaining simultaneously also the observation of very low or rather negligible coercivity and also the lowering of the saturation magnetization.

E.4 PBFMO transport properties

In order to unveil the possible occurrence of dielectric/polar character of PBFMO, the electrical properties were studied following the same chronological protocol applied in the case of BFMO. First, a polycrystalline pellet was properly prepared for transport measurements (see subchapter *II.H*). The preliminary measurement was a study of the thermal dependence of the electrical resistance.

The collected data, resulting with an applied electric bias of 0.25 V, are plotted in Fig. III.56.

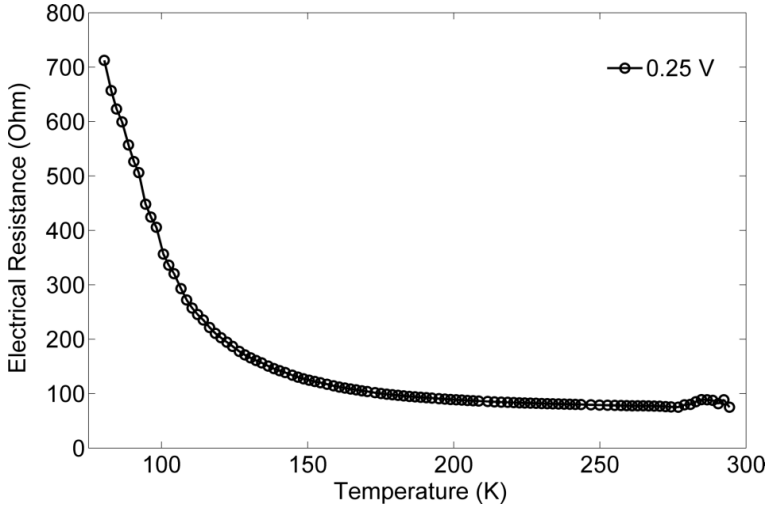

Figure III.56. Electrical resistance measured under an applied voltage of 0.25 V on a polycrystalline of PBFMO between 300 K and 80 K.

Other voltage biases were tested showing no macroscopic differences with respect to the proposed measurement, thus allowing their omission. The magnitude of the electrical resistance is surprisingly low in the whole thermal range, principally if it is compared to the values registered for BFMO, reported in Fig. III.14.

In fact, differently from BFMO, PBFMO shows a highly conductive character with resistance of the order of hundreds ohms (a difference of at least 5 order of magnitude).

Anyway, the temperature behavior seems to qualitatively follow that of a typical semiconducting material, with a thermally activated transport mechanism, and a exponential-like increase of the resistance with decreasing temperature. However, looking carefully at Fig. III.55, a strange anomaly precisely appears just below RT, with a broad peak anticipating the occurrence of the T_N of the system. Below this peak the resistance starts gradually to increase with a slow dynamics, suggesting that the thermal activation energy of the electric transport, k_BT, corresponds to lower temperatures. The fact that magnetic ordering can be related to a change of the electric properties is consequential to the observation of a strong modification also of the TM-O bond lengths, pointed out in section *III.E.2,* mainly for what concerns the molybdenum ion. The incoming ferrimagnetism acts to gradually stabilize the superexchange interactions in which the sole unpaired electron of Mo^{5+} is partially involved. Due to this phenomenon the material probably crosses around T_N a semi-metallic to semiconducting phase transition, in analogy to some similar magnetoresistive compounds, as for example Sr_2FeMoO_6.

In order to clarify the nature of the transport mechanism, Arrhenius plots of the R(T) curve were elaborated and shown in Fig. III.57. The trend does not reproduce the expected linear behavior, mainly in the low T regime (characterized by high values of the ratio 1000/T). At higher temperatures, just below the peak, the trend is not clear at this scale, and it needs a specific characterization.

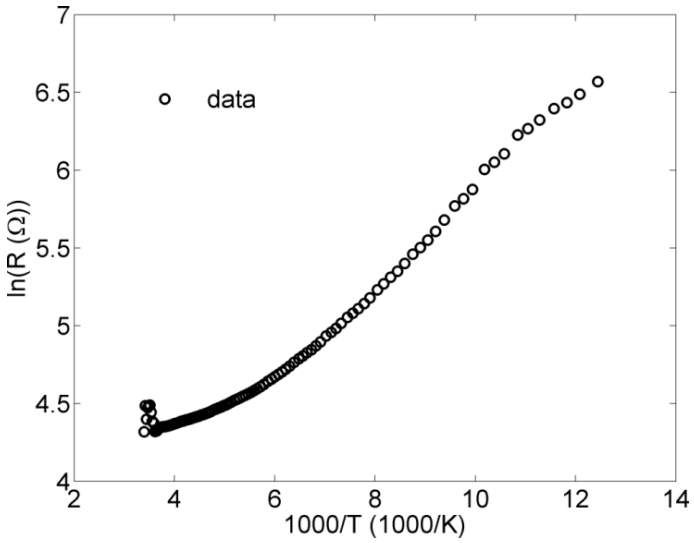

Figure III.57. Arrhenius plot of PBFMO electric resistance in the whole thermal interval.

As a consequence the thermal range between 195 K and T_N = 272 K was separately investigated finding an almost linear trend. The behavior was studied considering the three models used for BFMO, namely: TA, ANHSP and VRH (see Eqs. III.1-2-3, respectively). The results are really unexpected. The TA (see Fig. III.58(left-side)) and VRH model do not match the curve highlighting bad coefficients of determination. On the other hand, the ANHSP Holstein polaron model perfectly reproduces the curve with $R^2 = 0.9997$. This result, pictured in Fig. III. 58(right-side), visibly confirms such a good accordance. The calculated hopping energy $E_{HOP} = 0.43\ meV$ corresponds to a temperature of about 5 K, stating that the conduction band is well populated. This value experimentally demonstrates the low resistive character of PBFMO.

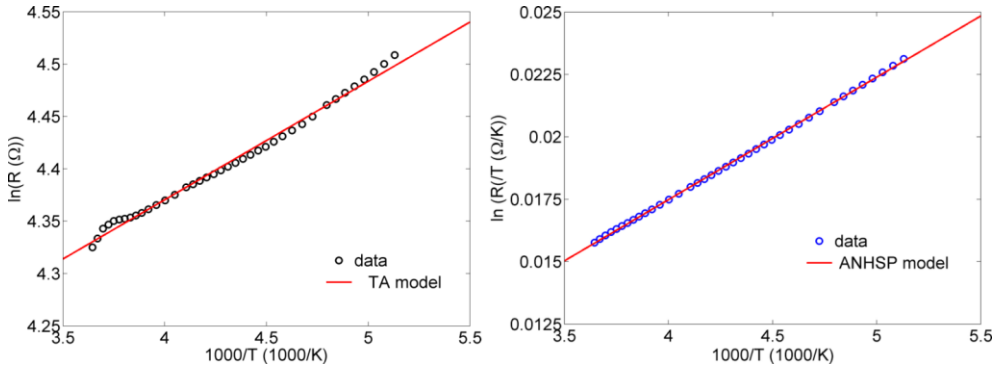

Figure III.58. Specific Arrhenius plots of the PBFMO electrical resistance between T_N =272 K and 195 K. On the left side of the figure, the curve is fitted with the classic thermally activated mechanism, while on the right side with the ANHSP Holstein polaron model.

The fact that precisely the ANHSP polaron model better reproduces the transport mechanism below T_N should not be surprising, since this is the model that takes into account a transport mechanism mediated by the structure, and it applies to systems with crystallographic order, just like PBFMO. This assertion finds additional support once the presence of compositional order involving the ions at the B-site is considered. Indeed the possible promotion of a high number of almost delocalized electrons in the conduction band can just derive from these crystallographic positions. In particular the role of Mo^{5+} is determinant since from the diffraction data the complete stabilization of its magnetic moment and so the localization of its electron only occur at about 50 K. Consequently the gradual thermally activated localization process of this electron is probably related to the huge enhancement of resistivity causing the deviation from the ANHSP model from about 190 K up to the minimum reached temperature of 80 K, where the agreement completely disappears. Despite these intriguing characteristics, such a low resistive response of PBFMO does not permit to perform any kind of dielectric characterization. Consequently, beside the results of structural analysis that suggested the absence of the necessary condition to ferroelectricity (i.e. centrosymmetric lattice with no detected distortion), it is confirmed by these measurements that PBFMO is not a good candidate to multiferroism. Nevertheless, it is probably a promising magnetoresistive compound.

E.5 Magnetoresistance in PBFMO

Magnetoresistance was tested with the Van der Pauw four-contacts technique on a larger and thinner discoid sample, with respect to that studied in the previous section *III.E.4*.

The sample was brought to 200 K, 150 K and 20 K exploiting the SQuID magnetometer cryostat, alternatively by means of ZFC, FC at ±40 kOe protocols, starting from RT. Reached the temperature set-point, the electrical resistance was measured as a function of the external magnetic field spanning from –40 kOe to +40 kOe. The set of results is plotted in Fig. III. 59.

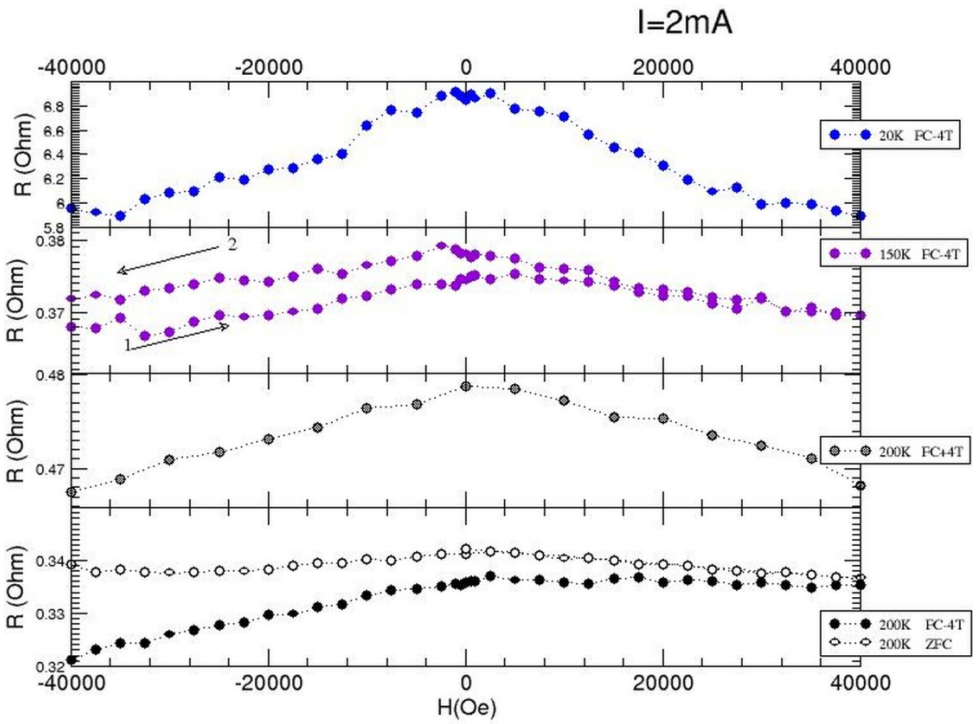

Figure III.59. Magnetoresistance measurements collected between –40 kOe and 40 kOe in different thermal and field cooling conditions: (from the bottom to the top) at 200 K: after ZFC (white circles), –40 kOe FC (black circles) and +40 kOe FC (grey circles); at 150 K after –40 kOe FC (purple circles); at 20 K after –40 kOe FC (blue circles).

The analysis of these curves point out a very intriguing scenario. The role played by the thermal cooling conditions seems to affect the overall behavior of PBFMO so that a distinct discussion for each temperature is needed, at least to better clarify the observed characteristics.

- At RT no magnetoresistance effects is detected.

- At 200 K, no-magnetoresistance is measured when the sample is cooled in zero-field conditions and the registered resistance retains the same value, around *0.34 Ω*. However, if the same measurement is carried out after field cooling in ±40 kOe, the observed phenomenology is drastically changed in a way that depends also on the applied field direction. Specifically, after –40 kOe field cooling, the electric resistance at zero-field promptly shows a small decrease (black circles of Fig. III.59), followed by an asymmetric response with respect to the field orientation during the measurement. For negative fields, a significant reduction of the electrical resistance is observed leading to a loss of 6% in magnitude at –40 kOe. Completely different is the situation in the positive field regime, where a substantial invariance of the resistance with respect to the zero-field value is registered. This evidence possibly suggests the presence of a transport mechanism driven by polarized carriers, a very important characteristic for eventual spintronic applications.

Contrasting phenomenology is displayed the case of the measurement after 40 kOe FC procedure. Surprisingly this operation leads to a strong enhancement of the recorded electrical resistance, estimated to be 40%, already at 0 Oe, if compared to the zero field cooling measurement. A classical symmetric magnetoresistive effect is so measured (grey circles of Fig. III.58) with a maximum relative loss of about 3% at –40 kOe and 40 kOe. In this case the effect of a strong magnetic field during the cooling acts in an reduction of the conduction avoiding the promotion of the polarized carriers.

- At 150 K, a magnetoresistance loop between –40 kOe / 40 kOe /–40 kOe is performed after a field cooling in –40 kOe. I limit the attention to this protocol, because beside all the other peculiarities detected at 200 K, the most promising perspective specifically arises from the possible confirmation of the asymmetric response of magnetoresistance and thus of the

presence of polarized carriers. Fortunately, the obtained results are encouraging (purple circles of Fig. III.59). A little hysteretic behavior is detected opening a 1 ÷ 2 % relative gap at –40 kOe, while a good superimposition is observed in the positive branch of the magnetoresistance curve. Once again, in isothermal condition, for negative applied fields the system still seems to respond with a selective reduction of its resistance. Hence, if polarized carriers are present, they are characterized by a spin resultant prevalently oriented in the negative field direction. For the sake of honesty, it is worth to note that the asymmetry of the curve together with the intensity of the magnetoresistive effect are strongly reduced by the lowering of temperature (compare the measurement at 150 K with that at 200 K of the previous case). This result provides once again a support for the hypothesis carried out in section *III.E.4* to explain the link between the strong variations of the transport properties with the incoming gradual stabilization of Mo-O bond length, as deduced from neutron diffraction data of section *III.E.2* (Fig. III.50).

- Finally at 20 K the asymmetric behavior is totally cancelled by temperature, confirming what has been just said on the effect of the stabilization of Mo-O bond length connected to the localization process of the spin polarized electrons. On the other hand, the 15% relative variation of the resistance, recorded both at ±40 kOe, represents the maximum detected value with respect to all the other cases, demonstrating that PBFMO is a magnetoresistive compound.

E.6 Conclusions on PBFMO characterization

Pb_2FeMoO_6 is an interesting compound belonging to the class of Pb-based double perovskites. It is synthesized only by means of HP/HT environments, due to the difficulty to stabilize Mo^{5+} in octahedral coordination with standard techniques. PBFMO crystallizes in a highly symmetrical cubic cell with the typical structure of a quadruple perovskite with $a' = 2a_{sp}$ and space group *F-m3m*. Therefore, differently from BFMO, no tilt and rotations of the octahedra of coordination are observed. The synchrotron data allowed to discriminate the predominant presence of order on the B-site between Fe^{3+} and Mo^{5+}, involving the 80% of the ions.

From such an ordered distribution, long-range ferrimagnetic structure arises with T_N = 272 K. Due to the big difference between the iron d^5 and molybdenum d^1 magnetic moments, a large saturation magnetization is observed by neutron diffraction magnetic analysis and in a sufficiently good accordance also with magnetometric characterization. The study of lattice parameters thermal evolution indicates the presence of sharp structural modifications, not in terms of symmetry but of density, starting below T_N. The incoming ferrimagnetic order causes clear effects on the TM-O bond lengths too. In particular, the Mo-O length expands below T_N, and continues to increase as the temperature is lowered until 50 K, when it stabilizes. This gradual expansion is responsible for the observed low-*T* cell volume expansion and also for the gradual mechanism of saturation of the magnetization.

PBFMO reveals an intriguing spontaneous magnetic response with an evident ferrimagnetic transition centered at T_N and followed by a low-*T* antiferromagnetic tail well visible in the ZFC curve. With applied fields of the order of thousand Oe this effect disappears. Consequently, ZFC and FC superimpose and the system displays a simple ferrimagnetic behavior, suggesting that the observed low-field antiferromagnetism is a secondary and probably disorder-related phenomenon, involving the 20% part of the material in which antiferromagnetic interactions are present (due to its compositional inhomogeneity). Such part of the material is also possibly engaged in the observed low saturation magnetization, with respect to that theoretically calculated for an ordered single crystal uniquely constituted by Fe-O-Mo chains with superexchange interactions. Furthermore, the 20% disordered part

is also potentially linked to the complete absence of magnetic anisotropy and coercivity of the magnetic structure as detected by hysteresis loop measurements. In fact since these region may break the long-range macroscopic 3D arrangement of Fe-O-Mo interaction, confining this order at the mesoscopic scale; therefore this may imply a spatial distributions of separated and almost non-interacting ferrimagnetic regions highly polarizable by the external field.

Electric transport analyses point out that PBFMO is a low resistive compound characterized, at RT, by a semi-metallic behavior. Nevertheless the magnetic ordering process affects also the transport mechanism, as well as the structural and magnetic properties. In this case the system electrical resistance, studied in a short 80 K interval below T_N, matches the typical thermal dependence predicted by the Holstein polaron model (or rather ANHSP), suggesting that the transport is driven by adiabatic nearest-neighbors hopping carried by partially delocalized molybdenum electrons. On the basis of this hypothesis, when the Mo-O length is stabilized, this electron is localized and the resistance of the material at low temperature rapidly shall increase, as correctly observed.

The absence of a dielectric character, in the whole thermal range, excludes the possibility of multiferroism in PBFMO. However electric resistance characterization as a function of an external magnetic field proves the occurrence of magnetoresistance. In particular a symmetrical magnetoresistive effect, with respect to the sign change of the applied external magnetic field, is measured as the temperature is cooled from T_N to very low temperatures (20 K). In addition to this experimental evidence, asymmetrical magnetoresistive anomalies were detected between T_N and 150 K. Specifically, the promotion of a conduction mechanism under the application of negative fields is recorded possibly ascribed to polarized electron transport type. This phenomenology is more pronounced in the thermal regime in which the Mo electron behaves as a partially delocalized particle promoting the Holstein polaron-mediated electrical transport.

In conclusion, further characterizations are needed to improve the knowledge about the physics of PBFMO. Precisely, a comprehensive set of additional electrical characterizations together with the exploitation of local techniques, like Mössbauer Spectroscopy and/or Raman spectroscopy, supported by theoretical modelization such as Density of States (DOS)

analyses could effectively be determinant in the long way towards the complete understanding of the compound properties. Nevertheless, even just considering the presented results, PBFMO can be correctly considered, differently from BFMO, a proper multifunctional material and consequently a good candidate not for multiferroic but at least for spintronic applications.

References

[1] Y. Maeno, H. Hashimoto et al. *Nature* **372,** (6506) 532–534 (1994).

[2] A. Arulraj, K. Ramesha, J. Gopalakrishnan, and C. N. R. Rao *J. Solid State Chem.* **155**, 233 (2000).

[3] K. I. Kobayashi, T. Kimura, Y. Tomioka, H. Sawada, K. Terakura, and Y. Tokura *Phys. Rev. B* **59,** 11159 (1999).

[4] N. Hamada, and Y. Moritomo *The 3rd Japan-Korea Joint Workshop on First-Principles Electronic Structure Calculations* **1**, 56 (2000).

[5] Y. Moritomo, S. Xu, A. Machida, T. Akimoto, E. Nishibori, M. Takata, and M. Sakata *Phys. Rev. B* **61,** 7827(R) (2000).

[6] K. I. Kobayashi, T. Kimura, H. Sawada, K. Terakura, and Tokura Y. *Nature* **395**, 677 (1998).

[7] J. B. Goodenough *J. Phys. Chem. Solids* **6,** 287 (1958)

[8] J. Kanamori *J. Phys. Chem. Solids* **10**, 87 (1959).

[9] T. Kimura, S. Kawamoto, I. Yamada, M. Azuma, M. Takano, and Y. Tokura *Phys. Rev. B* **67**, 180401(R) (2003)

[10] A. Sundaresan, R. V. K. Mangalam, A. Iyo, Y. Tanaka, and C.N.R. Rao *J. Mater. Chem* **18**, 2191–2193 (2008)

[11] D. Delmonte, F. Mezzadri, C. Pernechele, G. Calestani, G. Spina, M. Lantieri, M. Solzi, R. Cabassi, F. Bolzoni, A. Migliori, C. Ritter, and E. Gilioli *Phys. Rev. B* **88,** 014431 (2013).

[12] P. Mandal, A. Sundaresan, C. N. R. Rao, A. Iyo, P. M. Shirage, Y. Tanaka, C. Simon, V. Pralong, O. I. Lebedev, V. Caignaert, and B. Raveau, *Phys. Rev. B* **82**, 100416 (2010).

[13] M. C. Burla, R. Caliandro, M. Camalli, B. Carrozzini, G. L. Cascarano, L. De Caro, C. Giacovazzo, G. Polidori, and R. Spagna *J. Appl. Cryst*. **38**, 381 (2005).

[14] G. M. Sheldrick *SHELXL97: Program for the crystal structure refinement.* Univ. of Gottingen,Germany (1993).

[15] M. Nespolo, G. Ferraris, and H. Ohashi, *Acta Cryst. B* **55**, 902 (1999).

[16] A. M. Glazer *Acta Cryst. B* **28,** 3384 (1972).

[17] K. Momma, and F. Izumi, *J. Appl. Crystallogr.***44**, 1272 (2011).

[18] A. A. Belik, A. M. Abakumov, A. A. Tsirlin, J. Hadermann, J. Kim, G. Van Tendeloo, and E. Takayama-Muromachi *Chem. Mater.* **23**, 4505 (2011).

[19] P. Mandal, C. R. Serrao, E. Suard, V. Caignaert, B. Raveau, A. Sundaresan and C. N. R. Rao *J. Solid State Chem*. **197**, 408 (2013).

[20] A. A. Belik, *Inorg. Chem.* **52**, 2015 (2013).

[21] M. J. Benitez, O. Petracic, H. Tüysüz, F. Schüth, and H. Zabel *Phys. Rev. B* **83,** 134424 (2011).

[22] D. Delmonte et al. *J. Phys. Condens. Matt.* Submitted in January (2015).

[23] D. Delmonte et al. Phys. Rev. B Submitted in December (2014).

[24] S. B. Abdelkhalek, N. Kallel, S. Kallel, T. Guizouarn, O. Peña, and M. Oumezzine *J. Superconductivity and Novel Magn.* **26**, 3171-3180 (2013).

[25] R. Cabassi, F. Bolzoni E. Gilioli, F. Bissoli, A. Prodi, and A. Gauzzi *Phys. Rev. B* **81**, 214412 (2010).

[26] R.M. Kusters, J. Singleton, D.A. Keen, R. McGreevy, and W. Hayes *Physica B* **155**, 362 (1989).

[27] M. F. Hundley, M. Hawley, R. H. Heffner, Q. X. Jia, J. J. Neumeier, J. Tesmer, J. D. Thompson, and X. D. Wu *Appl. Phys. Lett.* **67**, 860 (1995).

[28] G. C. Xiong, S. M. Bhagat, Q. Li, M. Domínguez, H. L. Ju, R. L. Greene, T. Venkatesan, J. M. Byers, and M. Rubinstein *Solid State Commun*. **97**, 599 (1996).

[29] D. Emin, and T. Holstein *Ann. Phys.* **53,** 439 (1969).

[30] N. F. Mott, and E. A. Davies *Electron Processes in Non-crystalline Materials* Clarendon, Oxford (1979).

[31] N. F. Mott, *Conduction in Non-Crystalline materials* Clarendon Oxford 17–23 (1993).

[32] A. Banerjee, S. Bhattacharya, S. Mollah, H. Sakata, H. D. Yang, and B.K. Chaudhuri *Phys. Rev. B* **68**, 186401 (2003).

[33] A. L. Efros, and B. I. Shoklovskii *J. Phys. C* **8**, L49 (1975).

[34] A. L. Efros *J. Phys. C: Solid State Phys.* **9**, 2021 (1976).

[35] R. Parthasarathy, X. M. Lin, K. Elteto, T. F. Rosenbaum, and H. M. Jaeger *Phys. Rev. Lett.* **92**, 076801 (2004).

[36] D.Yu, C. Wang, B. L. Wehrenberg, and P. Guyot-Sionnest *Phys*. *Rev*. *Lett*. **92**, 216802 (2004).

[37] T. B. Tran, I. S. Beloborodov, X. M. Lin, T .P. Bigioni, V. M. Vinokur, and H.M. Jaeger *Phys. Rev. Lett.* **95**, 076806 (2005).

[38] L. Néel *Ann. Phys.* Leipzig **3**, 137 (1948).

[39] E. W. Gorter, and J.A. Schulkes *Phys. Rev.* **90**, 487 (1953).

[40] R. Pauthenet *J. Appl. Phys.* **29**, 253 (1958).

[41] S. I. Ohkoshi, T. Iyoda, A Fujishima, and K. Hashimoto *Phys. Rev. B* **56**, 11642 (1997).

[42] S. I. Ohkoshi, Y. Abe, A. Fujishima, and K. Hashimoto *Phys. Rev. Lett*. **82**, 1285 (1999).

[43] K. Yoshii, A. Nakamura,Y. Ishii, and Y. Morii *J. Solid State Chem.* **162**, 84 (2001).

[44] K. Yoshii *J. Solid State Chem.* **159**, 204 (2001).

[45] V. A. Khomchenko, I. O. Troyanchuk, R. Szymczak, and H. Szymczak *J. Mater. Sci.* **43**, 5662 (2008).

[46] Y. L. Su, J. C. Zhang, Z. J. Feng, L. Li, B. Z. Li, Y. Zhou, Z. P. Chen, and S. X. Cao *J. Appl. Phys.* **108**, 013905 (2010).

[47] Nagamalleswararao Dasari, P. Mandal, A. Sundaresan, and N. S. Vidhyadhiraja *EPL* **99**, 17008 (2012).

[48] K. Vijayanandhini, C. Simon, V. Pralong, Y. Bréard, V. Caignaert, B. Raveau, P. Mandal, A. Sundaresan, and C. N. R. Rao *J. Phys. Cond. Mat.* **21,** 486002 (2009).

[49] J. Puerta, and P. Martin *Appl. Opt.* **20**, 3923 (1981).

[50] D. G. Rancourt *Nucl. Instr. And Meth. B* **44**, 199 (1989).

[51] D. Kothari ,V. Raghavendra Reddy, A. Gupta, C. Meneghini, and G. Aquilanti *J. Phys. Condens. Matter* **22**, 356001 (2010).

[52] V. S. Pokatilov, A. S. Sigov, and A. O. Konovalova *Bulletin of the Russian Academy of Sciences: Physics* **74**, 347-351 (2010).

[53] Q. A. Pankhurst, and R. J. Pollard *Applied field Mössbauer Spectroscopy of magnetic powders* in: G. Long, F. Grandjean (Eds.), Mössbauer Spectroscopy Applied to Magnetism and Materials Science vol. 1, Plenum Press New York (1996).

[54] F. Bødker, M. F. Hansen, C. B. Koch, K. Lefmann, and S. Mørup *Phys. Rev. B* **61,** 6826 (2000).

[55] M. A. Chuev *Doklady Physics* **57** 421 (2012) and references therein.

[56] L. Cianchi L, F. Del Giallo, G. Spina, W. Reiff, and A. Caneschi *Phys. Rev. B* **65,** 0644415 (2002).

[57] D. Rancourt *Analytical methods for Mössbauer spectral analysis of complex materials*, in: G. Long, F. Grandjean (Eds.), Mössbauer Spectroscopy Applied to Magnetism and Materials Science vol. 2, Plenum Press New York (1996).

[58] Y. L. Chen, and Y. De-Ping *Mössbauer Effect in Lattice Dynamics* Wiley-VCH, Weinheim (2007).

[59] A. P. Menushenkov, A. V. Kuznetsov, R. V. Chernikov, A. A. Ivanov, V. V. Sidorov, and K. V. Klementiev *J. Supercond. Nov. Magn.* **27,** 925 (2014).

[60] G. Geneste, H. Dammak, M. Hayoun, and M. Thiercelin M *Phys. Rev.* **87,** 014113 (2013).

[61] L. Cianchi, F. Del Giallo F, F. Pieralli, M. Mancini, S. Sciortino, G. Spina, R. Ammannati, and R. Garré *Solid State Commun.* **80,** 705 (1991).

[62] M. Capaccioli, L. Cianchi, F. Del Giallo, F. Pieralli, and G. Spina *J. Phys. Condens. Matter*, **7** 2429 (1995).

[63] D. Delmonte, F. Mezzadri et al. *Inorg. Chem.* (2015) under submission.

[64] X. Yuan, M. Xu, and Y. Chen *Appl. Phys. Lett.* **103**, 052411 (2013).

IV. Conclusions

This chapter is devoted to sum up my doctoral activity, spent among the Physics and Earth Science Department of the University of Parma and the Institute of Materials for Electronics and Magnetism (IMEM) of the National Research Council (CNR).

Since the beginning of 2011, a group of researchers in Parma decided to start a new line of research in the field of multiferroic magnetoelectric materials. These materials, belonging to the wide class of multifunctional compounds, are nowadays arousing big interest within the scientific community, either for fundamental and applied research. Multiferroic magnetoelectrics are materials in which magnetic and electric orders coexist and are coupled. In nature, spontaneous multiferroic magnetoelectrics are extremely rare due to strong structural and physical constraints required for the occurrence of the phenomenology. Consequently, the use of unconventional techniques such as high-pressure / high-temperature (HP/HT) and pulsed laser deposition systems (for bulk and film phases, respectively) is mandatory to produce artificial multiferroic phases. Moreover, for the experimental study of such exotic materials, the exploitation of standard physical characterization measurements is not sufficient to unveil their physical properties, imposing the development of novel and unconventional techniques.

These challenges represent my engagement rules within this fascinating research project. After three years of work, I turned out to establish a self-standing laboratory committed to the experimental characterization of multiferroic magnetoelectric properties. In particular, standard magnetometric techniques and standard electrical measurements techniques have been assembled in a unique platform (based on a “simple” SQuID magnetometer), to properly perform combined electric and magnetic investigations. Moreover, a high-voltage setup for ferroelectric characterization, equipped with the AIXACCT TF-Analyzer 2000, has been optimized and tested, allowing to study also bulk samples with non-dielectric properties (just like many multiferroics). These outcomes are non-trivial when one considers the number of technological problems to face, as is proved by the fact that, in spite of the large number of publications in this field, a complete magnetoelectric characterization is yet hard to find.

Beside this experimental work, an equal effort was devoted to the production and characterization of novel bulk systems with potential multiferroic magnetoelectric character, specifically by means of HP/HT solid state reactions. In four years, I stabilized more than ten single-phase compounds belonging to the perovskite ABO_3 class. Due to its large tolerance, perovskite lattice enables a variegate number of chemical substitutions and structural distortions. In these materials, magnetism and ferroelectricity derive from independent mechanisms; ferroelectricity is induced exploiting the stereochemical effect of Bi^{3+} or Pb^{2+} ions on the A-site of perovskite, while magnetism is promoted by the introduction of two different III-IV period metal cations (i.e. Cr, Mn, Fe, Co, Cu; Mo) on the B-site of perovskite. Systems obtained by these chemical substitutions, are usually called double perovskites, with general formula $A_2BB'O_6$. The choice of a double substitution on the B and B'-site can be explained considering that it may allow a lowering of the space and time-symmetry (operation that in some cases contributes to the coexistence of magnetic and electric order); on the other hand the presence of different magnetic interactions usually promotes high Curie temperatures despite an enhancement of the system complexity. It is worthwhile to recall that strong magnetoelectric coupling and high ordering temperature are the main requirements for practical application of multiferroics.

Within this Thesis, I mainly focused on the study of two compounds, because of their completely different multifunctional character:

- $BiFe_{0.5}Mn_{0.5}O_3$ (BFMO) -refer to sections *III.C.6* and *III.D.5* for a detailed description of the scientific results-

- Pb_2FeMoO_6 (PBFMO) -refer to section *III.E.6* for the same reasons pointed out above)-

BFMO in particular revealed intriguing, although complex, properties requiring magnetometric, structural, ferroelectric and magnetoelectric characterization to investigate its overall physical behavior. BFMO displayed a highly distorted cell with a strong compositional inhomogeneity involving the spatial distribution of iron and manganese; it showed coexistence of a RT (antiferro)magnetic order (T_N = 288 K) and ferroelectricity, which is irreversibly induced by an external DC electric bias (just below the semiconductor-to-insulator onset, occurring at T_P = 140 K). In addition, some interesting evidences of magnetoelectric coupling, measured by means of the combined magnetic/electric

techniques, were highlighted, such as the observation of magnetic ordering-induced changes of the transport properties; the occurrence of magnetocapacitance effects and the detection of a tuning of the magnetization thermal dependence under a DC electric bias application. Especially the latter experimental outcome unequivocally promotes BFMO as a possible bulk multiferroic magnetoelectric compound.

Despite these preeminent results, BFMO gave also the chance to study exotic phenomenologies subsidiary to multiferroism and magnetoelectricity but incredibly fascinating, specifically:

- the thermal activated field-dependent spontaneous magnetization reversal process;

- the Mott's Variable Range Hopping transport mechanism characterized by unusual monodimensional conductance.

These two mechanisms were deeply investigated since nowadays a general consensus on their interpretation is still lacking. The presented data allowed to describe them as disorder-related phenomena, pointing out the crucial role played by composition inhomogeneity in the spatial distribution of iron and manganese ions.

On the contrary, PBFMO showed completely different phenomenologies. It is a ferrimagnetic compound (T_N = 272 K) with a strong conductive electric character. Due to the highly symmetrical crystallographic structure, induced by a partial order on the B-site (~80%) involving iron and molybdenum ions, PBFMO did not show chances to be multiferroic. However, it displayed a considerable magnetoresistance; besides the measurement of a notable low-*T* magnetoresistive effect (~15%), electric transport seems to be characterized just below T_N by spin-polarized electrons making PBFMO a suitable candidate for spintronic applications.

The future objectives will focus on a consolidation and further implementation of the experimental setups at the basis of this research work. Nevertheless, an enlargement of our products scientific impact and applicative perspective would be decisive to sustain the activity costs; in this scenario a promising development may be achieved moving towards the area of the multiferroic film fabrications. Non-equilibrium thin film deposition techniques, such as the Pulsed Electron Deposition developed at IMEM-CNR can permit a

fundamental step forward. The first attempts to grow metastable multiferroic thin films are in progress; in this light, the acquired competences and experimental backgrounds are the essential building block to start a new research line.

I chose a personal consideration to conclude. The large number of comprehensive studies, which go truly beyond the presented results, gave me the opportunity to extent my knowledge and my attitude in facing scientific problems. Despite the truly interesting results achieved so far, I mainly consider this aspect as unavoidable goal in a doctorate traineeship.

Appendix

In this brief appendix I spend some words about the two principal collaborations in which I was involved during the Ph.D Thesis. I do this because, in the early 2014, thanks to my contribution, these activities brought to important results culminating in just as many patent licenses. The argument of my studies within this cooperations, together with a list of the patent authors and the correspondent references are reported below:

- characterization of the piezoelectric effect induced by ZnO nanorods functionalization in fully-integrated carbon fibers-based devices for sensing applications

Patent authors: Davide Calestani, Nicola Coppedé, Maurizio Culiolo, Davide Delmonte, Marco Villani, Andrea Zappettini, Laura Marchini, Rocco Bercella.

registered by Institute of Materials for Electronics and Magnetism (IMEM) CNR and Bercella S.R.L. (Patent Ref. 1).

- Writing of a simulation software for implementing the industrial scalability of the production process based on *16*16 cm*^{2} Cu(In,Ga)Se_2(CIGS)-based solar cells deposited by Pulsed Electron Deposition (PED) technique

Patent authors: Matteo Bronzoni, Davide Delmonte, Edmondo Gilioli, Massimo Mazzer, Francesco Pattini, Stefano Rampino.

registered by IMEM-CNR. (Patent Ref. 2).

As it can be argued, the presented topics belong to fields external to the multiferroic world. For these reasons my engagement has also represented the chance to expand my knowledge by facing completely different scientific issues. On the other hand, I think that my presence

inside a group of people with experiences in field of research different if not complementary to mine, can have possibly given an important push in reaching such good outcomes.

By considering that the main claims of each work have still to be kept protected due to their industrial innovative impact; I am imposed to write a discussion limited to those general aspects at least sufficient to focus the problem and its proposed solution. In the following the two activities are described in separated section.

Characterization of Piezoelectric effect in ZnO-functionalized Carbon fibers

ZnO is a compound well known to Material Scientists. Due to several interesting physical properties (wide band gap, high exciton binding energy, non-centrosimmetry of würtzite structure, piezoelectricity) it finds application in a variegate range of industrial areas but mainly in the field of sensing device technology. Moreover, due to its polar structure, ZnO can be obtained in different morphologies, (e.g. nanorods, nanoribbons, nanoparticles etc.) with a relatively cheap cost of production. In addition, these nanostructures can be integrated on different substrates of interest, or functionalized with other materials of choice. This perspective is very fascinating as far as the current rush to novel multifunctional components is considered. For what concerns piezoelectricity, foreseeing the ZnO integration into vehicles or buildings components, it would envision a revolutionary turning point in the field of transports and architecture.

The present activity has to be collocated in this scenario. In the frame of a collaboration between IMEM-CNR and Bercella S.R.L. (a company active in the production and manufacturing of carbon fiber structures), my colleagues succeeded to uniformly grow thin ZnO nanorods on single carbon fibers. Such carbon fibers, at a former or a later stage, can be bundle together or knitted in order to be utilized as structural constituents of the new generation car, plane and helicopter-shells. Despite the growth of ZnO on carbon fiber does not represent a novelty in the scientific community [3,4], a reliable characterization of the piezoelectric effect in the overall "system" (hereinafter the name given to our ZnO nanorods + carbon fiber device) resulted to be extremely complex or in some cases even tricky, causing some contradictory or uncompleted results in the prior art [5,6]. By means of standard methods, the piezoelectric effect is measured recording a DC voltage and/or a current generated by an external stress on devices in which the piezoelectric medium (i.e. the ZnO functionalized carbon fiber) is circuited together with a metal contact. This electrical continuity creates a Schottky barrier that favors, in principle, the collection of the displacive or polar signal directly on the gold wire. Specifically the voltage time variations, in open circuit conditions, and alternatively the current intensity variations, in short circuit

conditions, during the application and the release of a controlled stress oriented along ZnO rods' length direction is precisely due to the piezoelectric effect.

Despite this technique results effective in the case of purely insulating piezoelectrics, it is occasionally exposed to serious limitations when the sample presents a non-negligible, if not predominant, resistive character. The reader has to interpret my contribution to such research on the basis of this challenge. I worked to make possible a piezoelectric characterization measurement on a self-standing fully integrated product. Basically, my efforts were devoted to avoid the use of metal contacts in order to skip the Schottky-barrier effect and all the related collateral issues.

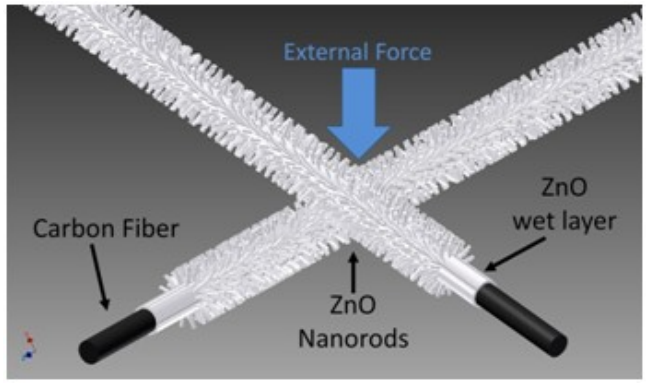

Figure A.1. A graphical representation of our tested "system" that is deprived by any other electrical components or contacts.

To reach this goal we thought and designed the "system" device, sketched in Fig. A.1. In this new scenario the standard characterization method is no more reliable. However, since piezoelectricity is a dielectric phenomenon related to a lowering of the spatial symmetry under a stress application, a significant strategy to study this property could be that of a dielectric characterization. The dielectric measurement is carried out by stimulating through an external pressure the piezoelectric effect of the sole ZnO nanorods lying in the crossing region between the two carbon fibers. In the presented system the electrical wiring elements are directly the carbon fibers themselves (this is theoretically possible as far as the good

conductance of graphite is concerned) and the ZnO nanorods represent the dielectric material interposed between them (carbon fiber play the role of the capacitor plates). Exploiting this solution, I am able to move away from the investigation of the I-V and R-V characteristics (typical of the standard methodology) and on the contrary focus on the Q-V and C-V characteristics. Anyway, these kinds of measurements present a fundamental problem associated to the intrinsic device electrical response, specifically the too high electrical permeability of the ZnO nanorods. From an experimental point of view, high amount of permeability imply that, under the application of an external DC voltage, electrons can flow through the ZnO nanorods and shield the displacive piezo-current. In addition, the induced polar charge drops to zero, deleted by the current flow. This fundamental drawback can be exclusively avoided by achieving high frequency voltage pulses in spite of DC biases. Indeed, frequency can discriminate the resistive or capacitive path of the current within the sample. In most cases, our samples result to be completely switchable from the resistive regime to the capacitive (dielectric) one, for frequencies higher than 1 kHz. This statement suggests that the AIXACCT TF-Analyzer 2000, deeply explained in section *III.G.1*, is the ideal instrument for such a piezoelectric study. Once the dielectric regime is selected by the proper electrical field frequency (which relies upon the total impedance of the system), the effect of a constant external pressure on the device electrical properties can be studied, ensuring that the measured current is not affected by spurious conductive leakage or capacitive losses contributions. What is expected is a switch from neutral to polar charge distribution, under mechanical stress, resulting in a current flow inside the material that balances the dipole formation (polaritazion current). However, the characteristic time duration of this process is much shorter than the period of our writing/reading voltage pulse (*1 ms* corresponding to *1 kHz*) so that the pulse cannot be synchronized to the polarization current not allowing the recording of its time evolution. Consequently, what can be done is renouncing to directly record the stress induced current polarization, and use the voltage intensity to depolarize the system retained under a constant stress condition. This is possible since the piezoelectric material is also ferroelectric until it is kept under deformation. In such a case, the induced ferroelectricity shows a charge (polarization) hysteretic behavior as a function of the intensity of the applied bias, characterized by an intrinsic coercive voltage and spontaneous polaritazion. With a proper

triangular pulse (whose intensity and frequency has to be set according to sample impedance), it is possible to depolarize the system and reverse the polarization. By integrating the current, measured point by point in correspondence of different amount of voltage along the triangular curve, ferroelectric hysteresis can be plot, and the intensity of the induced dipolar moment (related to the intensity of the piezoelectric displacement) can be derived. Such test effectively succeeds. The relative I-V and P-V curves are reported in Figs. A.2 and A.3, highlighting the expected scenario.

- The I-V curve (Fig. A.2) is characterized by the typical voltage-invariant current trend expected for a pure dielectric insulating material (noteworthy the dielectric current intensity does not depend on the applied voltage). In correspondence to almost symmetrical voltage intensities 9 ÷ 14 and –10 V ÷ –15 V, two peaks are detected. These peaks are the characteristic polarization lobes typical of ferroelectric materials and the corresponding voltages are the coercive voltages of the system (and they are functions of the external pressure intensity).

- The P-V curve (Fig. A.3) shows unequivocally a hysteresis behavior with no saturation, indicating that the electric dipole moment is not saturated, at least under the applied stress intensity (generated by a load of 10 g on the cross between the carbon fibers).

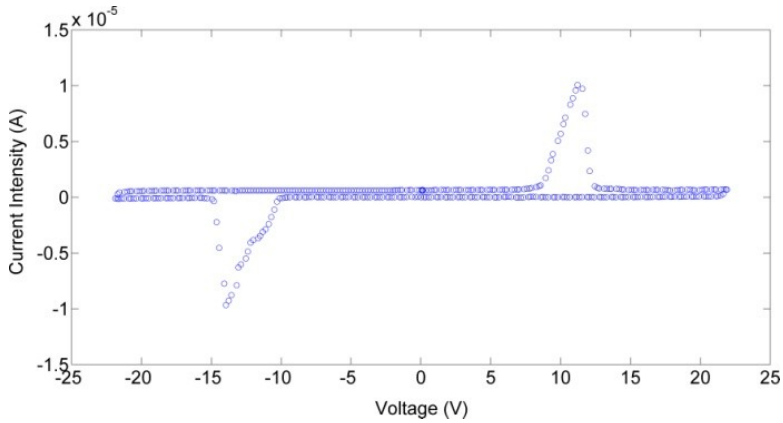

Figure A.2. Polarization lobes detected in the device under static stress application, evidencing the induction of a ferroelectric character.

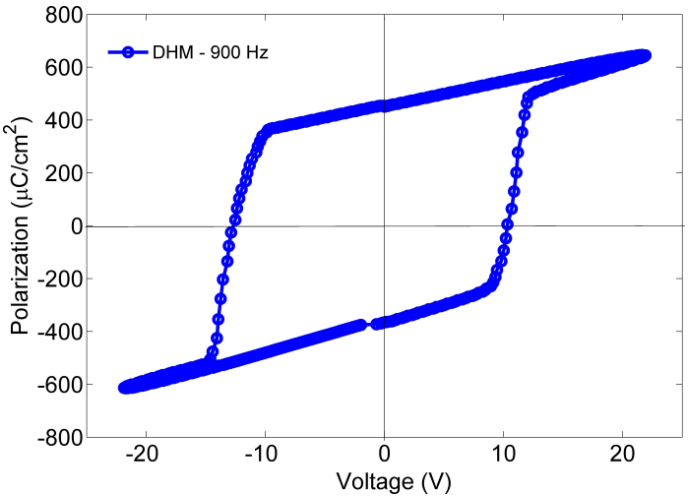

Figure A.3. Polarization measurement under static external stress confirms the piezoelectricity of the device.

In addition to a direct measurement of the stress-induced ferroelectricity, the first ever performed in ZNRs based systems, the measurement of device capacitance in real-time as a function of a reading voltage has to be performed in a process of press and release. This theoretically represents a way to verify a possible applicative scale-up of such devices. The need of a real time response of piezoelectrics to an external pressure is indeed a mandatory stage of characterization. As already said, piezoelectricity is a structural phenomenon related to a symmetry breaking for space inversion operation. Each time piezoelectricity is induced, the electric permittivity changes and so the measured capacitance of the compound. Accordingly, I perform a real-time characterization of the C-V curve under a static and a pulsed stimulus of proper frequency (higher enough to discriminate the dielectric regime). The results of this investigation are reported in Figs. A.4a and A.4b.

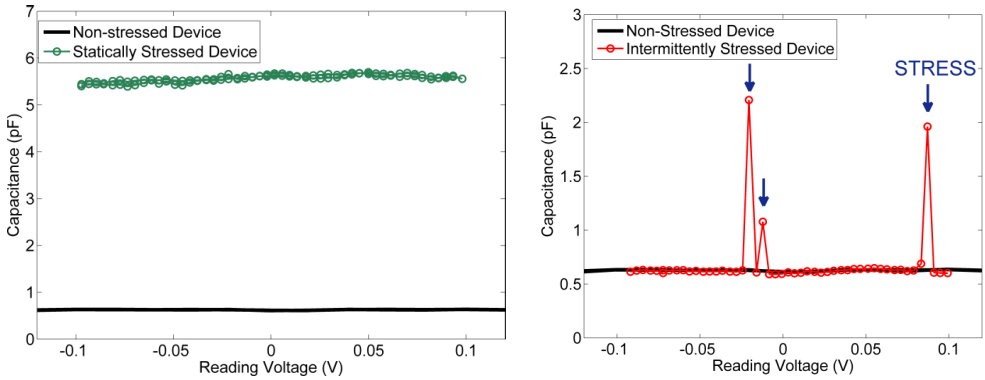

Figure A.4. (a) Real time capacitance response of the device with no external stress (black curve) and under static stress application (green curve). (b) Real time capacitance measurement under intermittent stress application (red curve).

The unstressed system capacitance does not depend on the applied voltage and it displays a mean value of *0.65 pF*. During a static pressure application, the system capacitance abruptly increases to *5.3 pF*, so suggesting the occurrence of an induced polar distortion of the unit cell (Fig. A.4a). Until the stress is retained, the capacitance shows voltage-invariance, confirming that if spurious leakage or a resistive contribution are present, they are almost negligible. This phenomenon could even be recorded dynamically, by means of an intermittent stress application of variable intensity (Fig. A.4b). The goodness and reproducibility of the process is evidenced by the immediate jump of the capacitance whenever the stress is applied together with its instantaneous relaxation back to the standard value once the stress is released. The general significance of such results candidates this innovative and fully integrated system as an intriguing device for technological applications, being clearly demonstrated its sensing behavior. Furthermore the simple device manufacturing, based on just two carbon fibers functionalized by ZnO nanorods, guarantees piezo-sensing performances without requiring other components integration (like metal contacts and wiring elements above all).

Industrial Scale-up simulation for CIGS-based solar cells deposited by PED

The importance of concepts like green energy and sustainability of men's consumptions is nowadays much more than a considerable thematic, I would say fundamental. Despite ethics judgments, I think that they are priorities which cannot be put apart or still overwhelmed by financial-economical interests. In this framework, scientists play a key role, being engaged to find solutions to the two III Millennium-greatest problems: the environmental disease and the slow but inexorable depletion of the traditional oil-based energy sources.

For the sake of honesty, a partial solution already exists lying in the solar cells technology. If in the last decades the market of such energy supply technology significantly expands, the ratio benfits/costs confines it in a subsidiary position with respect to the oil-based energy technology.

In such a way this work targets the goal to launch a low cost industrial alternative for the production of new generation solar cells with efficiency comparable to that of the silicon based commercial solar cells.

The novelty lies both on the use of a new promising photovoltaic material, the quaternary compound CIGS, but, above all, on the exploitation of an unusual production technique, i.e. the PED technique.

PED, the acronym of Pulsed Electron Deposition, utilizes an high energy accelerated electrons beam, produced by an electron gun and directed against a target, causing the material ablation (violent evaporation with the retention of the stoichiometric composition of the solid phase). Consequently the ablated/ionized gas (plume) rapidly expands and crystallizes on a proper substrate in form of a single-phase film layer.

The application of this technique is today limited to scientific purposes, being never considered as a potential industrial solution. The PED scale-up is consequently a virgin field where PED-researcher at IMEM started to move the first steps since the last few years, surely encouraged by the important results obtained in the single-source process

improvement which recently leaded to the reproducible production of CIGS-based solar cells with efficiency higher than the remarkable value of 15% [7].

Their main idea is to design a new and larger apparatus equipped with a multi-source array of PED guns, instead of a single source such as in the case the one devoted to the scientific activity. Single-source PED is indeed not suitable to fabricate commercial (*16*16 cm*^{2} wide) modules due to its narrow-peaked "deposition cone". However, the use of a multi-source PED may theoretically permit to deposit CIGS on a wide area; on the other hand, from a practical point of view, the chamber enlargement may cause a lowering of the photovoltaic characteristics principally, for what concerns the solar energy conversion efficiency. Specifically, the increase of the deposition area directly affects the retention of the high degree of thickness uniformity, from which prevalently depends the observation of high efficiency values. To face this challenging issue, me and my colleague Bronzoni developed a software that mathematically describes the dynamics of multiple PED guns process. The plume spatial distribution, responsible for the morphology of the deposition, can be indeed described by means of the bi-cosine equation (Eq. A.1) that contains two principal contributions: the evaporative one and the ablative one. The thickness distribution function, accordingly with Ref. 8 and Ref. 9, can be defined as:

$$F(\theta,\varphi) = F(\theta) = a\ \cos\theta + (1-a)\ cos^{p}\ \theta, \qquad \text{(A.1)}$$

where ϑ and φ define the solid angle coordinates, a is a constrained coefficient indicating the relative weight of the first addend (evaporation) with respect to the second (ablation), while p is an empirical exponent depending on the PED acceleration voltage (10 ÷ 20 kV), on the chamber background pressure, on the type of material used as target (CIGS) and also on the distance between target and substrate. In the discussed case, both these characteristics are invariant so that p is empirical determined to be *7*.

The simulation program, written in Matlab code, calculates the coating yield, the uniformity and the elapsed time of a complete deposition process as a function of a variable number of PED guns and of different type of substrate motion (static, rotational, translational and roto-

translational). Then by varying the guns coordinates it is possible to estimate the best target arrangement just like the one that maximizes a proper combination of the following reported parameters, marking quality of the deposition process.

-Mean value and standard deviation of the thickness distribution function *F(9)*: they estimate the thickness uniformity upon the entire surface.

-Coating yield: it takes into account the ratio between the amount of the deposited evaporated/ablated material with respect to the overall amount of evaporated/ablated material. Precisely, it is a measurement of material waste.

-Deposition time: it is an estimation of the total deposition process duration for growing a *1.5 μm*-thick CIGS film.

The obtained results clearly displayed strong variations of the deposition quality either varying the number of PED guns or the type of substrate motion. However, it is worth noting that an excessive number of PED guns if on one hand increases the quality of deposition, on the other hand bears heavy down upon the apparatus costs of installation and maintenance, making it no more suitable for industrial application. An economical evaluation suggests that a number of the four guns is the intermediate value that maximizes the ratio deposition-quality/costs-overhead. Therefore, I simulated the most performing four-source PED machines by means of a maximization of the quality parameters as function of the targets spatial arrangement. The obtained thickness spatial distributions are plotted in Figs. A.4, A.5, A.6, and A.7, which refer respectively to the case of a static, linear, rotational and roto-translational motion of the substrate.

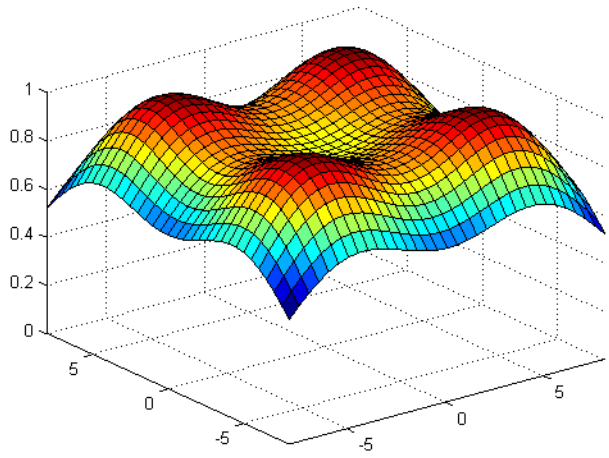

Figure A.4. Thickness profile simulation of a *16*16 cm*^{2} CIGS film deposited by four-source PED on a substrate in static position.

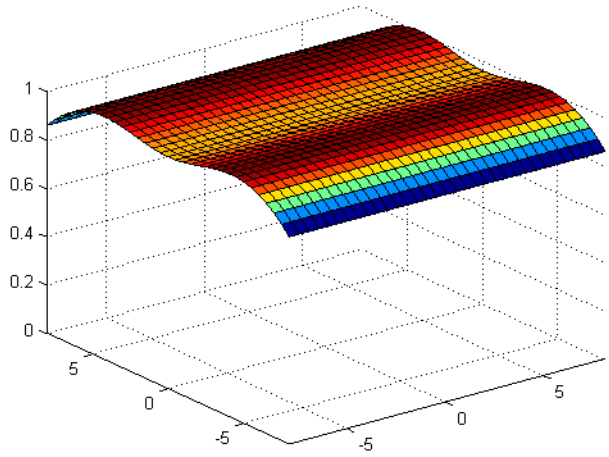

Figure A.5. Thickness profile simulation of a *16*16 cm*^{2} CIGS film deposited by four-source PED on a substrate put in linear (translational) motion.

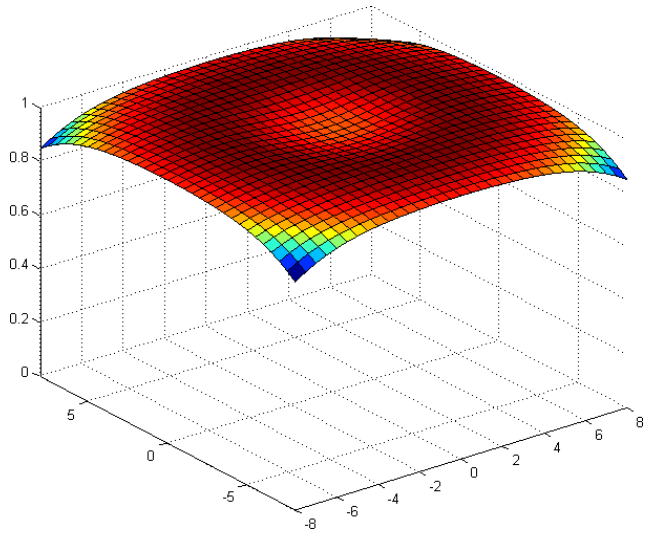

Figure A.6. Thickness profile simulation of a *16*16 cm*^{2} CIGS film deposited by four-source PED on a substrate put in rotational motion.

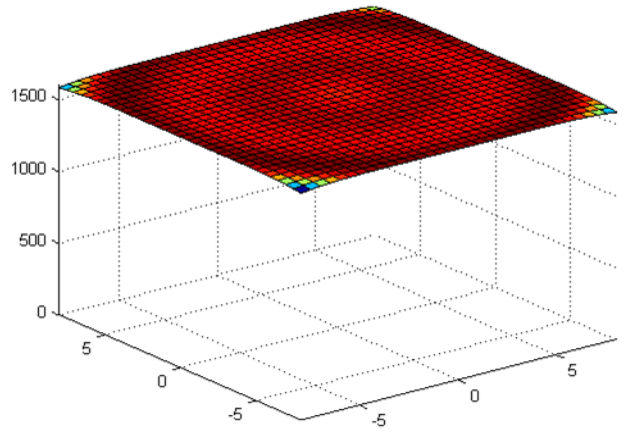

Figure A.7. Thickness profile simulation of a *16*16 cm*^{2} CIGS film deposited by four-source PED on a substrate put in roto-translational motion.

As it can be appreciated, the uniformity of the thickness distribution visibly depends on the choice of the selected substrate motion. Especially, the two linear-motion-based simulations

(Fig. A.5 and Fig. A.7) seem to be more performing with respect to the other two. In addition they are pure dynamical processes and thus they can be treated in two different modalities: as a single substrate deposition process or as a multiple substrate continuous process (like the industrial one). In the latter scenario, a linear-motion-based apparatus operates sequential deposition operations transferring substrates in a row inside the chamber and then outside, developing a real production chain. Consequently, more than a substrate lies in the chamber at the same time: this is a fundamental aspect either for what concerns the reduction of the material wasting or mostly for what concerns a substantial lowering of the deposition mean time per cell. Apart from such qualitative considerations, a detailed estimation of the performances for each type of motion requires a comparison of the deposition quality parameters for the four presented simulations. Such data are collected in Table A.1.

Table A.1. Comparison of the deposition quality parameters between the four different types of motion.

Substrate motion	**Uniformity (%)**	**Coating yield (%)**	**Deposition Time (s)**
Static	*83*	*54*	*81*
(dynamic) Translational	*96*	*46*	*75 / **40****
(static) Rotational	*98*	*31*	*157*
(dynamic) Roto-translational	*99.8*	*30*	*125 / **67****

*****the dynamical- motion based four-sources PED (i.e. translational and roto-translational) support two types of deposition process: a slower single substrate process (italic font) and a faster continuous multisubstrates industrial process (bold font) the considerably brings down the calculated deposition time keeping constant the other quality parameters.

An overall evaluation of these simulations suggests that in particular the roto-translational based four-source PED apparatus allow to obtain extraordinary results. Its performances are even more significant if compared to the standard techniques today exploited in the industrial production of commercial solar cells (e.g. thermal co-evaporation). Specifically PED techniques potentially can achieve higher values of the layer uniformity (~4% more

than co-evaporation) together with extremely lower material waste (~25% less than co-evaporation) and deposition time (~100% less than co-evaporation), as evincible from Table A.2.

Table A.2. Comparison between standard thermal co-evaporation technique, with respect to the simulated four-source PED technique with roto-translational motion of the substrate.

Technique	**Uniformity (%)**	**Std.Dev.(%)**	**Coating yield (%)**	**Deposition time (s)**
Standard thermal co-evaporation	**96**	**3**	**22**	**130**
four-source PED with roto-translational motion	**99.8**	**0.2**	**30**	**67**

In conclusion, the main outcome of the current work (and thus of the correlated patent license) is the concrete perspective of our process industrial scalability even in the short period. Indeed, PED has clearly demonstrated to be a reliable and competitive technique either in terms of cost or performances. Not without personal efforts, my colleagues are installing a first prototype of a four-stage PED apparatus, the so-called "*Alpha Chamber"* (in Italian Camera Alfa) inspiring to the geometrical suggestions pointed out by our simulations (above all for what concerns the guns and targets spatial distribution).

As in every other chapter of my life, probably the best is yet to come while the worst is always around the corner.

Appendix references

[1] D. Calestani, N. Coppedé, M. Culiolo, D. Delmonte, M. Villani, A. Zappettini, L. Marchini, R. Bercella. (2014). *Italian Patent No. MI2014A000499 "Dispositivo piezoelettrico a base di ossido di zinco"*. Milano: Ufficio Italiano Brevetti e Marchi.

[2] M. Bronzoni, D. Delmonte, E. Gilioli, M. Mazzer, F. Pattini, S. Rampino. (2014). *Italian Patent No. MI2014A000960 "Metodo di fabbricazione di celle solari a film sottile"*. Milano: Ufficio Italiano Brevetti e Marchi.

[3] H. Chen, L. Zhu, H. Liu, and W. Li *Nanotech.* **23**, 075402 (2012).

[4] Y. Lin, G. Ehlert, and H. A. Sodano *Adv. Funct. Mater.* **19**,2654–2660 (2009).

[5] Q. Liao, M. Mohr, X. Zhang, Z. Zhang, Y. Zhang, and H. J. Fecht *Nanoscale* **5**, 12350 (2013).

[6] Q. Liao, Z. Zhang, X. Zhang, M. Mohr, Y. Zhang, and H. J. Fecht *Nano Research* **7,** 6 917-928 (2014).

[7] S. Rampino, N. Armani, F. Bissoli, M. Bronzoni, D. Calestani, M. Calicchio, N. Delmonte, E. Gilioli, E. Gombia, R. Mosca, L. Nasi, F. Pattini, A. Zappettini, and M. Mazzer *Appl. Phys. Lett.* **101**, 132107 (2012).

[8] T. Venkatesan, X. D. Wu, A. Inam, and J. B. Watchman *Appl. Phys. Lett.* **52**, 1193 (1988).

[9] H. Dang, Z. Han, and Q. Qin *Science in China* **41**, 12 1310 (1998).

My opinion about Ph.D doctorate

Before concluding this painful Thesis, I feel the urge to put in words a little thought concerning the role of the Ph.D School in the third Millennium.

I started my Ph.D study in Italy, during the strongest western economical crisis since the new Deal in 1929. In the last years I matured the opinion that Doctorate should not be literally considered as a School. I am saying this because today a Ph.D student is directly employed in the management of the scientific activity, he writes papers, organizes the laboratory and takes care of products/materials purchasing; moreover he plans the research development and if necessary is a technician too (installing/repairing instruments and writing software). In addition, he can be involved as teaching assistant, giving also a significant contribution to the educational activity. Honestly, I believe that all these responsibilities depict a new scenario and impose a change in the way to see the organization of the Doctorate School. I would stress that it was for me really stimulating and formative beyond any expectation to be assigned to such an important scientific role. Nevertheless, the possibility to achieve the degree of Philosophiae Doctor, according to the current ministerial regulations, still goes through the necessity to take examinations as well as a normal under-graduate student with no supplemental tasks, although the Ph.D student engagement is completely changed. If the lack of investments represents the current Italian Research extrinsic problem, such an antiquated vision of the Ph.D student role is one, and not the unique, of the current intrinsic problems for which the Government is completely responsible. Really, is it sure that this model can continue to be maintained? Is it the best choice?

I do not think so. Without arrogance, Ph.D students are the engine of the Italian Research. Above that, in any case all the rules are made to be changed.

I sincerely hope that this situation will evolve at some point for the good of the future generations, although nowadays it seems quite impossible.

Acknowledgments

First of all I desire to acknowledge all the external contributions to this Thesis. In particular, Prof. Gabriele Spina of University of Firenze, Dr. Marco Lantieri of ISC–CNR Institute in Firenze for the Mössbauer Spectroscopy analyses and Dr. Andrea Migliori of IMM-CNR Institute in Bologna for the TEM experiments. Moreover I also acknowledge Dr. Clemens Ritter, our Beam Scientist at ILL, for the hand given during the experiments of neutron diffraction.

I am totally grateful to all the members of the heterogeneous "Multiferroic Group" in Parma, whose work is impregnated in these pages. I am principally referring to Dr. Riccardo Cabassi and Dr. Fulvio Bolzoni. Our debates have always been stimulating and enriching, although sometimes rough and glowing. Some scientific results are precisely come by such conflicting discussions. I want to thank also Dr. Chiara Pernechele for the huge number of magnetometric measurements she performed on my multiferroics since 2011; without her help all would have been more complicated.

I am really glad to have deeply met Prof. Gianluca Calestani, probably one of the most important Italian crystallographers and above all a wonderful person. Thank you Prof., for all!!

I sincerely want to celebrate both my Supervisors, Prof. Massimo Solzi and Dr. Edi Gilioli. In different ways and with different personalities and inclinations they gave me complete trust treating me not as student, but as a normal colleague (see the previous tail piece to understand how much this is important for me). I do not know if it could exist a greater gift. I don't think so. Every day I ask to myself if I really deserved such a high commendation, anyhow I am honored to have worked with you!!

I want to devote a special paragraph to my closer collaborator, the man who was on my side since the beginning of my scientific journey, my friend Dr. Francesco Mezzadri. It would be difficult to find the right words even with my native language…try to imagine in English… I know that you don't like the mushy mannerisms, but now it is my conscience that is

writing. I owe it to you, no matter what you think! You are a big Man and a big Scientist Capo (etor che bali)!!!

And now… perhaps… after more than 180 pages… I think… yes… sì… the time has come to write... in italiano insomma, porca misera, e svestire questi panni formali, che mi vanno stretti per definizione. Quest'ultima parte dei ringraziamenti è per le persone che mi hanno accompagnato lungo questo dottorato ed oltre nel tempo. Comincio dai miei colleghi ad IMEM, tra loro i più stretti: Villo, Coppe, Zapp, il Calle, la Bonni, il Ben, la Giulia, il Patto, Ste, il Fabbro, Filo e mio "fratello" Zamb. Ragas siete dei deficienti, ma guai se non ci foste! Un capitolo a parte, loro credo capiranno, spetta però al mio alterego, all'uomo che dal 2011 divide l'ufficio con me e che è parte integrante della mia quotidiana sofferenza. Perché nella sofferenza e nel disagio si lega a doppio filo il nostro rapporto. Perché la massima gioia è diventata ormai la condizione irraggiungibile dell'essere lasciati in pace, di non esser disturbati. Perché se sta andando particolarmente male è il caso di andare a bere una Pepsi; perché se sta andando bene vuol dire che stiamo andando a casa; perché se sta andando come sempre vuol dire che è appena suonata la sveglia ed è iniziata un'altra giornata. Dopodiché … stacco temporale … Siamo lì, nel tombale Studio 100, in silenzio, a fissare con occhiaie nere come la notte i rispettivi detestati schermi, in attesa della menata successiva. Ed è in quel momento di quiete apparente che, senza che nessuno di noi le abbia mai davvero pronunciate, poche parole tracciano la connessione, effimere come l'etere ma pesanti come il piombo: "Meno male che siamo in Due!". Ti voglio bene Bronz!!

Ringraziare poi tutti gli amici di una vita sarebbe un puro esercizio stilistico, anche perché questa Tesi è legata al mio mondo lavorativo molto più delle altre che invece rappresentavano un passaggio di vita. Non serve tributarli perché mai lo pretenderebbero.

Voglio dare un bacio vero a mia nonna Milena, che vale anche per gli altri miei tre nonni che non ci sono più. Loro mi hanno cresciuto ed amato gratis, senza misurarlo o quantificarlo ma solo perché io ero il loro Davide. Questo atto d'amore semplice è la cosa più smisurata che io conosca.

Poi c'è Elga … lei è dentro ogni mio giorno a prescindere che sia effettivamente con me. In questa sede le voglio solo dirle due parole: Grazie e Scusa (le altre le conservo per noi).

Infine viene la mia famiglia: mio padre, mia madre e mio fratello. Per quanto non lo abbia mai neanche minimamente dimostrato, io sono fiero di voi!

L'ultimo pensiero lo dedico a me stesso. Lo potevi fare questo passo idiota, hai visto?

Sono le ore 19 (7 pm) del 23 gennaio; sancisco la chiusura di questo ultimo massacrante passaggio accademico:

-5 -4 -3 -2 -1 ... chi ha qualcosa in contrario a riguardo fa senza parlare, semplicemente taccia … 0.

Parma, January 23th 2014

The author

…. finally free